McGill University

Ph.D Thesis

All-optical THz pulse shaping in a dynamic waveguide

Author:
Lauren Gingras

Supervisor:
Pr. David G. Cooke

A thesis submitted to McGill University in partial fulfilment of the requirements of the degree of Doctor of Philosophy, Physics

Department of Physics
McGill University, Montreal
April 2019

McGill

"The mountains are calling and I must go."

- John Muir

MCGILL UNIVERSITY

Abstract

Faculty of Science

Department of Physics

Doctor of Philosophy, Physics

All-optical THz pulse shaping in a dynamic waveguide

by Lauren Gingras

Controlling light and manipulating its flow is an important capability for the development of new technologies, often relevant to communications, and to fundamental research alike. All-optical control using pulsed laser systems allows dynamic photon manipulation on femtosecond timescales and enables ultrafast, reversible switching often unlocking new capabilities beyond passive optical components.

In this work, we demonstrate an all-optical platform for THz pulse shaping based on charge carrier photoinjection inside a semiconductor-filled parallel-plate waveguide operating over a broadband frequency range between 0.1 and 1.5 THz. The synthesis of arbitrarily-shaped THz waveforms, tunable in amplitude, linewidth and center frequency, is demonstrated by creating multiple replicas of a single-cycle high-field THz pulse. The physics underlying the platform's inner workings are discussed and we present experimental data collected using pump-probe time-domain THz spectroscopy. The platform further demonstrates the ability to tune the phase of the reflected single-cycle pulse and the capability to engineer the instantaneous frequency of a waveform demonstrating positive, negative and compound chirps.

We further present preliminary experimental results using such sculpted pulses to perform space-to-time imaging as well as time-to-space imaging. We discuss the possibility of dynamic photonic band structure switching and show preliminary demonstrations of coherent control of rotational wave packets in water vapour.

Abbrégé

La capacité de contrôler la lumière et de manipuler sa propagation est une compétence importante dans le développement de nouvelles technologies souvent essentielle aux communications et à la recherche fondamentale également. Le contrôle entièrement optique employant un laser pulsé permet d'effectuer des manipulations photoniques dynamiques sur l'échelle de la femtoseconde et rend possible des commutations ultrarapides et réversibles souvent débloquant de nouvelles capacités qui vont au-delà des composantes optiques passives.

Dans ce manuscrit, nous démontrons une plateforme entièrement optique pour former des impulsions THz basée sur la photo-injection de porteurs de charge à l'intérieur d'un guide d'onde à plaques parallèles empli d'un semiconducteur sur une bande de fréquence allant de 0.1 à 1.5 THz. La synthèse d'impulsions THz de forme arbitraire modulaire en amplitude, largeur de raie, et fréquence centrale est démontrée par la création de multiples répliques d'un pulse THz monocycle à haute intensité. La physique sous-jacente est discutée et nous présentons des données expérimentales collectées utilisant la spectroscopie THz pompe-sonde résolue en temps. La platforme démontre d'ailleurs l'habileté à moduler la phase d'une impulsion monocycle réfléchie ainsi que la capacité de sculpter la fréquence instantanée d'une onde en démontrant un chirp positif, négatif et composés.

Nous présentons de plus des résultats expérimentaux supplémentaires employant la méthode de modulation des pulses pour démontrer l'imagerie espace-temps ainsi que temps-espace. Nous discutons de plus de la possibilité de créer des structures de bandes photoniques de façon dynamique et démontrons des résultats préliminaires de manipulation cohérente du paquet d'onde de molécules d'eau à l'état gazeux.

Acknowledgements

There are a number of people to whom I would like to address my most sincere thanks. First of all Dave. Thank you for being an outstanding supervisor throughout the last 7 years. Thank you for welcoming me into the THz community and allowing me to meet and mingle with some of the finest researchers that make this field so special. I am grateful for all the experiences I've had over the last several years and for your understanding that there is more to life than what goes on in the lab. I hope this project will be the foundation for many more undertakings and one of the foundations of your quest to ultrafast enlightenment. All the best to you, Nicole and Dana. Godspeed Rocket Man.

I've also had the chance to cross paths with a good number of outstanding students during the course of my PhD. First and foremost: David V., I've had the chance to learn and think about the technical problems and laser issues at your side. Wishing you the best in life and through all your undertakings. Thanks to Ben and Yang, it's been a pleasure working with you and to see you both become some of the finest THz spectroscopists out there. Best of luck on your measurements and may your samples always be clean. Most of all, thank you Dom for all the hours spent in the lab banging our heads on the wall. Thanks for helping make insurmountable tasks a 2-week deal. Thanks for the board game nights, the drinks and the self-inflicted camping nights in a rental compact. I would wish you luck but you've already shown that you don't need it. I simply wish you courage and determination for your last push to graduation.

Special thanks to Jean-Michel for being an admirable host supervisor over the last year. Though pre-tenure years are often a stressful time, you were always welcoming to this new collaboration. There never was a real promise of results to begin with, yet you always welcomed new ideas and offered us time with your instruments. Thanks for the learning opportunity, the tips and tricks and for helping make this project so successful.

I would also like to thank the students at UOttawa for their help in the lab. Thanks to Wei for always being there, rain or shine, to help me get started with the equipment. Wishing you the best and of course success in your ongoing research. Thank you Aidan for helping carry the torch. Thank you for helping pick up the experiments when I was needed elsewhere and I hope your further research with this platform will be very fruitful.

Behind every great project usually lies a great technician. In this case I would like to give special thanks to the three outstanding techs at the center for condensed matter physics. John,

it's thanks to you if our tables were always floating. Thanks for helping us make it through countless mechanical failures and for safeguarding the lab. Thanks to Robert for all the help with sample preparation, for all the guidance and help fixing things. Thanks to Richard for all the hours helping with mechanical fabrication, for all the resources and help ordering the right parts and tools. Thank you all for always helping promptly and for running to our rescue when things were bad. I would also like to thank the technicians in the McGill microfab, specially Sasa and Jun. It's thanks to you if I always got samples just the way I wanted them.

Thanks to John, my running coach, for helping me get through tough times. It takes a healthy body to host a healthy mind. You gave me the strength to deal with the stress and anxiety. You helped me accomplish things I would have never thought possible. You showed me dedication, determination and gave me the tools to pursue dreams and goals outside of academia.

Most of all, thanks to Stephanie for always being there to support me. You have been an amazing partner and this accomplishment is as much yours as it is mine. Thank you for all the attentions, for pulling more weight when I was pushing through long experiments. Thank you for caring, understanding and listening, though you like to claim that you're lost beyond terms like "laser" and "shadow mask". Thank you for always knowing what I need, be it some rest, a moment alone or a kick in the rear to get me moving forward again. Thank you for being there for the happy moments, through the tough ones, but also for making happy memories out of ordinary moments. Thanks for understanding and for supporting me, even when I'm undertaking something that seems beyond reasonable. I can't wait for our next adventure together.

Thanks to my mother for helping me through this endeavour. Though it pains me greatly that you will not be here to witness the end, I am forever grateful for everything you've given me. Thanks for always helping me, in any way you could, with all my projects, whether in or outside school. Thank you for always loving and caring for me and for always listening. Thank you for always giving, even when you had other things on your mind. Thank you for showing me strength and teaching me to find beauty in all things around me. Thank you for giving me your love of the outdoors and of adventure and for taking me with you on some of the most memorable ones. I am forever grateful for all the moments we have spent together.

Finally, thanks to my dad for supporting me from the very beginning and beyond. Thanks for all the time spent helping me with my homework. Thanks for teaching me the values of hard work and also a good work-life balance. Thank you for teaching me manual work and how

to make my visions into usable elements. Thank you for always giving and never asking for anything in return. Thank you for listening and caring, though I suspect not all my interests connect with you. Thank you for all the memories, I look forward to making more in the years to come.

Thank you all for supporting me through this endeavour and for helping me make this idea into a state-of-the-art system.

Contribution to original knowledge

The entirety of the work presented in this manuscript is based on previous proof of concept demonstrations made by Pr. David Cooke, principal advisor to this thesis, during the course of his post-doctoral fellow at the Technical University of Denmark (DTU) in 2008 and 2009. The initial platform used an oscillator-based source and a silicon-filled parallel-plate waveguide to demonstrate attenuation and time-delay of a broadband terahertz pulse. The platform was further developed to be integrated to an amplified laser system and used to demonstrate inter-modal coupling inside a waveguide for a Masters thesis project [1].

The first step taken further was the addition of a patterned photoexcitation resulting in controllable tuning of the waveguide dispersion, on resonance [2]. While the data demonstrates the switching of a resonance faster than the transit time of the pulse, no spectral signatures were observed which would require switching the band structure faster than the carrier wave. This is the first demonstration of switching a photonic band structure from the light line. Perhaps the greatest insight and most enabling step taken in this work was to begin working in a configuration where the reflected beam was collected. The waveforms reflected by the device demonstrate the ability to create shaped THz waveforms for the first time. This is significant because most modern methods of generating strong field THz pulses produce single cycle THz pulses. This technique offers the ability to transform these pulses into any shape one desires, and has applications in data encoding as well as quantum control. The papers presented in chapters 5 and 6 [3, 4] demonstrate some of the capabilities of this platform. In essence, it allows synthesizing of THz waveforms in an all-optical fashion which makes the platform reversible and fully reconfigurable. The monochromaticity of generated multi-cycle waveforms demonstrated is on par with commercially available THz bandpass filters but, as mentioned, also offers full reconfigurability. The platform demonstrated and developed has, to the best of our knowledge, unprecedented and unparalleled pulse shaping capabilities at low-THz frequencies. We believe it is an enabling technology for THz control experiments that require more convoluted THz multi-cycle waveforms. Early unpublished results are presented in chapter 7 as a demonstration of some of the suggested applications. Each author's contributions to the work presented in this manuscript is included at the beginning of the respective chapters.

Contents

List of Figures

Abbreviations

THz	**T**era **H**ertz
TDS	**T**ime **D**omain **S**pectroscopy
ZnTe	**Z**inc **T**elluride
GaP	**G**allium **P**hosphide
$LiNbO_3$	**L**ithium **N**iobate
DFG	**D**ifference **F**requency **G**eneration
SHG	**S**econd **H**armonic **G**eneration
EO	**E**lectro-**O**ptic
TO	**T**ransverse **O**ptical
TEM	**T**ransverse **E**lectro-**M**agnetic
TE	**T**ransverse **E**lectric
TM	**T**ransverse **M**agnetic
CEP	**C**arrier **E**nvelope **P**hase
ITO	**I**ndium **T**in **O**xide
OPA	**O**ptical **P**arametric **A**mplifier
Nd:YLF	**N**eodymium-doped **Y**ttrium **L**ithium **F**luoride
Tb:KGW	**Y**tterbium-doped **P**otassium **G**adolinium **T**ungstate
Ti:sapph	**T**itanium-doped **S**apphire
CMOS	**C**omplimentary **M**etal-**O**xide **S**emiconductor
HDPE	**H**igh-**D**ensity **P**oly**E**thylene
FFT	**F**ast **F**ourier **T**ransform
NIR	**N**ear **I**nfra **R**ed
PPWG	**P**arallel **P**late **W**ave **G**uide
ASCII	**A**merican **S**tandard **C**ode for **I**nformation **I**nterchange
SI	**S**tandard **I**nternational (unit system)

Physical Constants

Speed of light	c	=	$2.997\ 924\ 58 \times 10^{8}$ [m/s] (exact)
Permittivity of free space	ϵ_0	=	$8.854\ 187\ 82 \times 10^{-12}$ [C^2/Nm^2] (exact)
Permeability of free space	μ_0	=	$4\pi \times 10^{-7}$ [N/A^2] (exact)
Charge of electrons	e	=	$1.602\ 176\ 57 \times 10^{-19}$ [C]
Mass of electrons	m_e	=	$9.109\ 382\ 91 \times 10^{-31}$ [kg]
Boltzmann constant	k_B	=	$1.380\ 648\ 8 \times 10^{-23}$ [m^2s^2kg/s^2K]

Symbols

d	Thickness of the slab waveguide	[m]
L	Length of the slab waveguide	[m]
m^*	Effective mass	[electron masses]
$\mathbf{E}$	Electric field	[V/m]
$\mathbf{H}$	Magnetic field	[A/m]
E_{Ref}	Reference terahertz electric field waveform	[V/m]
E_{Refl}	Reflected terahertz electric field waveform	[V/m]
E_{Trans}	Transmitted terahertz electric field waveform	[V/m]
χ	Electric susceptibility	
$\tilde{\epsilon}$	Complex relative permittivity	
ϵ_1	Real part of the relative permittivity	
ϵ_2	Imaginary part of the relative permittivity	
$\tilde{n}$	Complex refractive index	
n	Real part of the refractive index	
κ	Imaginary part of the refractive index	
σ	Complex conductivity	$[\Omega\ \mathrm{cm}]^{-1}$
σ_1	Real part of the conductivity	$[\Omega\ \mathrm{cm}]^{-1}$
σ_2	Imaginary part of the conductivity	$[\Omega\ \mathrm{cm}]^{-1}$
σ_{dc}	DC conductance	[S]
μ_e	Charge carrier mobility	$[\mathrm{m}^2\mathrm{s}^{-1}\mathrm{V}^{-1}]$
α	Absorption coefficient	$[\mathrm{cm}]^{-1}$
ω	Angular frequency	[rads/s]
ω_p	Plasma frequency	[rads/s]
τ	Charge carrier scattering time	[s]

Chapter 1

Introduction

1.1 The terahertz spectrum

Though the concept that light should be simultaneously treated as a wave and as a particle is universally accepted, it remains enormously advantageous, both mathematically and conceptually, to treat only one of the two cases at a time. In consequence, a great divide was formed in the electromagnetic spectrum. On the one side, where wavelengths are longer than the typical object observable by the naked eye, frequencies of interest are typically slow. Notably radio waves, at the far end of the spectrum, where frequencies are akin to that of audible sound waves. Slightly closer, still on the low-frequency side, the regime of microwaves is found, where not only one can heat up dinner but also where modern day communications have thrived and enabled us to wirelessly connect the world's population through the internet. All the aforementioned regimes are more widely treated in the wave-like pictures where oscillations of the electro-magnetic field of light is slow enough to be picked up by free charges. Consequently, these waves are typically generated and detected via antennas. For this reason the worlds of electronics and microwaves have symbiotically evolved since the later half of the 20^{th} century. On the other side of the divide, we find the world of photonics where, as the name makes it obvious, light is generally treated in the photon picture. Where as on the long-wavelength side of the spectrum frequency is the typical unit of measure, beyond the visible range energy is a much more typical unit of measure. Here in the realm of ultraviolet radiation and gamma rays, interactions between light and matter more generally result in light imparting all of its energy onto particles or atoms in a fashion more akin to a collision, hence the particle picture prevails.

By the same rationale, sources of UV or gamma radiation are generally thermal sources of extreme temperature, particle collision-based sources or radioactively decaying elements.

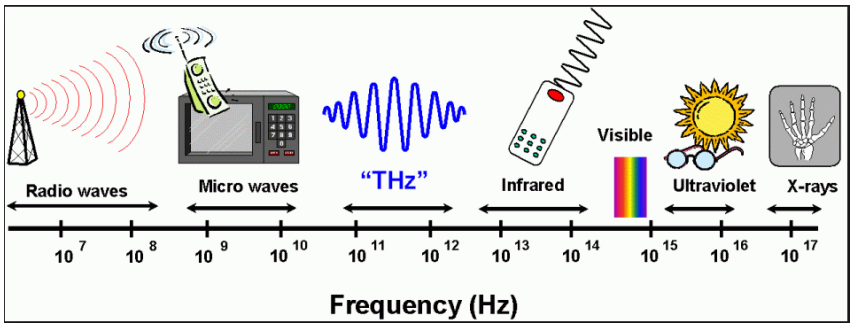

FIGURE 1.1: Artistic representation of the electromagnetic spectrum showing where the THz gap lies. Credits: Daniel Mittleman, circa 1995.

Naturally, this divide left what was long called the "Terahertz gap" at its center. Where most of the visible spectrum and the lower-energy near-infrared and mid-infrared bands had been conquered via what could be called a more "photonic" approach, the far-infrared long remained the ultimate frontier in terms of electromagnetic radiation. Before we discuss the technologies that helped bridge this gap, we want to ensure that the readers are in familiar territory here. We present a comparative figure showing the equivalence of the THz gap in units of frequency, wavelength, wavenumber and photon energy in Fig. 1.2 encompassing the terahertz spectrum, loosely defined as encompassing frequencies from 300 GHz up to 10 THz.

One of the earliest and perhaps one of the most enabling demonstrations came in the form of a broadband source of THz radiation that was also, conveniently, a great detector for said waves. The Auston switch, first demonstrated in 1975 [5], harnessed photo-injected charge carriers to drive a picosecond current between two biased metallic gates inside a high-mobility semiconductor. This extremely short-lived transit of charges resulted in a radiated ps electromagnetic pulse frequency-centered around 1 THz. This new family of emitters was made possible thanks to advancements accomplished in the development of pulsed coherent laser sources which rendered picosecond photoexcitation of free charges possible. By the same process, charges could be excited across the detector antenna and that same THz field was used to drive them across the gates allowing the measurement of a current proportional to the THz electric field with a direction dictated by its phase. Further progress was made in the following decades, pioneers such as David Auston, Daniel R. Grischkowsky, Xi-Cheng Zhang spearheading the efforts to bring the worlds of photonics and electronics to a meeting point in the THz gap.

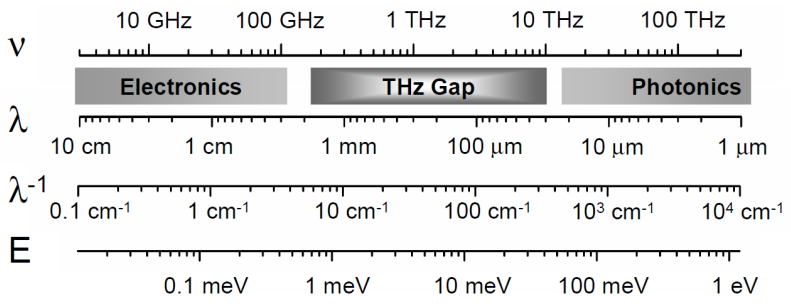

FIGURE 1.2: THz gap with respect to frequency, wavelength, wavenumber and photon energy [184].

The commercial availability of turn-key high-power femtosecond (fs) pulsed laser systems has since then contributed enormously to the development of more efficient sources of terahertz light. With innovations made using non-linear crystals to generate broadband THz radiation through optical rectification, a process further discussed in chapter 2, the THz community soon saw its own gold rush. With the promise of investigating condensed matter transients with femtosecond resolution [6–10], performing industrial non-destructive imaging and evaluation [11], investigating chemical species and transitions [12–14], remotely detecting illicit substances [15–17] and explosives [18, 19], security detection [20–24], and medical sensing and imaging [25–29], terahertz science quickly established itself as a powerful tool for probing low-energy phenomena on ultrafast timescales.

From a fundamental science standpoint, being able to probe the transport properties of semiconductors such as conductivity, photoconductivity, and carrier lifetimes is an extremely desirable capability. The advent of broadband time-resolved terahertz spectroscopy [30] enabled the scientific community to harness spectroscopic information in a fully phase-resolved and coherent fashion even below the black-body radiation level of materials [31]. To put it plainly, this measurement technique, further discussed in chapter 2, directly measures the time-resolved electric field thus enabling one to extract fundamental dielectric properties of semiconductors and other materials without having to resort to Kramers-Kronig relations. Moreover, synchronization with a femtosecond laser and the short duration of the THz broadband pulse enable one to follow the dynamics of these frequency-dependant optical functions following photoexcitation with a temporal resolution of 10 fs. This technique is especially powerful when studying events with picosecond characteristic lifetimes such as scattering of free charges [32], phonon oscillations of a crystal lattice [33], and plasma oscillations [34–36], to name a few.

The more recent development of high-peak electric field terahertz sources [37–42] has not only allowed for non-linear spectroscopy at THz frequencies [43–46] but has become central to enabling a great number of new technologies. The ability to generate time-controlled bursts of radiation with electric fields on the order of MegaVolts/cm using tabletop rather than accelerator-based sources has been the epicentre for the fields of ultrafast nanoscopy [47–51] and THz field electron emission and acceleration [52–57].

Moreover, the telecommunications industry has had its eyes set on the THz band for several years now. As consumer demand increases for bandwidth and sheer volume of data, wireless communication methods have had to evolve and adapt. The most obvious leap conceivable to increase data transfer rates is to broaden the bandwidth employed. This is usually more easily accomplished by expanding communication devices to higher carrier frequencies, as exemplified by the transition of consumer WiFi bands from 2.3 GHz to 5 GHz and by the escalation of cellular bands form 1.8 GHz in 2G technologies to 2 GHz in 3G technologies, pushed up to 8 GHz in 4G technologies. Now with 5G around the corner having been allocated up to 86 GHz into the millimeter wave range the prospect of directional high-frequency telecommunications is becoming even more realistic. Companies, such as Nippon Hoso Kyokai in Japan, have also started cornering the market for ultra broadband point-to-point connections allowing transmission of ultra-high-definition videos in an effort to render costly camera equipment more portable for live events broadcasts [58].

1.2 An all-optical modulator

One of the key motivations behind this project is the fact that, like mentioned previously, the demand for high bandwidth in the telecommunications industry has pushed the Federal Communication Commission (FCC) to allocate bandwidths up to 300 GHz. Everything beyond that falls into the THz regime and is completely uncharted territory. Recent efforts to use existing diode and antenna-based sources along-side multiplexing schemes have been used to demonstrate point-to-point wireless communication in air with rates up to 100 GB/s over several meters in a laboratory environment [59]. More recent results show promise in terms of bandwidth expansion using antenna units [60, 61], photodiodes [62] and GaAs transistors [63] and pushing the transmission distances using uni-travelling photodiodes [64] and monolithic integrated circuits [65]. State of the art systems are already demonstrating 400 Gb/s transmission over 100 meters in free space [66]. Most of these advances are rooted in the modulation and mixing of near infrared

telecommunication frequency signals which are converted and detected via passive elements. A more extensive review of telecommunication-oriented technologies can be found in ref. [67]. III-V semiconductor-based methods, such as InP transistors have more recently been used to demonstrate power amplifiers of 200 mW at 210 GHz and showing amplification up to 670 GHz [68]. Architectures based on silicon have also stepped into THz territory generating picosecond pulses with frequencies even exceeding 1 THz [69, 70]. Due to their modest footprint, these structures can also be arranged into arrays to perform beam steering [71]. The ability to control the propagation of THz waves is also crucial to communication applications and key components such as passive [72] and active [73] splitters, multiplexers [74, 75], and spatial light modulators that are electrically tunable [76, 77] have been studied. Though the recent progress has been remarkable, there is still a need for novel technologies to modulate, de-modulate, beamform, steer, store and generally control THz radiation in an active fashion.

Industry requirements and demands of course spark a lot of interest from an applications and engineering standpoint, but achieving control over THz waveforms is equally if not more appealing from a fundamental science standpoint. A lot of effort have been spent on studying the nature of light and predicting optical analogues to other natural phenomena. For example, a properly engineered dynamic modulation inside a resonator structure is predicted to give rise to a photonic equivalent to the Lorentz force [78], a particle without mass or charge. Careful modulation of the dielectric environment of light in a dielectric slab waveguide is also predicted to give rise to a photonic Aharonov-Bohm effect [79]. Ultrafast modulation of resonator cavities has also been used to overcome the delay-bandwidth limit [80] as well as light stopping and time-reversal processes [81]. Over the past 10 years, the ultrafast community has been enthused with the idea of developing and employing pulsed sources of light with sub-cycle tunability [82–86]. The main attraction is the ability to probe phenomena occurring in matter at energies significantly lower than most semiconductor bandgaps but with extreme time resolution. Furthermore, these methods allowed for the investigation of more elusive phenomena such as high harmonic emission in crystals [87] and graphene [88, 89] as well as the observation of Dirac currents in topological surfaces [90].

For all of these applications and for much of these fundamental research motivations, a good number of platforms and devices have been developed for terahertz modulation. In the early 2000s, THz research saw a device boom in the form metamaterials. An originally well established technology used to filter microwave frequencies, these sub-wavelength conductive resonator arrays were scaled down using standard lithographic methods to better work in the THz domain.

Using metal-on-dielectric architectures, these compact passive filters were made into low-pass [91], high-pass [92], band-pass [93–96] and notch filters [97]. Optical modulation also became a natural extension of these devices where by injecting carriers in the underlying semiconductor via ultrafast pump excitation the transmission characteristics could be switched on an picosecond timescale [98–100]. These devices, dubbed "frequency-agile" and shown in Fig. 1.3a), however only offered tunability in the vicinity of their native engineered resonance thus limiting their individual versatility. Other sources, such as quantum cascade lasers (QCL), displayed in Fig. 1.3c), also offer a certain amount of tunability [101–105]. The major drawback of this methods is that the electronic confinement of the quantum cascade requires low-temperature operation [106]. Other sources have also been developed in recent years in order to provide tunable THz emitters. Notably, periodically-poled lithium niobate (PPLN) has been getting some attention as it provides extremely high conversion efficiencies [107, 108]. The inconvenience of using PPLN is that tunability is also linked to the quasi-phase matching condition which is determined by the size of every domain in the crystal and thus locked in the design phase [109]. Lithium niobate ($LiNbO_3$) has also been used to develop tunable THz sources based on the modulation of an excitation near-infrared pulse. For example, Pr. Tonouchi's group at Osaka University showed that by geometrically patterning the input facet of a $LiNbO_3$ crystal, as shown in Fig. 1.3b), in the tilted pulse-front method, further discussed in chapter 3, one can generate narrowband high electric field THz waveforms with tunable center frequency and bandwidth [110, 111]. Additionally, mixing of detuned laser lines was more recently used to generate frequency and linewidth-tunable THz generation in a method described as injection-seeded terahertz-wave parametric generator (is-TPG) [112]. All of the previously listed methods have shown promise, whether through high efficiency or simplicity, though none of them can claim to do it all. Moreover, only few of the previously mentioned techniques have claimed adjustability over the underlying phase of the THz waveforms.

For control over the THz pulse carrier-envelope phase (CEP), fewer methods present themselves. It is important to note that in the photon or intensity picture, where light absorption does not typically depend on the field shape, the polarity or CEP of the excitation pulse is largely irrelevant. For highly non-linear phenomena, where the effects studied are dependant on the amplitude of the instantaneous electric field of the pulse, tuning of the CEP becomes imperative. To tune the phase of a typical THz broadband pulse via phase delay methods, one needs to engineer a material or device capable of flat phase shifting over roughly 5 octaves in frequency, about 5 times the span of the entire spectrum visible to the human eye. This major obstacle is

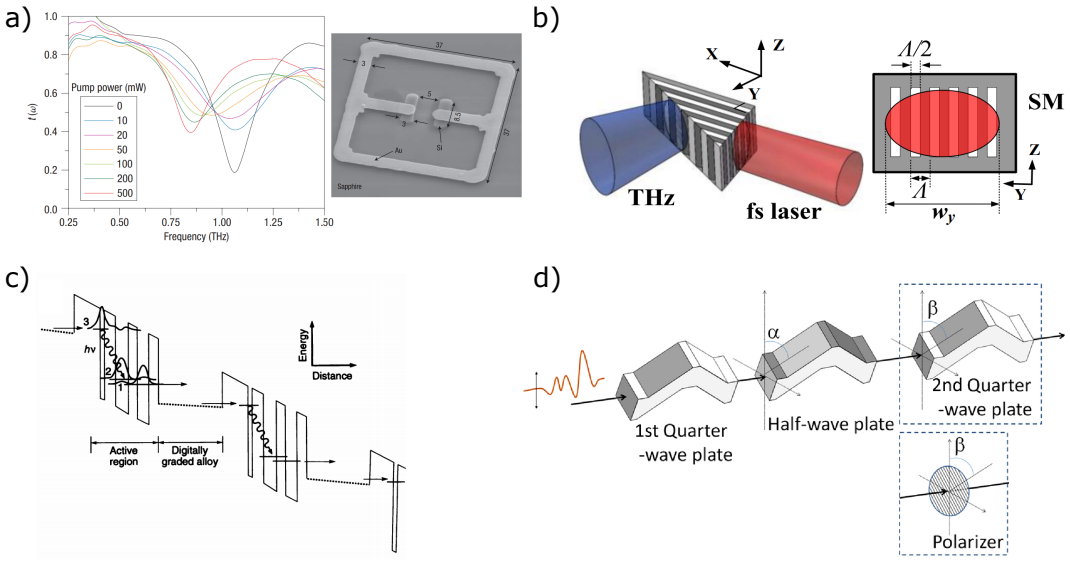

FIGURE 1.3: a) Transmission characteristics and capture of the frequency agile metamaterials [99]. b) Schematic representation of a large aperture PPLN crystal used for tunable narrowband THz generation [110]. c) Schematic representation of the principle of operation of a quantum cascade laser [113]. d) Representation of the phase shifter components from ref. [114].

why most research groups tend to lean towards simpler methods such as using the Guoy phase shift which naturally occurs at any focus of a Gaussian pulse. Other ingenious researchers have developed broadband waveplates using high-resistivity monolithic silicon prisms, showed in Fig. 1.3d), in order to continuously phase shift a single-cycle THz pulse with $\approx$ 10 % transmission [114, 115]. Though both described methods are relatively simple, they are also actuated mechanically and thus greatly limited if rapid tuning is necessary. For this, an optical [99, 100] or electronic [116] actuation method would be preferable.

On a side note, another important characteristic of propagating light waves is their polarization state. Though most THz sources are linearly-polarized by nature, a good number of effects are better accessed via circularly-polarized states of light [117, 118]. More exotic polarization states, such as vortex beams [119–121], have also been shown to be better suited to study more elusive natural phenomena. The platform discussed in this work does not, however, offer any way to tune the polarization state of THz light.

Modulation of electromagnetic waves has been the focus of much research in the infrared band, mostly using passive components integrated to transmission lines. Using metallic boundaries and spatially varying refractive indices light is confined and guided such as in an optical fibre. These devices can also be used to attenuate given frequencies, though this approach generally

makes the device non-reconfigurable. Using the right design, the propagation direction, phase and even speed at which light travels can be modified. Most of these methods naturally extend easily to the THz spectrum as geometrically defined devices can be scaled with wavelength. Many of these structures have already been studied at THz frequencies, for example: photonic crystals [122, 123], microcavity resonators [124], single-groove notch filters [125, 126], Bragg resonant structures [127] and curved-surface waveguides [128]. One of the great advantages of these devices is that the confinement they provide makes for a small footprint which is highly desirable for platforms potentially aimed at industry applications. Furthermore, THz platforms benefit from the transparency of a wide number of industry-standard semiconductors making their implementation easier. Semiconductor waveguide platforms have already shown great promise in the THz range, with early demonstrations being made in the millimeter-wave range in the second half of the 90s [129–131]. One-dimensional defect structures were also investigated through THz pump-probe spectroscopy methods [132] as well as dynamic tuning of a THz signal inside a sub-wavelength resonator [98]. All of the demonstrations mentioned here benefit greatly from micro and nano-fabrication techniques which allow for the definition of details, components and defects on $\lambda_{THz}/100$ lengthscales which greatly supresses scattering losses in transmission lines alongside resonator quality factors reaching over 1000 [122, 127, 133–137].

In the work presented in this thesis, we demonstrate an all-optical platform for arbitrary pulse shaping in the THz domain, building on previous work by Prof. Cooke on active THz waveguides [138, 139]. It has already been used to demonstrate transmission amplitude attenuation [140] control over the propagation direction and pulse delay [141]. More recently and by the author of this thesis, it was used to show tunable coupling between the geometric waveguide modes [1]. The platform uses photoinjection inside a silicon-filled parallel-plate waveguide (PPWG) to modulate the transmission and reflection properties of the THz signal. The research presented in the following chapters focuses on the patterning of the photoinjected regions in order to create one-dimensional arrays. The operating principle is schematically presented in Fig. 1.4 where a spatially patterned pulse of near-infrared light is used to modulate the transmitted and reflected properties of a guided THz waveform. The modulation is generated by spatial patterning of the silicon's dielectric function via the introduction of charge carriers by an optical pump with above bandgap photon energy. The platform is fully reversible, meaning that after charge carrier recombination it reverts back to a simple homogeneous dielectric-filled PPWG on a μs timescale. The same idea also makes it completely reconfigurable, implying that one can in principle change the transmission or reflection properties of the structure at every pass of a

THz pulse, provided the pump intensity is actuated as quickly.

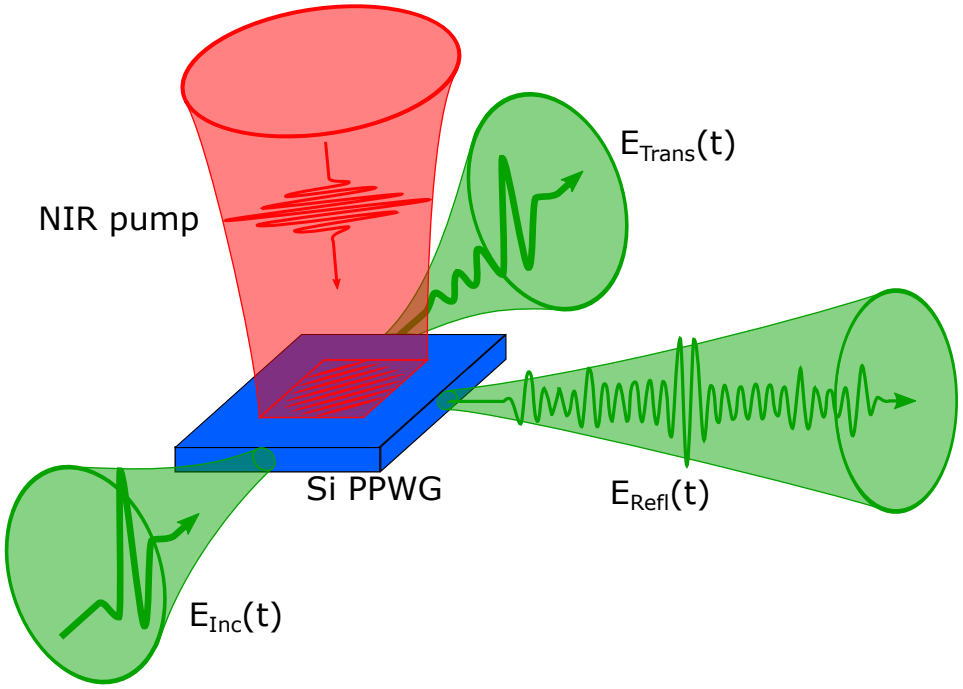

FIGURE 1.4: Schematic drawing of the silicon PPWG with a THz pulse coupled in ($E_{Inc}(t)$), transmitted ($E_{Trans}(t)$) and reflected ($E_{Refl}(t)$) as well as the optical pump (red). The patterned pump excitation creates a pulse-shaped reflected waveform.

The couple of following chapters (Ch. 2 & 3) focus on the underlying theory behind the experiments performed during this thesis and the experimental methods used to gather and analyse the data. We then present three manuscripts published in journals of the Optical Society of America. The first focuses on the dynamic creation of a gapless 1-dimensional photonic structure and on the transmission properties of this structure. In the article we discuss the properties of the Bragg resonator and the phase and group delay generated by the curvature of the photonic band near resonance. The second published work focuses on the pulse shaping capabilities of this platform in the reflection geometry. In the article we demonstrate linewidth and frequency tuning of THz frequency combs as well as the ability to encode information in the THz waveform by digitally encoding an 8-bit array into a THz waveform. The third manuscript presented focuses on the pulse shaping capabilities as well but on the phase tuning component. We show the ability to arbitrarily tune the CEP of the reflected pulse as well as the ability to generate THz waveforms with arbitrary chirp, both positive and negative. We conclude by presenting preliminary data recorded using this platform, namely: time-to-space mapping, two-dimensional photonic crystal structures, and driving and resolving pulse revivals from non-adiabatically switched rotational wave packets in water molecules.

We hope this manuscript will convince the readers that the pulse shaping capabilities of the platform demonstrated in the following work go far beyond the versatility demonstrated by any other platform in the THz regime [110, 142–144]. Its versatility and performance make it an excellent source of arbitrarily-shaped THz waveforms, a truly enabling tool for experiments aiming at controlling the state of matter as well as physical and chemical systems using THz radiation.

Chapter 2

Terahertz spectroscopy and light-matter interactions

In this chapter, we will discuss THz generation, detection, waveguiding and spectroscopic techniques used in this thesis. First, we will discuss THz time domain spectroscopy (THz-TDS), the technique with which the measurements are performed. We will cover the basics of second-order optical rectification and electro-optic sampling, with which we generate and detect our signals, respectively. We will then treat THz propagation inside a parallel-plate waveguide and give a brief overview of the Drude model, which is essential to understanding the pump-probe extension of THz-TDS used to interact with the THz waveforms in this work. We also discuss the Fabry-Pérot interferometer and its extension to describe the physics underlying our work. Summary derivations are presented here but we encourage readers who seek further understanding to look through a great collection of books and review articles in the literature [145–148, 185–188].

2.1 Time domain THz spectroscopy

2.1.1 Classical THz generation methods

Perhaps the first easily available source of coherent broadband THz radiation was first presented in pioneering work done by Auston et al. [5]. As discussed in chapter 1, these sources were originally used in transmission lines and evolved and became more commonly known as

photoconductive switches [149–151]. In essence, the switch can be viewed as a discharging dielectric-filled parallel-plate capacitor. A femtosecond pump focussed between the plates introduces charge carriers that are swept between the anode and cathode by an applied DC bias. The principle of operation can be understood by the wave equation:

$$\nabla^2 \mathbf{E} = \epsilon\mu \frac{\partial^2 \mathbf{E}}{\partial t^2} + \mu \frac{\partial}{\partial t} \left(\mathbf{J}_{conduction} + J_{bound} \right). \tag{2.1}$$

It is easy to see that if we consider a non-uniform motion of charge (i.e. $(\partial \mathbf{J}_{conduction}/\partial t \neq 0)$) the resultant is a non-zero propagating electric field. This way, the charge carriers induced inside the biased antenna are swept on ultrafast timescales result in a pulsed electromagnetic field in the far infrared.

Though antennas are still commonly used, the most prevalent way of generating broadband THz waveforms with μJ [152] or even mJ [153] pulse energies is through optical rectification of a near-infrared (NIR) pulse inside a second-order non-linear crystal. The first demonstration of this effect in the far infrared was made in the group of Yuen-Ron Shen [154] in 1971 using a $LiNbO_3$ crystal illuminated by a picosecond laser source. The most common crystal used for this type of experiment is perhaps Zinc Telluride (ZnTe) due to its high efficiency, 0.1 to 3 THz generation bandwidth, colinear emission geometry and good phase matching at 800 nm [155] where Ti:sapphire based femtosecond laser sources are readily available. In this work we employ tilted NIR pulse-fronts in $LiNbO_3$, a slightly more convoluted method, to generate high electric field THz waveforms, though the fundamentals remain the same as in ZnTe. The nonlinear polarization due to an applied time-varying electric field can be described perturbatively through a Taylor expansion:

$$P(t) = P_0 + \chi^{(1)} E(t) + \chi^{(2)} E^2(t) + \chi^{(3)} E^3(t) + ... \tag{2.2}$$

Here, P_0 is the built-in polarization of the material in the absence of static charges, $\chi^{(n)}$ is the n^{th} order electric susceptibility tensor component and $E(t)$ is the electric field amplitude. It is important to note that though χ is a small number, a non-linear material may exhibit $\chi^{(n+1)} > \chi^{(n)}$ near resonance in which case the higher-order susceptibility terms must be accounted for [189]. Furthermore, due to symmetry considerations, only non-linear materials that do not possess inversion symmetry will exhibit second-order effects. This property is a consequence

of the inversion operator $\mathbf{S}$ for which $\mathbf{S} \cdot \hat{\mathbf{e}} = -\hat{\mathbf{e}}$ for an arbitrary vector $\hat{\mathbf{e}}$ inside an inversion symmetric medium. This result yields $\chi^{(2)} = -\chi^{(2)}$ for which the only physical solution is $\chi^{(2)} = 0$ [189]. Lithium Niobate, which is used in this work to generate THz waves, has a trigonal crystalline lattice which lacks inversion symmetry. We neglect the third-order term and introduce two time-varying electric fields of the form $E_1(t) = \cos(\omega_1 t)$ and $E_2(t) = \cos(\omega_2 t)$ into Eq. 2.2. Neglecting the imaginary terms which only contributes to absorption, the time-dependent polarizability can be reduced to:

$$P^{(2)}(t) = \frac{\chi^{(2)}}{2} \left[\cos\left(\left[\omega_1 + \omega_2\right] t\right) + \cos\left(\left[\omega_2 - \omega_1\right] t\right)\right] \tag{2.3}$$

Equation 2.3 may be familiar to the readers as the first term represents second harmonic generation, or frequency doubling. In the continuous wave (CW) case ($\omega_1 = \omega_2$), the second term is often dismissed as it only contributes to a DC field component. If we consider a femtosecond pulsed laser system with typical characteristics for a Ti:sapphire amplifier cavity we expect to have an input bandwidth frequency-centered at 375 THz (800 nm) with equally separated modes separated by the cavity repetition rate (100 Hz - 100 kHz). The frequencies generated from the mixing between modes of this frequency comb, whether through second harmonic generation (SHG) or difference-frequency generation (DFG), will always be separated by the same comb spacing as illustrated in Fig. 2.1. The maximal bandwidth of the generated pulses will be dictated by the input bandwidth, which is limited by the gain bandwidth of the laser cavity. Figure 2.1 illustrates the generation of a THz pulse through DFG. The modes within the THz bandwidth are given by any combination of the modes within the NIR input pulse.

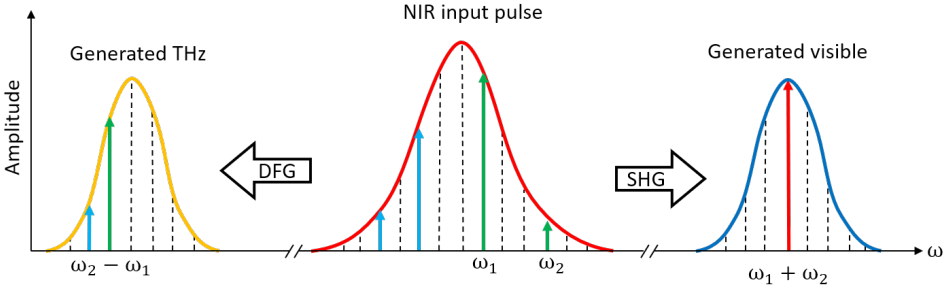

FIGURE 2.1: Schematic process of optical rectification and second-order frequency generation of a broadband pulse. The dashed lines represent the frequency comb of the laser cavity.

One of the conditions required for this process to work efficiently is of course that the group velocity of the NIR pulse be the same as the phase velocity of the THz wave inside the non-linear

material. This is what is referred to as the phase-matching condition and in summary it ensures that the generated frequency-difference term (our THz light) is added coherently through the entire thickness of the generation medium. In order to derive the mathematical expression dictating phase matching, we need to first solve the wave equation for the electric field DFG in the slowly varying amplitude approximation which yields [190, 156]

$$E(\Omega, z) = \frac{\Omega^2 e^{ik(\omega)L}}{k(\Omega)c_0^2} \int_{-\infty}^{\infty} \chi_{eff}^{(2)}(\Omega) A(\omega + \Omega) A^*(\omega) \frac{e^{i\Delta k(\omega,\Omega)z} - 1}{\Delta k(\omega, \Omega)} d\omega. \tag{2.4}$$

Here, Ω and ω are the THz and NIR angular frequencies, respectively, L is the length of the nonlinear crystal, $\chi_{eff}^{(2)}$ is the effective second-order susceptibility and $A(\omega)$ is the complex spectral field amplitude. We note that this expression is only valid if the pump is not significantly depleted or modified by the DFG process and explicitly depends on the phase mismatch between the THz and NIR frequencies [157]:

$$\begin{aligned}
\Delta k(\omega, \Omega) &= \frac{1}{c_0} \left((\omega + \Omega) \cdot n(\omega + \Omega) - \omega \cdot n(\omega) - \Omega \cdot n(\Omega) \right) && \text{(2.5a)} \\
&\simeq \frac{\Omega}{c_0} \left(n(\omega) + \omega \frac{dn(\omega)}{d\omega} - n(\Omega) \right) && \text{(2.5b)} \\
&\simeq \frac{\Omega}{c_0} \left(n_g(\omega_0) - n_p(\Omega) \right) && \text{(2.5c)} \\
& && \text{(2.5d)}
\end{aligned}$$

Which, simply states that the group index at NIR frequencies must match the THs phase index. The approximation made here is valid for the case where the NIR bandwidth is small compared to its center frequency ($\Delta\omega \ll \omega_0$). With this same approximation, we can rewrite eq. 2.4 in the form:

$$E(\Omega, z) = \frac{\Omega^2 e^{ik(\omega)L}}{k(\Omega)c_0^2} \chi_{eff}^{(2)}(\Omega) \frac{e^{i\Delta k(\omega,\Omega)z} - 1}{\Delta k(\omega, \Omega)} C(\Omega) \tag{2.6}$$

where $C(\Omega) = \int A(\omega + \Omega) A^*(\omega) d\omega$ is the autocorrelation function of the pump beam. It is also important to consider how well a material can convert photons from the NIR to THz frequencies. It is then easy to observe that a well phase matched material, yielding a low Δk, yields greater

field amplitudes. We can define the conversion efficiency η_{THz} with which the NIR light is converted as [158]

$$\eta_{THz} = \frac{2I(d_{eff}L\Omega)^2}{\epsilon_0 n_{NIR}^2 n_{THz} c_0^3} e^{-\alpha_{THz}L/2} \cdot \frac{\sinh^2(\alpha_{THz}L/4)}{(\alpha_{THz}L/4)^2}. \tag{2.7}$$

Here I is the NIR light intensity, d_{eff} is the effective nonlinear coefficient of the medium, L is the length of the medium, Ω is the angular (THz) frequency, ϵ_0 is the vacuum permittivity, n_{NIR} is the group index in the NIR, n_{THz} is the phase index at THz frequencies, c_0 is the speed of light and α_{THz} is the absorption coefficient of the medium at THz frequencies. We note that d_{eff} is simply the tensor component of $\chi^{(2)}$ relevant to efficient second-order frequency mixing processes in the crystalline axis employed. This equation can be simplified in the case of negligible absorption ($\alpha_{THz}L \ll 1$) to

$$\eta_{THz} = \frac{2I(d_{eff}L\Omega)^2}{\epsilon_0 n_{NIR}^2 n_{THz} c_0^3}. \tag{2.8}$$

In the case where absorption is considerable ($\alpha_{THz}L \gg 1$), the equation simplifies to

$$\eta_{THz} = \frac{8I(d_{eff}\Omega)^2}{\epsilon_0 n_{NIR}^2 n_{THz} c_0^3 \alpha_{THz}^2}. \tag{2.9}$$

The last two equations point to the fact that the generation efficiency scales as the square of the length of the medium L as long as its length remains smaller than that of the penetration depth of the THz light ($1/\alpha_{THz}$). Because of the vanishing dependence on crystal thickness, there is no benefit to generating THz in the case described in eq. 2.9. Furthermore, the efficiency scales linearly with incident intensity, though we would like to point out that this equation does not take into account the damage threshold specific to the generation crystal. More discussion on the properties of the most widespread crystals used in THz generation can be found in ref. [158] alongside figures of merit for energy conversion efficiency of these crystals.

Phase matching is indeed increasingly harder to achieve with wider bandwidths and thus crystals used for ultra-broadband THz generation are generally thinner than their narrowband counterparts. For example, 0.5 - 1 mm thick ZnTe crystals yield a bandwidth spanning from 0.1 to 3 THz and are extremely widespread; though a 30 μm thick ZnTe crystal can generate frequencies up to 37 THz [8], at the cost of over one order of magnitude in conversion efficiency. It is also

important to mention that this process emits radiation through bound charge carrier displacement and the far field solution of Eq. 2.1 thus yields $\frac{\partial \mathbf{J}_{bound}}{\partial t} = \frac{\partial^2 \mathbf{P}}{\partial t^2}$; meaning that the envelope of the THz field should be dictated by the bound charge carrier displacement which follows the envelope of the pulsed NIR excitation. The implications being that whether considering the frequency difference picture or the wave formalism, the achievable THz bandwidth is intimately linked to the input laser bandwidth and pulse duration.

For this research, the tilted pulse-front method is employed to generate single-cycle broadband high peak-field THz waveforms [38, 159, 160]. This method is chosen not for its simplicity but because the d_{eff} value of $LiNbO_3$ is of 168 pm/V whereas that of ZnTe is of 68.5 pm/V [161] allowing for energy conversion efficiencies of 10^{-3} [153, 162, 163] whereas ZnTe generally only provides efficiencies on the order of 10^{-5} [164]. One of the most staggering things about this generation method is the fact that quantum conversion efficiencies, meaning the number of times infrared photons are used to generate THz photons, can be in excess of 1, exceeding the Manley-Rowe limit [159]. In fact, due to a cascaded process, NIR photons can be recycled and reused multiple times manifesting as a significant red-shifted tail in the transmitted pump pulse spectrum [153].

Though $LiNbO_3$ boasts an impressive nonlinear coefficient, it most certainly does not respond to the phase matching criteria established earlier with a NIR group index value of 2.26 [165] and a THz phase index value of 4.96 [166] at 1 THz. This obstacle is circumvented by tilting the angle NIR of the pulse front in order to match the velocity of both wavefronts. Note that the NIR and THz frequencies do not travel at the same speed due to the refractive index mismatch but adequate pulse front tilt insures coherent addition of THz radiation and thus phase matching. The general principle of operation of tilted pulse-front optical rectification inside $LiNbO_3$ is relatively simple to understand. Consider the Huygens-Fresnel principle for the wavefront of a propagating electromagnetic field where every point along this front can be considered as a point emitter. This picture is often used to illustrate the diffraction of waves inside slits or around sharp objects and is just as suited for this example. If we consider the case depicted in Fig. 2.2 where a slice of a pulse propagates inside a material where NIR light is significantly faster than THz light, the THz waveform generated via optical rectification should be emitted in a cone shape in the manner of Cherenkov radiation. The cone angle can be simply calculated using the formula

$$\theta = \arccos\left(c_{THz}/c_{NIR}\right) = \arccos\left(n_{NIR}/n_{THz}\right) \tag{2.10}$$

which yields a value of $\theta = 63°$ at 800 nm. The experimental configuration and challenges used to achieve this tilt angle will be discussed in chapter 3. Note that this picture is also perfectly analogous to breaking the sound barrier where an object, a fighter jet for example, is travelling faster than the speed of sound in the medium. In the case illustrated in subfigure 2.2a), we consider a slice of a flat NIR wavefront, depicted in red, perfectly perpendicular to its direction of propagation. By considering the THz wavelets emitted at each wavefront extremity, sketched in yellow and green here, we can see that no significant overlap is achieved between the top and lower portions of the wavefront. Now, if instead tilt the angle of the propagating NIR wavefront, as depicted in red in subfigure 2.2b), and match the angle of the tilt to that of the Cherenkov cone, we can achieve significant overlap between wavelets from each extremities, depicted in yellow and green. This coherent addition results in extremely efficient THz generation, represented by the green arrows. This clever way of achieving phase matching between NIR and THz frequencies in $LiNbO_3$ has allowed experimentalists to harness its large second order nonlinearity, high damage threshold and large bandgap which supresses parasitic two-photon absorption. Tilted pulse-front THz generation in $LiNbO_3$ has been one of the foundations over which non-linear THz spectroscopy has been expanding over the last decade. If the readers seek further reading on this subject, the literature is teeming with excellent work and reports [38, 153, 159, 160, 162] and experimental observations of this effect [167, 168].

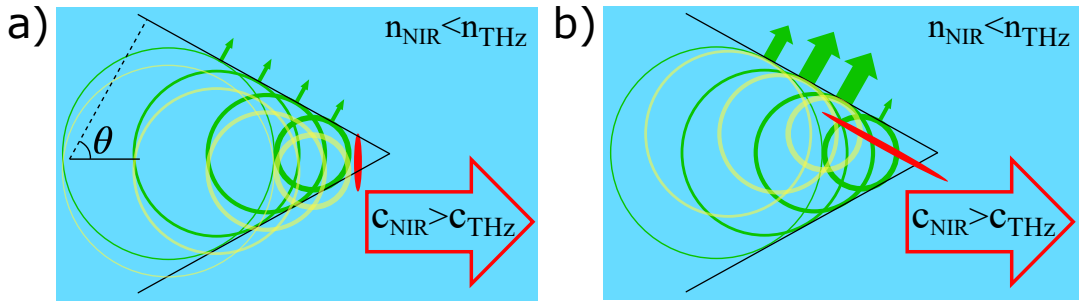

FIGURE 2.2: a) Schematic representation of the wavelet emission (yellow and green circles) from a slice of a NIR pulse (red) propagating inside a higher-index medium. b) Depiction of the same scenario where the wavefront has been tilted to match the angle of the emission cone.

2.1.2 Free-space electro-optic detection

As mentioned in chapter 1, photoconductive switches were originally developed in the THz domain to be used both as emitters and as detectors of far infrared radiation. In 1996 though, a new method of detection was demonstrated almost simultaneously by three different groups

[169–171] and would soon become the standard THz-TDS detection scheme. This method, now better known as electro-optical detection, or EO detection for short, uses the Pockels effect inside a non-linear crystal to imprint the THz amplitude and phase onto the polarization state of a NIR beam. The working principle behind this technique is illustrated in Fig. 2.3 and requires overlapping a NIR pulse with a THz pulse both spatially and temporally inside an electro-optically active medium. We can first consider the simple case of subfigure 2.3a) where no THz is present. The linearly polarized NIR pulse, or gating beam, is incident onto an EO crystal after which its polarization is modified to circular using a quarter waveplate ($\lambda/4$). Both orthonormal polarization components are then separated and detected by individual photodiode detectors. Careful alignment, balancing and compensation for the EO crystal's inherent birefringence should yield equal amounts of light in each diode thus equal voltage readings. Now, if we consider overlapping a pulsed THz electric field with our gating beam, as illustrated in subfigure 2.3b), the Pockels effect induced by the THz electric field results in a polarization rotation in the gating beam inside the EO crystal. We note that this is, just like for optical rectification, only satisfied if the phase matching condition is met for both THz and NIR bandwidths. Same as for generation, broader detection bandwidths can generally be achieved by using thinner crystals. The advantage of using the Pockels effect is that the direction of rotation of the NIR polarization is sensitive to the field direction. In other words, if the THz field is pointed up, as in Fig. 2.3b), the polarization will be rotated to the right. If however the instantaneous electric field is pointed downwards, the polarization would be rotated to the left. This way, the THz electric field can be directly mapped onto the NIR polarization. This phase retardation φ is given by

$$\sin(\Delta\varphi) \simeq \Delta\varphi = \frac{\omega L}{c_0} n_O^3 r_{41} E_{\mathrm{THz}} \tag{2.11}$$

where ω is the angular frequency of the gating beam, L is the length of the EO medium, n_O is the refractive index at NIR frequencies, r_{41} is the electro-optic coefficient of the detection crystal and E_{THz} is the instantaneous THz electric field [185]. We note that this relation is only valid if $\Delta\varphi \ll 1$, which is generally the case, but one needs to attenuate E_{THz} by a known amount with field strengths above $\sim$ 15 kV/cm assuming using a 0.5 mm thick ZnTe crystal with 4 pm/V electro-optic coefficient in order to get a sensible field calibration when using a $LiNbO_3$ source. Accordingly, the phase retardation, or polarization rotation, is transformed into an elliptical polarization by the quarter waveplate, as illustrated in Fig. 2.3.b) and delivered as an imbalance between the orthonormal polarization components to the photodiodes. This imbalance is directly proportional to E_{THz} and also sensitive to its phase. By doing careful

voltage measurements, typically using a lock-in amplifier, it is then possible to retrace the THz waveform by stepping its temporal overlap with the gating beam, just like in a temporal correlation measurement. Again, it is important to emphasize that this technique gives direct access to the phase of the field eliminating the need to resort to Kramers-Kronig relations and fastidious calculations generally required to extract both components of an optical response function.

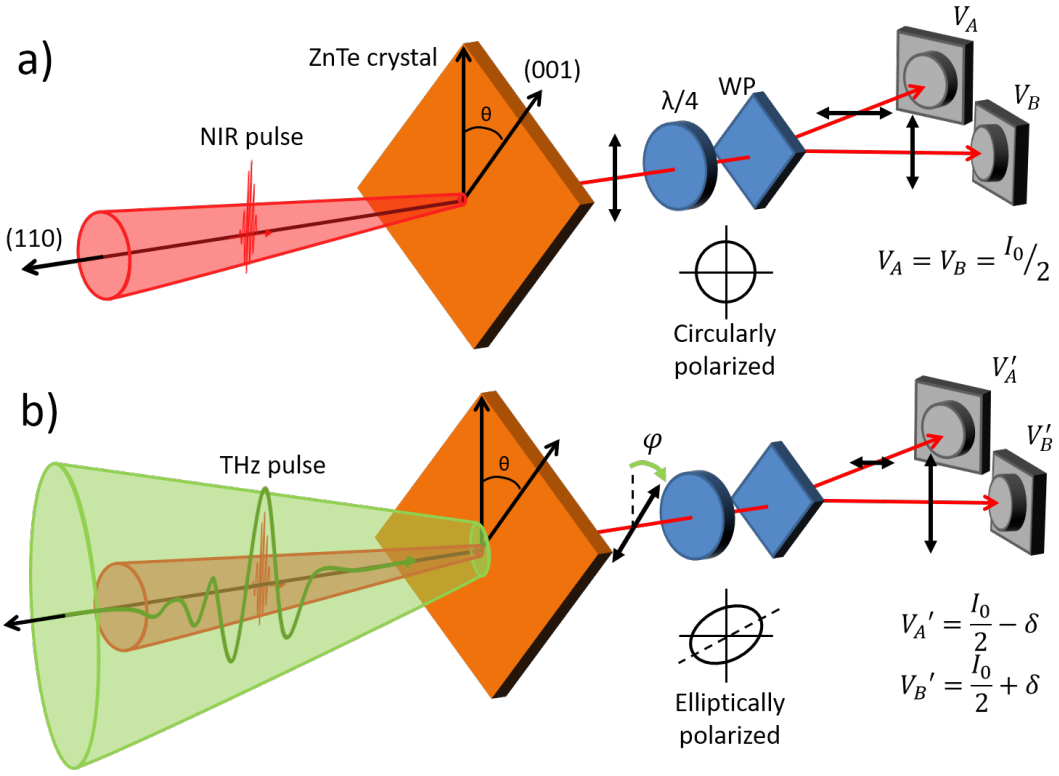

FIGURE 2.3: Schematic of the THz and gating pulse polarization for electro-optical detection in ZnTe where the quarter waveplate is labelled $\lambda/4$ and the Wollaston prism is labelled WP.

As with all detection methods, one must consider the response function of the detector, which depends on three factors in the case of OE sampling [185]. First, transverse optical (TO) phonons have a significant impact over the second-order non-linear susceptibility causing it to shift greatly in the vicinity of its resonance [172]. The second one is subtler and involves the autocorrelation (A_{Opt}) of the gating pulse's electric field (E_{Opt}) which is given by

$$A_{Opt}(\omega_{THz}) = \int_{-\infty}^{\infty} E^*_{Opt}(\omega' - \omega) E_{Opt}(\omega' - \omega - \omega_{THz}) d\omega'. \tag{2.12}$$

What this integral expresses is the decrease in efficiency as NIR light is red-shifted away from

its initial spectrum content as a by-product of optical rectification and emission of THz radiation inside the detection crystal. Again, this term is intimately linked to the phase matching condition and to the thickness of the EO medium. The third factor that must be considered is the frequency filtering $\Delta\Phi$ that arises due to the mismatch in THz and NIR velocity inside the detection crystal

$$\Delta\Phi(\omega, \omega_{THz}) = \frac{e^{i\Delta k(\omega,\omega_{THz})D} - 1}{i\Delta k(\omega, \omega_{THz})}. \tag{2.13}$$

This last term shows a dependence on the wavevector mismatch Δk and again on the thickness of the OE medium D. The combination three of these factors is presented in Fig. 2.4 for a 13 μm thick GaP crystal [172]. We note the presence of a sharp dip in the response function at 8 and 40 THz due to TO phonons in GaP [173, 191], though the region of interest in those experiments entirely lies in the flat response region below 4 THz primarily due to the bandwidth limitations of our generation method. Readers interested in the calculations and derivations relevant to electro-optical sampling in the commonly used ZnTe can find an excellent example in an article by P. Planken, see Ref. [174].

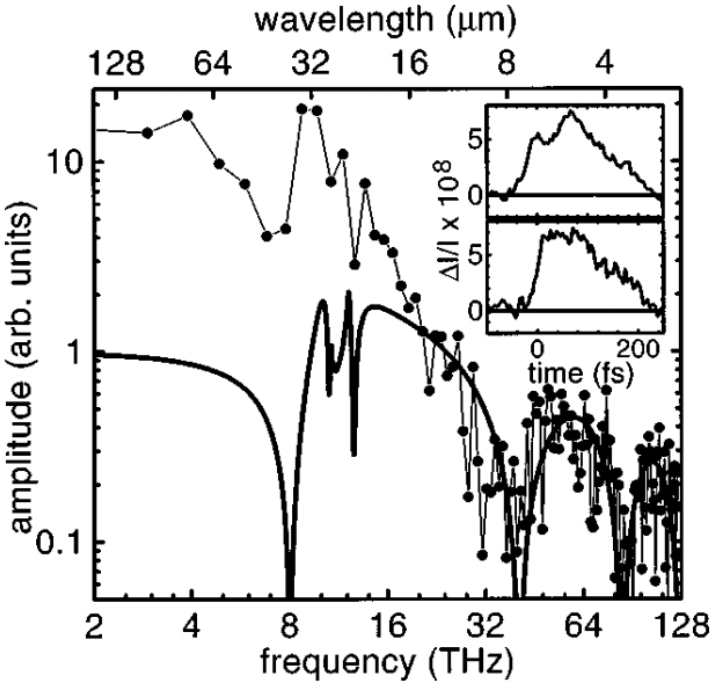

FIGURE 2.4: Measured spectrum collected by a 13 μm thick GaP crystal and emitted by a GaAs *p-i-n* diode (connected dots). Calculated response function of the thin GaP crystal including dispersion and phonon coupling considerations (thick solid line) [172].

2.2 THz parallel-plate waveguide

As with all good things in the realm of electro-dynamics, the derivation of the equations governing light inside waveguides begins with Maxwell's equations. When expressed in SI units, using bold characters to represent vector quantities, these take the form

$$\nabla \cdot \mathbf{E} = 0 \tag{2.14a}$$

$$\nabla \cdot \mathbf{H} = 0 \tag{2.14b}$$

$$\nabla \times \mathbf{E} = -\mu_0 \frac{\partial \mathbf{H}}{\partial t} \tag{2.14c}$$

$$\nabla \times \mathbf{H} = \mathbf{J}_f + \frac{\partial \mathbf{D}}{\partial t} \tag{2.14d}$$

where $\mathbf{J}_f$ is the free charge carrier current density and $\mathbf{D}$ denotes the electric displacement field. As a reminder, the electric and displacement fields are related through the relation $\mathbf{D} = \tilde{\epsilon}\mathbf{E} + \mathbf{P}$ where $\tilde{\epsilon}$ is the complex electric permittivity and $\mathbf{P}$ is the polarization. As we wish to express travelling electromagnetic waves for a time-domain spectroscopy experiment it is advantageous to represent the magnetic field $\mathbf{H}$ and electric field $\mathbf{E}$ as

$$\mathbf{E}(x, y, z, t) = \mathbf{E}_0(x, y)e^{i(kz-\omega t)} \tag{2.15a}$$

$$\mathbf{H}(x, y, z, t) = \mathbf{H}_0(x, y)e^{i(kz-\omega t)}. \tag{2.15b}$$

The axis choice taken here is presented in Fig. 2.5. Using the wave equations and inserting them into Maxwell's equations one can find the following after decoupling $\mathbf{E}_0$ and $\mathbf{H}_0$:

$$\left[\frac{\partial^2}{\partial y^2} + \frac{\partial^2}{\partial x^2} + (\omega/c)^2 - k^2\right] \mathbf{E_0} = 0 \tag{2.16a}$$

$$\left[\frac{\partial^2}{\partial y^2} + \frac{\partial^2}{\partial x^2} + (\omega/c)^2 - k^2\right] \mathbf{H_0} = 0. \tag{2.16b}$$

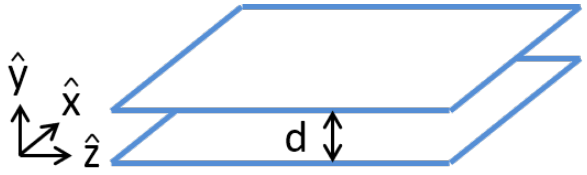

FIGURE 2.5: Axis definitions for the parallel-plate waveguide.

When this derivation is made in the literature, two general families of solutions arise to this problem which are referred to as transverse electric (TE) or transverse magnetic (TM) modes. These occur when $E_y = E_z = 0$ in the TE case and $H_y = H_z = 0$ for TM modes. Here, the subscript denotes the component of the field parallel to the axis defined in Fig. 2.5. The chosen configuration for our experiments is that of the TM modes where the magnetic field is always parallel to the x-axis. This lets us define a plane wave solution of the form $\mathbf{H}_0(x, y) = Y(y)e^{-ikz}\hat{\mathbf{x}}$ which, inserted into Eq. 2.16b) yields a solution of the form

$$\frac{\partial^2 Y}{\partial y^2} + \left[(\omega/c)^2 - k^2\right] Y = 0. \tag{2.17}$$

This familiar differential equation of course yields a sinusoidal solution which, once we apply continuous magnetic field boundary conditions at the magnetic plates, gives

$$\mathbf{H} = H_0 \cos\left(\frac{m\pi}{d}y\right) e^{-ikz}\hat{\mathbf{x}} \tag{2.18}$$

where d is the plate separation, like in Fig. 2.5, and m is a positive integer representing the mode number. Using Ampère's law we can derive the electric field equation which is expresses in the form

$$\mathbf{E} = \frac{-iH_0}{\omega\epsilon}\left[-\frac{m\pi}{d}\sin\left(\frac{m\pi}{d}y\right)\hat{\mathbf{z}} + ik\frac{m\pi}{d}\cos\left(\frac{m\pi}{d}y\right)\hat{\mathbf{y}}\right] e^{-ikz}. \tag{2.19}$$

What is interesting to note is that for TM modes there exists an $m = 0$ solution often referred to as the transverse electro-magnetic mode (TEM). For any other mode ($m = 1, 2, 3, ...$), there exists a cutoff frequency ν_c under which no propagation is allowed

$$\nu_c = \frac{\omega_c}{2\pi} = \frac{mc_0}{2nd}. \tag{2.20}$$

This cutoff is a function of the mode number m, of the plate separation d and of the refractive index inserted between the plates n. At frequencies below its respective cutoff, a mode will simply decay exponentially along the propagation axis. Because of this resonance, the phase and group velocities (v_ϕ & v_g, respectively) dramatically change in the vicinity of this resonance

$$v_\phi = \frac{c_0}{n}\sqrt{1-\left(\frac{\omega_c}{\omega}\right)^2} \tag{2.21a}$$

$$v_g = \frac{c_0}{n\sqrt{1-\left(\frac{\omega_c}{\omega}\right)^2}}. \tag{2.21b}$$

This results in a great amount of dispersion on top of the cutoff issue. The truly interesting fact about the 0^{th} mode is that on top of having no low-frequency rejection band it is completely dispersionless. What this means for us is that we can input a single-cycle pulse of arbitrarily wide bandwidth and collect the same bandwidth at the waveguide output, as long as we couple into and stay in this TEM mode. There exist certain experimental limitations to the coupling bandwidth but we will address those in chapter 3.

2.3 Free carriers and the Drude model

The all-optical approach to modulating light is, evidently, the fastest imaginable method that can be used to actuate a THz signal. This actuation cannot however be done directly through photon-photon interactions as their bosonic nature prevents such interactions. Therefore, we must rely on a material to mediate the influence of our trigger, or pump, on the THz signal. The method chosen for the experiments presented in this work relies on free carrier excitation inside a semiconductor-filled waveguide. As discussed in the previous subsection, the use of the TEM guided mode allows for free-space-like propagation of a broadband pulse inside a dielectric environment. By using a pump excitation wavelength above the bandgap of our semiconductor, high-resistivity float-zone silicon in this case, we can promote charge carriers from the valence to the conduction band and thus induce a change in the dielectric environment of the guided THz pulse. In this section, we present the Drude model, which provides an intuitive approach to deal with the dielectric properties of a band semiconductor. To derive these equations, we will first consider the Newtonian equation of motion for a charged particle of effective mass m^* moving at a velocity $\mathbf{v}$ inside a time-dependant electric field $\mathbf{E}(t)$ and having a dampening collisional momentum rate of $1/\tau$

$$m^*\frac{d\mathbf{v}(t)}{dt} = -\frac{m^*\mathbf{v}}{\tau} - e\mathbf{E}(t). \tag{2.22}$$

By inserting the definition of the current density $\mathbf{J} = -Ne\mathbf{v}$ where N is the density of charge carriers and by assuming an oscillating electric field and current density of the form $\mathbf{J}(t) = \mathbf{J}_0 e^{i\omega t}$ we find the relation

$$i\omega \mathbf{J}_0 e^{i\omega t} + \mathbf{J}_0 e^{i\omega t} = \frac{ne^2}{m^*} \mathbf{E}_0 e^{i\omega t}. \tag{2.23}$$

It then becomes easy to extract both real and imaginary parts of the conductivity ($\tilde{\sigma} = \sigma_1 + i\sigma_2$) knowing that $\mathbf{J} = \sigma \mathbf{E}$:

$$\sigma_1 = \frac{\sigma_{dc}}{1 + (\omega\tau)^2} \tag{2.24a}$$

$$\sigma_2 = \omega\tau \frac{\sigma_{dc}}{1 + (\omega\tau)^2}. \tag{2.24b}$$

Here, we have introduced the DC conductivity $\sigma_{dc} = \dfrac{Ne^2\tau}{m^*}$ which is dependent on the charge carrier density N. We note that the relaxation time τ is generally on the order of 50×10^{-15} s in float-zone silicon and the effective valley-averaged mass m^* of 0.26 m_e for the electrons and of of 0.37 m_e for the holes [175], where m_e is the vacuum electronic mass. The number used for the carrier density are dependant on the pump characteristics, geometry and intensity and will be discussed in the experimental methods in chapter 3. It is also useful to introduce the plasma frequency, which is given by

$$\omega_p = \sqrt{\frac{Ne^2}{m^* \epsilon_0}}. \tag{2.25}$$

This quantity is associated to the collective excitation of the plasma which can occur when $\epsilon_1 = 0$; this occurs at $\omega = \omega_p$ for the Drude model.

Given the conductivity equations defined in Eq. 2.24, which are expressed in terms of measurable quantities, the complex relative electric permittivity knowing that $\tilde{\epsilon}(\omega) = \epsilon_B + \dfrac{i\tilde{\sigma}}{\epsilon_0 \omega}$

$$\epsilon_1 = \epsilon_B - \frac{\tau\sigma_{dc}}{\epsilon_0\left[1+(\omega\tau)^2\right]} \tag{2.26a}$$

$$\epsilon_2 = \frac{\sigma_{dc}}{\epsilon_0\omega\left[1+(\omega\tau)^2\right]} \tag{2.26b}$$

where it has been decomposed in its real and imaginary parts. Here ϵ_B denotes the background permittivity. Remembering the relation $\tilde{\epsilon} = \epsilon_1 + i\epsilon_2 = \tilde{n}^2 = (n+i\kappa)^2$ the real and imaginary parts of the refractive index (n & k, respectively) are given by

$$n = \frac{1}{\sqrt{2}}\sqrt{\epsilon_r - \frac{\sigma_{dc}\tau}{\epsilon_0}\frac{1}{1+(\omega\tau)^2} + \sqrt{\frac{\epsilon_r^2 + \left(\frac{\sigma_{dc}}{\epsilon_0\omega} - \epsilon_r\tau\omega\right)^2}{1+(\omega\tau)^2}}} \tag{2.27a}$$

$$\kappa = \frac{1}{\sqrt{2}}\sqrt{-\epsilon_r + \frac{\sigma_{dc}\tau}{\epsilon_0}\frac{1}{1+(\omega\tau)^2} + \sqrt{\frac{\epsilon_r^2 + \left(\frac{\sigma_{dc}}{\epsilon_0\omega} - \epsilon_r\tau\omega\right)^2}{1+(\omega\tau)^2}}} \tag{2.27b}$$

It is then possible to write a general solution for a propagating electric field in the presence of free charge carriers knowing that the wavevector is related to the refractive index via $\tilde{k} = \tilde{n}\omega/c_0$:

$$\mathbf{E}(x,y,z,t) = \mathbf{E}_0(x,y)e^{i(kz-\omega t)}e^{-\alpha z}. \tag{2.28}$$

Here we can see that the second exponential term introduces loss in the system due to the imaginary part of the refractive index. We've expressed it in terms of the field loss coefficient $\alpha_{field} = \frac{2\pi f\kappa}{c_0}$. In most of the literature, authors choose to express loss using the Beer-Lambert law which is expressed in units of power. Since amplitude is naturally measured in THz TDS, we opt to express this quantity in terms of field amplitude loss, which only differs by a factor of two in the exponent. Furthermore, this loss term can be expressed in terms of the penetration depth $\delta = 1/2\alpha$, the length after which the waveform intensity has diminished by $1/e$.

It is also useful to define the electron charge carrier mobility $\mu_e = \frac{e\tau}{m^*}$ which relates the drift velocity of an electron inside an applied electric field. This diffusion length l_D is given by the simple equation

$$l_D = \sqrt{Dt} \tag{2.29}$$

which depends on time t and on the diffusion coefficient D. This last quantity is a material property given by its ambipolar mobility μ_{ab} and which varies as a function of temperature T:

$$D = \frac{\mu_{ab} k_B \mathrm{T}}{e}. \tag{2.30}$$

We recognise here the elementary charge e as well as the Boltzmann constant k_B. The ambipolar mobility is defined as the collective mobility in the material in the case of an optically created equal population of electrons and holes. In this case, electrons and holes both contribute to give

$$\mu_{ab} = \frac{\mu_e \mu_h}{\mu_e + \mu_h} \tag{2.31}$$

where $\mu_h = 300\ \mathrm{cm}^2/\mathrm{Vs}$ and $\mu_e = 1000\ \mathrm{cm}^2/\mathrm{Vs}$; with heavy holes dominating the photocarrier diffusion characteristics for silicon at room temperature. We can thus use these quantities to evaluate the diffusion length scales relevant to our experiment. For example, a THz pulse takes 20 picosecond to transit through a photoinjected structure of typical size. Over this duration, carriers will diffuse over a length $l_D \simeq 100$ nm, much less than the 1 THz wavelength in silicon (88 μm) or the length scales of the photoinjected structures (20 μm). Another relevant timescale is the recombination time of the electrons and holes in silicon, which is on the order of 1 μs. Over this timescale, carriers will drift up to $l_D \simeq 20$ μm, thus washing out the structures and making the operation of this device impractical with a CW pump laser.

2.4 Bragg gratings and the transfer matrix method

When light is shone onto a mirror, it is reflected. What is less intuitive is that when a second mirror is inserted in the beam trajectory in the vicinity of the first mirror, certain frequencies are allowed to traverse. It is important to note that though the Fabry-Pérot equations describe very well the basics behind this simple interferometer they fall short when it comes to describing the more complex case of a distributed Bragg reflector, specially in the presence of dispersive media. For this, we use an analytical calculation method known as the transfer-matrix method which

accounts for the non-trivial phase change acquired by light upon reflection off a complex-indexed medium where $n \simeq k$. We do not wish to get bogged down in the details as many derivations can be found in optics textbooks but in summary the method relies on matrix formalism to propagate transmission parameters through various layers with independent material properties. If we consider light incident from material number 1 onto material number 2, the propagation matrix M_{12} can be described the interface interaction as

$$M_{12} = \begin{bmatrix} \dfrac{n_2 \cos\theta_2 + n_1 \cos\theta_1}{2n_2 \cos\theta_2} & \dfrac{n_2 \cos\theta_2 - n_1 \cos\theta_1}{2n_2 \cos\theta_2} \\ \dfrac{n_2 \cos\theta_2 - n_1 \cos\theta_1}{2n_2 \cos\theta_2} & \dfrac{n_2 \cos\theta_2 + n_1 \cos\theta_1}{2n_2 \cos\theta_2} \end{bmatrix} \tag{2.32}$$

for an isotropic medium. Here n_1 and n_2 are the refractive indices of materials 1 and 2 and θ_1 and θ_2 are the propagation angles with respect to normal of materials 1 and 2, respectively. Furthermore, we need to consider the phase delay acquired through each material using the matrix expression

$$P_2 = \begin{bmatrix} e^{ik_2 d} & 0 \\ 0 & e^{-ik_2 d} \end{bmatrix} \tag{2.33}$$

where k_2 is the wavevector of material 2 and d is the thickness of this material. For transmission from medium 1 to medium 3 through medium 2, one can then find the transmission and reflection solution using simple matrix multiplication:

$$M_{23} P_2 M_{12} \begin{bmatrix} E^{(1)}_{Trans} \\ E^{(1)}_{Refl} \end{bmatrix} = \begin{bmatrix} E^{(3)}_{Trans} \\ E^{(3)}_{Refl} \end{bmatrix}. \tag{2.34}$$

The power of this method lies in the ability to cascade matrix multiplications for increasing number of mediums considered. If we consider the case at hand where we photoinject charge carriers into a series of periodically repeating silicon regions, we can analytically calculate the total transmitted and reflected electric fields. For practical reasons, this is more easily done numerically and the solutions for a typical structure are presented in Fig. 2.6. The case considered has 20 lines of 20 μm thickness and a 160 μm pitch. The charge carrier density ($N \simeq 10^{16}$ cm^{-3}) yields a conductivity of 82 Siemens/m which equates to a plasma frequency ($\omega_p/2\pi$) of 2.3 THz. What is predicted and observed [176] is an increase in electric field transmission on resonance with a simultaneous increase in reflection. This is contradictory to the simple

case considered in the Fabry-Pérot interferometer and as we can also observe does not respect the Stokes relations ($R + T = 1$). This is due to the fact that in the case at hand $n \simeq k$ (ie. $\mathrm{Re}(n) \simeq \mathrm{Im}(n)$) which influences the phase change upon reflection at the photodoped silicon interfaces. This is further discussed in our published work presented in chapter 4. We note that though this analytical method makes very accurate predictions on the transmission and reflection amplitude of a device, it does not yield the time-domain solution to the electric field of the THz pulse. For this, we opt to primarily rely on finite-difference time-domain (FDTD) simulations to make predictions on the reflected THz waveform.

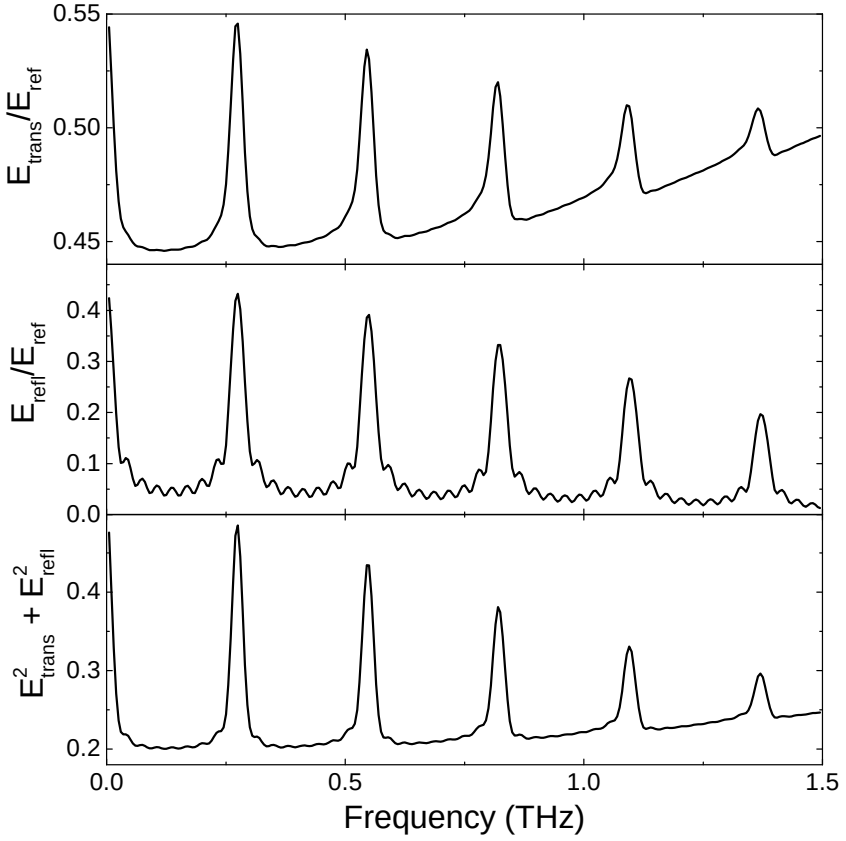

FIGURE 2.6: Electric field transmission (top) and reflection (middle) for a typical photoinjected structure with charge carrier density of $\sim 10^{16}$ cm^{-3}. (bottom) Intensity transmission and reflection sum (T+R).

2.4.1 Plasma-dielectric photonic band structure in one dimension

Another useful way to treat our experimental system is to calculate the dispersion relation, or photonic bands, for a one-dimensional plasma-dielectric stack. This derivation originates from an article by L. Shiveshwari and P. Mahto and a more detailed discussion can be found in ref. [177]. By considering alternating layers of plasma (photoexcited silicon) and dielectric (bare

silicon) of thickness a and b, respectively, with the permittivity of each region defined in Fig. 2.7. We recall ω_p, the plasma frequency defined in section 2.3 and we also define the structure period $d = a + b$.

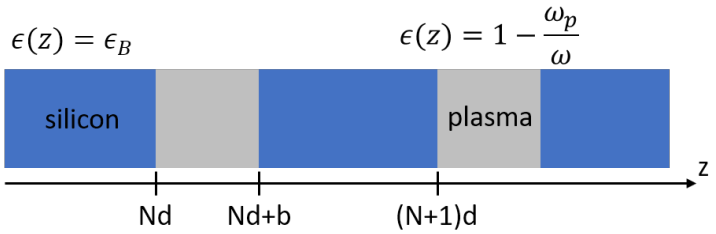

FIGURE 2.7: Schematic of the one-dimensional plasma-dielectric stack. The plasma is depicted in light grey and the dielectric, silicon, in blue. The axis defined the stack period and the dielectric constant of each material.

If we consider the case where $\omega < \omega_p$, which is most always the case in our experiments, the electric field can be written as:

$$E(z) = \begin{cases} B_N e^{ik_b(z-Nd-b)} + \bar{B}_N e^{-ik_b(z-Nd-b)} & \text{In bare silicon} \\ A_N e^{ik_a(z-(N+1)d)} + \bar{A}_N e^{-ik_a(z-(N+1)d)} & \text{In the plasma.} \end{cases} \tag{2.35}$$

Here, the wavevectors in silicon and in the plasma are given by $k_b = \frac{\omega}{c_0}\sqrt{\epsilon_B}$ and $k_a = \frac{\omega}{c_0}\sqrt{\frac{\omega_p^2}{\omega^2} - 1}$, respectively.

When considering unit cells N, we can write the boundary conditions to Maxwell's equations in the matrix form

$$\begin{bmatrix} B_N \\ \bar{B}_N \end{bmatrix} = M^N \begin{bmatrix} B_0 \\ \bar{B}_0 \end{bmatrix} \tag{2.36}$$

where B_N and $\bar{B}_N$ are the amplitude of the forwards and backwards propagating waves in cell N, respectively. Here M is a 2x2 transfer matrix, as defined in the previous section. By applying the laws of energy conservation and by using the time-reversal symmetry properties of Maxwell's equation we can extract the transmission coefficient of a 1D periodic structure, as detailed in ref. [178].

$$T_N = \left(1 + U_{N-1}^2 \left(\frac{1}{T_1} - 1\right)\right)^{-1} \tag{2.37}$$

In this equation, the Chebyshev polynomial of second kind is defined as

$$U_N = \frac{\sin(N+1)\phi}{\sin\phi} \tag{2.38}$$

where T_1 is the transmission through a single sub-unit and ϕ is the Bloch phase. Their solutions are given by

$$\phi = \arccos\left(\cosh(k_a a)\cos(k_b b) + \frac{1}{2}\left(\frac{k_a}{k_b} - \frac{k_b}{k_a}\right)\sinh(k_a a)\sin(k_b b)\right) \tag{2.39}$$

and

$$T_1 = \left(1 + \frac{1}{4}\left(\frac{k_a}{k_b} + \frac{k_b}{k_a}\right)^2 \sinh^2(k_a a)\right)^{-1}. \tag{2.40}$$

Since the dispersion relation of an infinite structure is given by the trace of the transfer matrix $cos(kd) = Tr(M)/2$, we find the dispersion relation for $\omega < \omega_p$:

$$\cos(kd) = \cosh(k_a a)\cos(k_b b) + \frac{1}{2}\left(\frac{k_a}{k_b} - \frac{k_b}{k_a}\right)\sinh(k_a a)\sin(k_b b). \tag{2.41}$$

By plotting the dispersion relation given by eq. 2.41 for a periodic structure with identical parameters as those used in section 2.4 ($a = 20$ μm and $b = 140$ μm), we find the band structure plotted in Fig. 2.8a). Here we have defined a plasma frequency ($\omega_p/2\pi$) of 3.4 THz which contributes to flattening the bands near resonance but do not open a gap in the dispersion relation as the Bragg condition is not fully met on-resonance ($n_a a \neq n_b b$). We also plot the electric field transmission as a function of frequency for the band calculation (Fig. 2.8b), black) alongside the transfer matrix calculation (red, from Fig. 2.6). We can see that both data sets match very well. The resonances of the band calculation show narrower linewidths as they depict the case of a structure with an infinite number of unit cells whereas the transfer matrix calculations are done for 20 unit cells. It is interesting to note that even for an infinite number of cells, the resonance linewidth is not infinitely sharp, contrary to what one would expect in the case of a lossless structure.

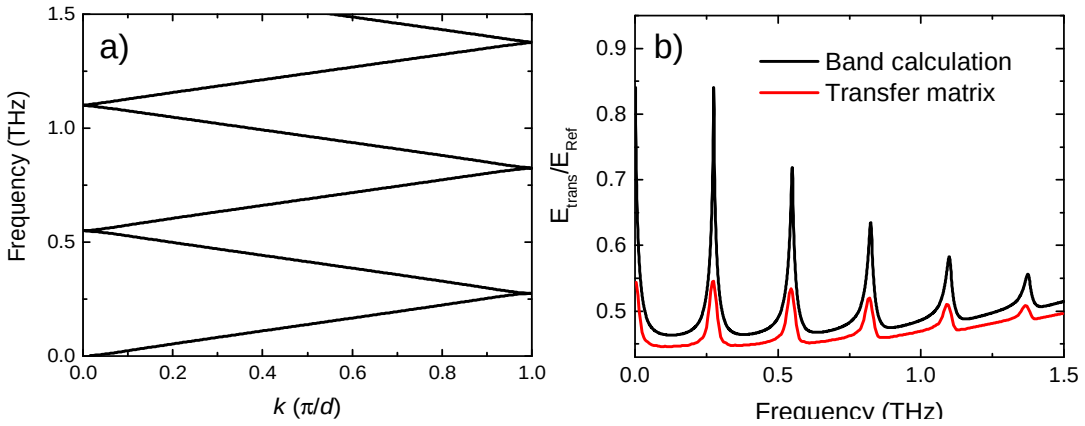

FIGURE 2.8: (a) Calculated dispersion curve in the first Brillouin zone. (b) Electric field transmission amplitude calculated from the dispersion curve of an infinite plasma-dielectric 1D photonic structure (black) and for a transfer-matrix method calculation (red). The plasma frequency $\omega_p/2\pi$ is fixed at 3.4 THz and the structure dimensions are (a = 20 μm and b = 140 μm).

Chapter 3

Experimental methods

In the following sections we will discuss the experimental methods used to gather the data presented in this thesis. We will present an overview of THz time-domain spectroscopy (TDS) including amplified NIR femtosecond pulse generation, tilted pulse-front optical rectification inside $LiNbO_3$ and the way they are used to perform THz-TDS as well as pump-probe time-resolved THz spectroscopy. We describe with some detail the few fabrication steps performed to fabricate our samples alongside the waveguide design parameters. We further discuss the experimental challenges and difficulties encountered and the steps taken to overcome them.

3.1 Amplified femtosecond Ti:sapphire laser system

As discussed in previous chapters, using femtosecond near-infrared pulses is an extremely convenient way to generate broadband single-cycle phase-locked pulses of THz radiation. Perhaps the most widespread method of obtaining short mJ level NIR pulses is through chirped-pulse amplification of a broadband low-intensity NIR pulse. This method has received a lot of attention in recent months following the 2018 physics Nobel prize awarded to Arthur Ashkin, Gérard Mourou and Donna Strickland. It is to the two latter-mentioned scientists that we owe this convenient method of generating high-intensity ultra-short pulses of light, schematically presented in Fig. 3.1. Since this method is extremely well described and vulgarized in the scientific and popular literature we will simply underline the characteristics of the lasers employed for our experiments.

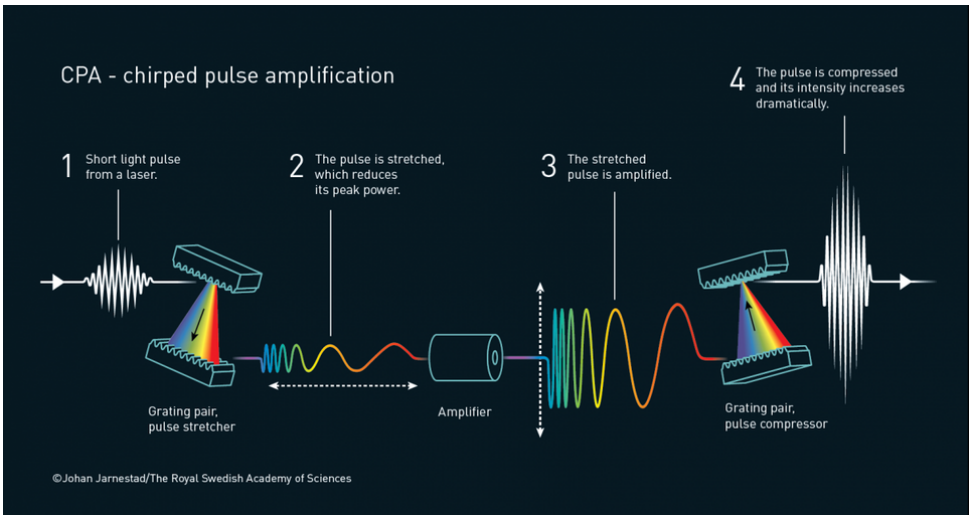

FIGURE 3.1: Schematic figure representing the process of chirped pulse amplification used in regenerative amplifier. Credits to The Royal Swedish Academy of Sciences for the illustration produced as press material for the 2018 Nobel prize in physics announcement.

For the first two experiments presented in chapter 4 and 5, the laser system employed is comprised of a titanium-doped sapphire (Ti:sapph) oscillator and amplifier manufactured by the company Coherent Inc. The mode-locked oscillator provides 50 fs pulses frequency-centred at 810 nm and with an ≈ 80 nm bandwidth. At its 80 MHz repetition rate, 320 milliWatts of its power output are directed to the amplifier to seed the amplification process depicted in Fig. 3.1. The cavity uses a Q-switched Nd:YLF laser with a 527 nm central frequency to amplify the seed inside the gain medium over roughly 15 cavity passes. A tunable grating compresses the NIR pulses, each now containing 5 mJ of energy with a power spectrum peaked at 795 nm and operating at a 1 kHz repetition rate. The amplifier system can be operated to output bandwidth-limited pulses of 40 fs or 110 fs in length. Though the latter pulse duration is more suited for optical rectification in $LiNbO_3$ due to its smaller bandwidth, we opt to use the shorter pulse duration configuration in order to increase the conversion efficiency of the optical parametric amplifier (OPA) used to convert the pump light to 1050 nm.

The OPA used in these experiments is a commercial system provided by the company Continuum. It uses a standard sapphire white-light continuum stage which is mixed collinearly with the input Ti:sapp pump to convert the input spectrum to anywhere between 550 nm and 2.3 μm wavelength. We choose to operate using the signal output at 1050 nm in order to achieve a penetration depth of our pump inside silicon on the same order as our waveguide thickness (150 μm). We note that the ambiguity on the penetration depth here is caused by the extremely

rapid variation of its value in the vicinity of the bandgap of silicon, making it extremely dependent on the precise characteristics of the wafer used. Some of the major drawbacks of having to resort to using an OPA for light conversion were that it needed half of the laser output power to function optimally, providing 10-20 μJ pump pulses and reducing the available energy for THz generation. It also required a fine tuning of the amplifier's compressor settings thus making it impossible to optimally compensate for dispersion in the THz generation and detection line in the absence of an external compressor stage. Furthermore, since the OPA relies on highly nonlinear processes to operate it suffered greatly from short-term pointing instability and long-term intensity drops even when enclosed and positioned nearby the amplifier output. This resulted in an extra source of noise in the pump-induced signal and greatly limited our pulse-shaping capabilities. Furthermore, the wavefront output by the OPA proved to be too distorted to use a spatial light modulator (SLM) to spatially shape the pump intensity. These problems were eventually circumvented by switching to an entirely different laser system, which will now be described.

For the experiments presented in chapters 6 and 7, we used an entirely different laser system provided by our collaborators at the University of Ottawa. The research group of Pr. Jean-Michel Ménard employs a laser system originally developed for industrial applications by the company Light Conversion. The system is a closed-box solid-state amplifier with integrated oscillator which operates at 1028 nm using an ytterbium-doped potassium gadolinium tungstate (Yb:KGW) crystal. Though these family of crystals are typically used for their wavelength tunability, this laser system focuses on providing tunability over its repetition rate, going from 3 kHz all the way to 1 MHz. We opted to use the 6 kHz configuration where pulses carry 1 mJ of energy over their 180 fs duration. The 1030 nm range is still very well phase matched for $LiNbO_3$ and allows us to photoexcite our samples with adequate penetration depths and with up to 200 μJ pump energies. Needless to say, it would be a great understatement to say that this considerably simplified our experiments.

3.2 Terahertz time-domain spectrometer

The routing of the beam used for the later set of experiments is depicted in Fig. 3.2 with the relevant optics labelled. We note that beam is routed using dielectric mirrors optimised for the NIR though they are excluded here for clarity. 20% of the incident p-polarized intensity is first sent to the pump line, depicted in solid blue, where it reflects off a spatial light modulator

(SLM) and imaged onto the sample using a plano-convex lens. We note that a mechanical delay stage, not depicted here, is added to this line for experiments presented in chapters 4 and 7 in order to time-resolve events happening between the arrival of the pump (NIR) and probe (THz) pulses. Furthermore, experiments performed with the 800 nm Ti:sapph amplifier also require the addition of an OPA to this line (not shown here). Also, the SLM is only used in some of the later versions of the experiment and was simply replaced by a mirror in chapters 4 and 5. A beamsplitter positioned before the sample picks off a small part of the light to reproduce the image plane onto a CMOS array camera in order to characterize the pump intensity spatial distribution on the sample. The THz generation line is represented by the pink solid line and comprised of an 1800 lines/mm grating for which the m = -1 diffraction order is imaged onto the $LiNbO_3$ crystal also using a bi-convex lens. We note that the grating is replaced when the experiment is performed using a source frequency-centered at 1028 nm, though in both cases the grating angle and lens position are adjusted to match the Cherenkov cone angle discussed in chapter 2 (63° at 800 nm and 67.5° at 1028 nm). We note that a waveplate is used to rotate the NIR polarization for optimal THz conversion and a set of mirrors and translation stages ensure the most efficient alignment is achieved.

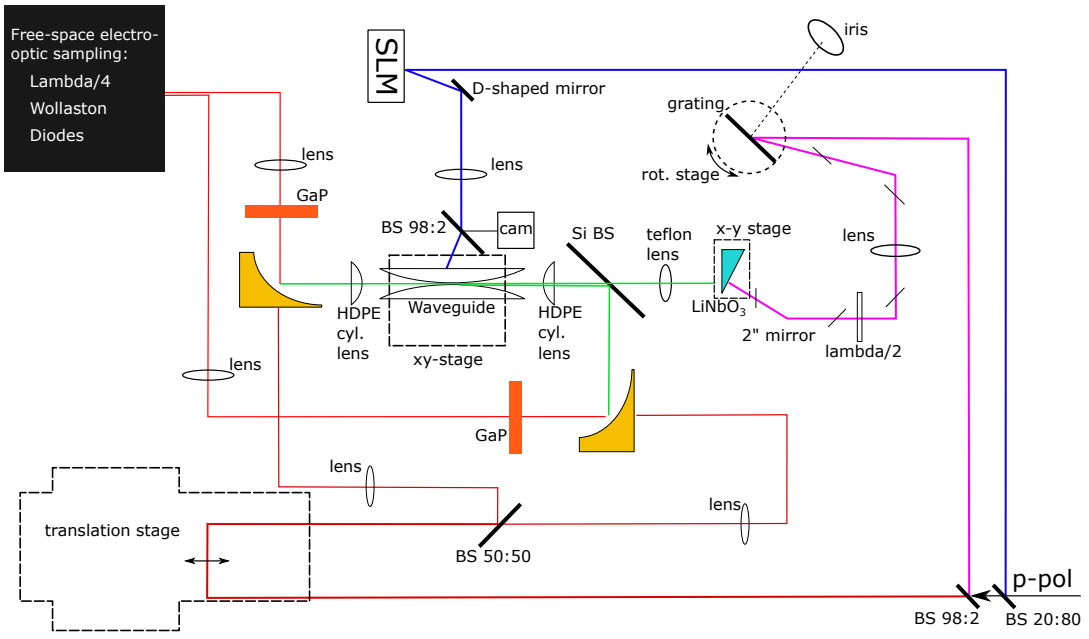

FIGURE 3.2: Schematic representation of the THz spectrometer. The blue line denotes the pump line, the red line the gating line, the pink line shows the THz generation tracing and the green line denotes the THz beampath. The relevant optical elements are identified and the thin black lines crossing the THz generation beam (pink line) denote the orientation of the NIR pulse front tilt.

The THz beam generated by optical rectification is imaged at the output of the $LiNbO_3$ crystal using an uncooled micro bolometer array camera developed by INO Inc. and optimized to achieve collimated THz emission. A plano-convex teflon lens is also used to help collimate the slightly divergent emitted THz beam. The THz pulse is the coupled into and out of the silicon-filled waveguide using a pair of tapered aluminium plates, or horn antennas, alongside custom-made high-density polyethylene (HDPE) cylindrical lenses. The transmitted part is directly collected by a 3" off-axis parabolic mirror, depicted in yellow, and overlapped with the gating beam. The signal reflected from the waveguide is redirected by a 1 cm thick silicon beamsplitter to a 2" off-axis parabolic mirror and overlapped with the gating beam. The detection line is split from the THz generation beam by a 98:2 beamsplitter (2% transmission) and represented in red in Fig. 3.2. A mechanical translation stage allows to change the length of this line thus changing the temporal overlap of the gating beam with respect to the THz beam. A 50:50 beamsplitter splits the gating line to the transmitted and reflected collecting parabolic mirrors where a +300 mm focal length plano-convex lens focuses the NIR beam through a hole in the parabolic mirror in each line. The THz and gating beams are overlapped spatially and temporally inside a thick gallium phosphide (GaP) crystal and then routed to the electro-optic detection components described in the previous chapter. A lock-in amplifier is used in conjuncture with a chopper wheel to subtract the background of the optical signal in the photodiodes. The amplifier and step-stage motor are addressed by a computer via General Purpose Interface Bus (GPIB).

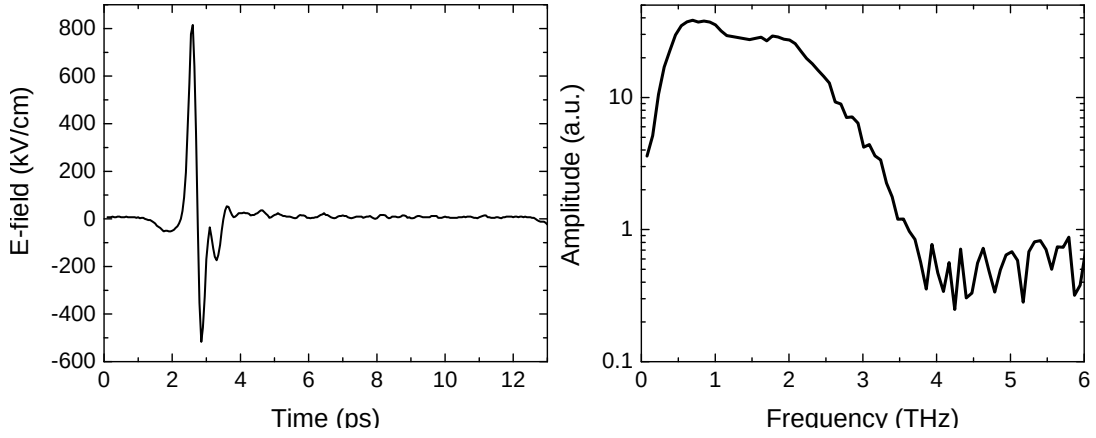

FIGURE 3.3: Time-domain electric field trace (left) generated using tilted pulse-front optical rectification in $LiNbO_3$ in our Ti:sapph amplifier setup. Associated electric field amplitude (right) of the waveform transmitted through air with no waveguide present in the beampath.

A typical electric field time trace is presented in Fig. 3.3 where a single-cycle THz pulse is generated using tilted pulse-front optical rectification in $LiNbO_3$ alongside its amplitude spectrum obtained using a simple fast Fourier transform (FFT). The peak field amplitude

obtained here is of 800 kV/cm, with only air purged of any water vapour present in the path of the THz light. The fundamental limit to the dynamic range achievable by this spectrometer is here limited by the polarization optics, namely Wollaston prism, used for EO detection. The extinction ratio of these polarisers, meaning the ratio in number of photons that leak to the wrong polarization direction, is typically of 1:1000 which sets the peak amplitude to spectral noise ratio achievable, irrespective of the measurement's signal to noise. With some effort, the noise in the measurements was more recently diminished to achieve a sensitivity of $< 1\ \mu V$ on a ~ 10 mV scale, which is majorly governed by the electrical noise. This, helped by the 5 mm thickness of our detection GaP crystal, allows for the detection of electric fields of a few mV/cm, corresponding to ~ 100 photons per pulse.

The frequency resolution achievable in these measurements is limited by the longest possible sampled time trace of our electric field. An important detail is that in order to avoid observing evenly-spaced drops in spectral field amplitude, commonly referred to as etalons, we need to sample only one instance of the pulse in our FFT range. This goes back to the Fabry-Pérot resonator described in the previous chapter but is unwanted in this specific case. Accordingly, every pulse replica created by internal reflections inside the THz generation line, gating line or THz line must be time-windowed in the FFT or data-recording processes. Using a 200 μm thick (110) cut GaP detection crystal glued to a 3 mm thick (100) inactive GaP crystal is one of the ways used to ensure we can achieve the best resolution possible. On top of providing significantly stronger signals, it allows us to sample for a time interval of

$$\Delta t = \frac{2d\mathrm{n}_{GaP}}{c_0} \tag{3.1}$$

where d is the crystal thickness, and $\mathrm{n}_{GaP} = 3.2$ is the refractive index of GaP at NIR and THz frequencies. This provides us with a 107 ps sampling interval, which corresponds to a frequency resolution of 4.7 GHz. This can of course be increased further by zero-padding in the time-domain, i.e. adding zeros to the beginning and end of the data set to increase the frequency resolution, though this is effectively equivalent to mathematically interpolating between the data points and adds no new information to the spectroscopic measurement. Furthermore, the maximum frequency measurable is determined by the time-sampling interval which is limited by our translation stage. The minimum accurate stepping distance of ~ 6 microns corresponds to a Nyquist frequency of 50 THz, well above the investigated bandwidth of ~ 5 THz. Accordingly,

the motor stages are typically moved in larger intervals corresponding to 100 fs time steps in order to minimize data collection times.

3.3 Terahertz and the parallel-plate waveguide

The essence of the experiment is comprised in the waveguide structure presented in Fig. 3.4. Subfigure a) shows broadband THz pulses (green lines) coupled into the waveguide with their electric field perpendicular to the metallic surfaces. The curved aluminium plates help couple THz frequencies from free-space to the silicon-filled section of the waveguide with efficiencies up to 103% higher than hyper-hemispherical lenses [179]. A 30 mm curvature of both top and bottom surfaces at the input and output ports provide good coupling whilst minimizing the footprint of the device. The two aluminium plates are pressed together using 4 screws located around the sample in order to avoid any air gaps between the plates and the sample, which can result in a dramatic increase in propagation loss and dispersion [180]. The top plate is designed with a hole in its center to provide optical access to the enclosed sample. In this configuration, the reflected beam travels back co-linearly with the path of the incident THz pulse and is redirected by a 1 cm thick high-resistivity silicon wafer placed at 45° incidence. Simple Fresnel coefficient calculations for the transmission and reflection ratio of silicon (n_{Si}=3.42) reveal that the beamsplitter reduces the peak electric field amplitude by a factor of 4.4 (19.3 in power) due to the combined transmission and reflection losses. Great progress can thus be made by avoiding the colinear reflection geometry used in those experiments. For this, efforts are being made to out-couple the beam in a non-colinear fashion in future experiments.

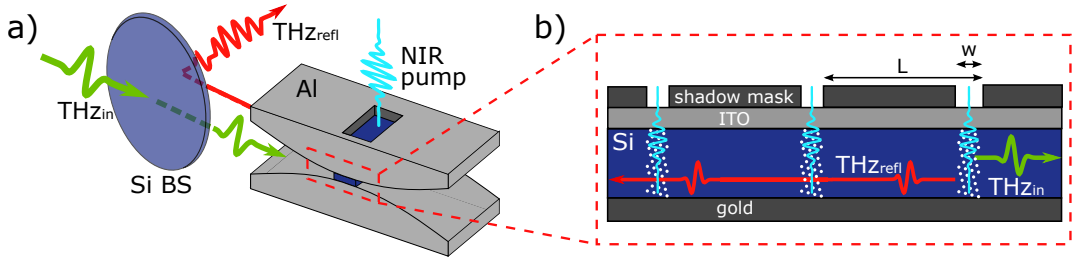

FIGURE 3.4: Schematic depiction of the pumped waveguide device. a) 3-dimensional view of the tapered parallel-plate aluminium waveguide with a silicon sample inside. A silicon beamsplitter reflects (red line) the incident THz pulse (green line). b) Side view of the silicon-filled portion of the waveguide. Gold and ITO coatings provide confinement for the THz wave and optical access through the top for NIR light (light blue). Charge carriers (white dots) are photoinduced in a geometrically-defined fashion using a shadow mask atop the ITO layer.

Subfigure 3.4b) shows an illustrative representation of the waveguide cross-section. Here we can see that an incident THz pulse (green line) has traversed a geometrically-defined photoexcited structure. The photoinduced reflectors depicted by the white dotted regions are created by the promotion of charge carriers by the NIR beam only in the open section of the shadow mask. Each of those acts as a partially reflecting mirror and will create a back-travelling lower-intensity replica of the incident beam (red curves). The optical window used in this waveguide design is 8 mm in length, allowing us to sculpt waveforms up to 182 ps in length.

As mentioned previously, we use high-resistivity ($> 20,000$ Ωm) float-zone silicon to fabricate the samples. The wafers are 2 inches in diameter, commercially available and can be bought at a thickness of 147 ± 7 μm with both sides polished. In order to satisfy the boundary conditions required for propagation of THz light in the TEM mode, we coat both surfaces of the wafer with conductive sheets. For the bottom we sputter a 150 nm sheet of gold with a 3 nm titanium or chromium adhesion layer which effectively behaves like a perfect metal at THz frequencies. The top layer is more challenging as it is also required to provide transparency at NIR frequencies. For this we have elected to use an indium tin oxide (ITO) layer of a few microns in thickness. This industry-standard material can be found on just about any touch-screen device due to its high optical transparency and good conductivity. A company was contracted for its deposition up to a thickness (several microns) sufficient to achieve a sheet resistivity smaller than 1 Ω/sq. We note that in past experiments we have used thin layers ($\sim$ 20 nm) of gold as they provided both good conductivity [181] and NIR transparency comparable to that of thick ITO (10-20%) but they had the major drawback of having next to no resistance to mechanical stress. The addition of a patterned 150 μm thick gold layer is done atop the ITO in order to provide the best contrast possible between the bright and dark areas of photoexcitation. Again, thinner gold layers could provide good contrast but would have poor mechanical resistance. The patterns are defined using standard microfabrication photo-lithography techniques involving UV exposure of photo-active resins, development and subsequent metal deposition and chemical etching.

The ohmic losses resulting from the finite conductivity of the top plate will greatly dominate the overall propagation losses in the waveguide in the absence of pump-induced charge carriers. Let's consider the field absorption coefficient $\alpha = 2n_{Si}/\sigma_1\delta_0 Z_0 d$ [186] where n_{Si} is the refractive index of silicon, δ_0 is the penetration depth of the light inside the material, d is the plate separation and Z_0 is the impedance of free space. Knowing that the sheet resistance of ITO is

given by $R_S = 1/\sigma_1\delta_0$ and assuming a penetration depth of 1 μm in ITO, we find that

$$\alpha_{Si} = \frac{2n_{Si}R_S}{Z_0 d} \simeq 1 \text{ cm}^{-1}. \tag{3.2}$$

This means that for we can propagate the signal through 2.3 cm of sample before we reduce our field strength by a factor 10. In the case of a reflected signal it is good to remember that a pulse will travel the distance twice; from input to reflector and back again. We note that the we also need to account for the 31% combined transmission loss due to the Fresnel reflections at the air-silicon and silicon-air interfaces. Furthermore, the air-filled section of the waveguide is accountable for a portion of the losses. Knowing that aluminium has a conductivity of $3.5 \cdot 10^7$ S/m [192] and yields an 82 nm penetration depth at 1 THz [185] we can calculate the absorption coefficient of both top and bottom plates $\alpha_{Air} = 0.25$ cm^{-1}. This equates to a propagation of roughly 9 cm in air between two plates separated by 150 μm before the field is reduced by a factor of 10.

To ensure good transmission of the THz signal into and out of the silicon-filled portion of the waveguide it is essential that the facets of the wafer used for the experiment be free of any metal and have a smoothness on the order of $\lambda_{THz}/10$. For this, we cleave the samples manually after the ITO and gold coatings, including the shadow mask, are applied to the samples. By carefully selecting a dicing angle parallel to the crystalline axis of the silicon wafers we can achieve exceptionally flat and smooth surfaces, results which were never achieved using diamond saw dicing. We also note that samples for which manual cleaving did not yield sufficiently flat surfaces, likely due to strain in the wafers or clumsy wafer manipulation during the cleaving phase, were polished using extremely fine grit fiber polishing paper to achieve comparable transmission.

3.4 NIR pump of silicon

One of the most important parameters in these experiments is the wavelength of the pump excitation. In order to promote charge carriers with a 1 photon to 1 electron-hole pair ratio we need to provide an excitation energy above the 1.14 eV indirect bandgap of silicon. This means that we have to choose a wavelength shorter than 1088 nm. This is a rather simple task though it gets more complicated when considering the depletion of the incident pump intensity

as it propagates through the thickness of the silicon slab. As mentioned in chapter 2, the Beer-Lambert law states that the intensity of a beam will diminish exponentially with propagation distance as it traverses a material. Knowing that in the case of silicon, the penetration depth is close to 150 μm for light with a 1030 nm wavelength, we can plot the intensity distribution as a function of distance between the waveguide plates. Figure 3.5 shows the intensity along the y-axis, as defined in previous chapters, assuming a 150 μm penetration depth. The black curve illustrates the intensity distribution made by the first pass of the beam through the waveguide thickness. As it reaches the bottom plate, the gold coating reflects NIR light, leaving a new exponentially intensity distribution now decaying with lowering position (red curve). The same phenomenon happens at the return to the ITO top plate where the back-travelling beam (red) is reflected a second time leaving a new exponentially decaying distribution (blue). The sum of all of these contributions is shown here in pink and we have normalised their values to that of the incident pump intensity after transmission through the ITO layer. When accounting for the multiple reflections, we find an average intensity distribution between the plates of $0.94 \cdot I_{incident}$ with a 14% standard deviation. Because the value for the penetration depth varies very rapidly as a function of wavelength near the bandgap, we have calculated those values for a 120 and 180 μm penetration depth which come up to $(0.78 \pm 0.17) \cdot I_{incident}$ and $(1.09 \pm 0.12) \cdot I_{incident}$, respectively. What Fig. 3.5 shows us and what these values corroborate is that after propagation of the pump through the sample it is safe to assume that the intensity distribution is uniform across the plates. This is crucial as we do not wish to cause any scattering between the TEM mode and the higher-order TM modes, which we demonstrated in previous work using pump light with a 15 μm penetration depth [1].

Because some of the experiments presented in this work and projected are performed in a time resolved pump-probe fashion and since some of the effects studied may be sensitive to the timescale on which the optical perturbations occur we need to consider the speed at which the light-induced structures are created. We note that this is irrelevant in the case where the structures are present prior to the arrival of our THz probe pulse, which we refer to as the static case. This timescale is quickly determined as it simply depends on the time it takes for the NIR pulse to traverse from the top to the bottom plate of the waveguide. This is simply given by $\Delta t = dn_{NIR}/c_0$ where d is the plate separation and $n_{NIR} = 3.4$ is the group velocity in silicon at 1030 nm. For a 150 μm thick waveguide we find a 1.7 ps turn-on time. This is substantially slower than the 50-200 fs pulse duration meaning the plate separation is the main limiting factor for the turn-on time. This means that we have to be careful as the dielectric environment is

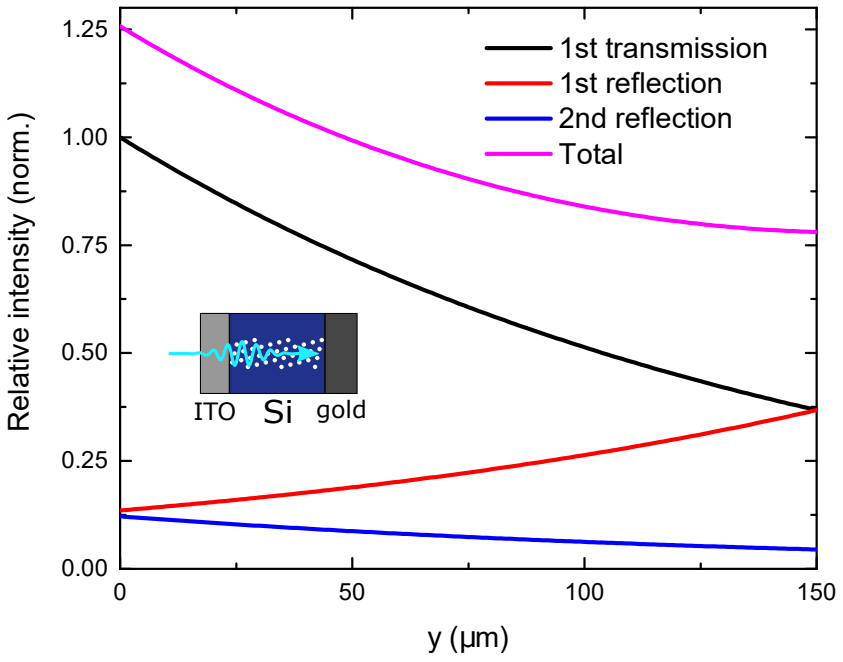

FIGURE 3.5: Relative pump intensity along the waveguide thickness. We show the transmission through the first waveguide thickness (black curve) and subsequent reflections on the gold bottom plate (red curve) and ITO top plate (blue curve). The sum of these is shown in pink, all of which are normalised to the input intensity after the ITO coating. The inset shows the orientation of the waveguide and the incident pump in this representation.

changed on a ∼2 ps timescale, we might experience non-linear effects below 0.25 THz (half a cycle = 2 ps). Of course, if one wished to investigate such non-linear effects in the THz range which can arise when the dielectric environment of a pulse is modified extremely rapidly [82, 182], it would be simplest to use thinner wafers as the turn-on time depends linearly on the plate separation. This 2 ps timescale is also an indication that effects happening on shorter timescales may be smeared out and unresolved in pump-probe time-domain spectroscopic measurements. We also note that to some extent the charge carrier uniformity criteria is met once the pulse has made its second pass through the waveguide thickness after reflection upon the gold backplate, bringing the turn-on time closer to 3.4 ps.

Another important parameter in those experiments is the recombination time of the charge carriers. As electrons and holes are created through photoinjection these pairs of oppositely-charged particle and quasi-particle will recombine thus giving our device reversibility and reconfigurability. The timescale over which these carriers recombine is entirely independent on the pump characteristics other than its intensity. For silicon at room temperature, charge carriers recombination times are on the order of 100 μs, which should allow for reconfigurability up to a 10 kHz rate, well above the repetition rate of the lasers used. The experiments are operated below

any scattering saturation threshold ($\sim 10^{16}$ carriers/cm^{-3}) and we do not expect there to be any significant increase in sample temperature caused by the pump. We note that in order to decrease the reconfiguration time, thus increasing the reconfigurability rate, it would be possible to sweep the carriers using a static potential across the plates. Alternatively, one could use a direct bandgap semiconductor, such as GaAs, which typically yields carrier recombination times on the order of microseconds. This raises the issue of having to achieve penetration depths on the order of 100 μm in materials that generally yield only a few microns of penetration depth.

One more important parameter in our experiments is the intensity distribution of the pump across the waveguide surface. As depicted in Fig. 3.2, we employ a CMOS array camera to perform this task. The sample is initially removed and the camera is placed with the detector array in its position. A reference image is then created using the SLM or by simply focusing a short focal length lens with the camera at the focus. The camera is then put back to its usual position behind a beamsplitter where it is adjusted to ensure that its detector array is at the same image plane as the sample. When the sample is put back into position we have an accurate measurement of the intensity distribution across its surface. We note that the camera's dynamic range is somewhat limited and its intensity has to be adjusted using either internal gain, exposure time or through external neutral density filters. Accordingly, we need to resort to a separate intensity monitor that is introduced in the line to record the integrated incident pump power. We can then correlate the two measurements to extract the intensity distribution, or fluence, over the sample. The camera provides a 5.3 μm pitch which defines our spatial resolution, though this corresponds to the wavelength of a 16.5 THz signal, largely above our experimental bandwidth.

3.5 Differential pump-probe measurements

We would like to bring some clarity here on a measurement technique, referred to as differential measurement, used in this work. As mentioned previously, all of the measurements are recorded using a lock-in amplifier through EO sampling. The strength of the lock-in amplifier is that it can be triggered by the signal of a chopper wheel which is modulating the signal at a frequency commensurate with that of the laser repetition rate. This way, one can subtract the background signal, or illumination, on the detection photodiodes and minimize the optical, and even electrical noise of the measurement. When trying to detect a minute modulation of the signal, the differential measurement is better suited as it allows the subtraction of the signal

itself. In our experiment, this translates as moving the chopper wheel to the pump line thus measuring $\Delta E(t) = E_{ref}(t) - E_{pump}(t)$. Here, E_{ref} is the reference signal, without pump, and E_{pump} is the signal in the presence of a pump. Again, when the modulation is small and those two quantities are similar, this method allows one to measure their difference on a much smaller scale, or higher sensitivity, thus greatly improving the signal-to-noise ratio and improving the experimental sensitivity. In order to retrieve the correct amplitude though, one must ensure proper chopper wheel phase as well as lock-in phase calibrations. A post-processing step is also generally needed in order to correct the amplitude of the signal in frequency space. By properly gathering a reference (unpumped) waveform (E_{ref}), modulated (pumped) waveform (E_{pump}), as well as a differential waveform ($\Delta E(t)$) separately we can adjust the amplitude by a multiplicative calibration factor a given by the equation

$$\frac{E_{pump}(\omega)}{E_{ref}(\omega)} = 1 - a\frac{\Delta E(\omega)}{E_{ref}(\omega)}. \tag{3.3}$$

Furthermore, this calibration should be performed before and after each differential measurement in order to retrieve correct phase information and to avoid time-drift errors.

We should also note that though this technique is great for accessing pump-induced transients with greater resolution, it also has its drawbacks. For example, when we use the pump-induced reflectors to generate a back-travelling sculpted waveform, as in chapter 5, the reflected field amplitudes are on the order of that from Fresnel reflections at the air-silicon sample interface. Because these surfaces are all parallel to one-another they will all back-travel colinearly and thus be detected by a regular EO detection scheme. Since the air-Si interface appears before in the beampath, the reflected pulse it creates will arrive in our detector earlier than the pump-induced pulses. If we consider the same case but in for a differential measurement; the air-Si reflection is present in both pumped and unpumped scenarios and will thus be subtracted by the lock-in amplifier whereas the pump-induced reflections still remain. There are of course other optics in the THz beampath that cause reflections to be picked up by the detector and those can be substantially greater than our pump-induced reflections. One can imagine that in a scenario where samples are probed with pump-induced waveforms the experiment would become sensitive to THz-pump THz-probe effects and this technique could breakdown, especially in the presence of nonlinear effects. For this, efforts are being made in developing a pulse-shaping scheme that prevents the overlap of the pump-induced waveform and stray reflections.

Chapter 4

Dynamic creation of a light-induced terahertz guided-wave resonator

4.1 Preface

In this chapter we present the first pulse shaping demonstration we made using patterned photoinjection inside a waveguide. This work focuses on the dynamic creation of a periodic array of photo-injected lines that result in transmission enhancement on resonance. We note that all the measurements presented were performed in transmission configuration and that simulations were used to infer information on the reflected signal. The main reason for the lack of reflection measurements is that we had not yet realized that the reflection geometry would be such a powerful tool for THz pulse shaping. The data is recorded with time resolution between the pump and probe beam arrival in order to investigate the dynamics of spatially-defined charge carrier photoinjection on a picosecond timescale. The 1-dimensional photonic structure created did not yield a gap but the bending of the photonic bands showed that this could be used for slow light experiments. Accordingly, we characterized the group velocity change introduced by the structure and validated that our experimental conditions were well described by the Drude model. Furthermore, simulations were performed using finite-difference time-domain (FDTD) simulations in order to fit the transmission measurements and extract the reflection characteristics from those same simulations. Analytical transfer-matrix method calculations were also performed in order to fit the experimental results though these are not presented in this work as they essentially reproduced almost exactly the results acquired through the

FDTD method. We also note that some simulations were performed employing finite element method (FEM) simulations using the commercially available software COMSOL® though the absence of time-dependent pump characteristics greatly limited their usefulness. One of the truly remarkable things about this experiment, though no clear signature presents itself in the experimental data, is the fact that the dispersion relation of the THz light traversing the sample is modified directly from the light line. Whereas most photonic experiments rely on a pre-existing periodically repeating structure with its own dispersion characteristics, bands and gaps; we create a new band structure out of "nothing".

This work was published in 2014 the journal *Optics Express* and titled "Optically induced mode coupling and interference in a terahertz parallel plate waveguide". The authors, listed in order, are Lauren Gingras, Marcel Georgin and David G. Cooke. The experimental work was almost entirely done by Lauren Gingras alongside the FDTD and transfer-matrix simulations. Marcel Georgin, in charge of an undergraduate research project, contributed FEM simulations that were extremely useful to the understanding of the underlying physics presented in this work. Though his simulation results were not presented in the manuscript his name belonged in the list of authors. David G. Cooke was attributed the last author slot for his supervisory work, which means he basically oversaw every step of the process from conception of the experiment to overhauling of the article's manuscript.

We would also like to note that, as required by McGill University's thesis manuscript guidelines, this chapter is identical to the published version of the paper, including the list of references which are numbered and listed independently within the chapter. This will also be the case for the following two published articles (chapters 5 and 6).

4.2 Abstract

We demonstrate a dynamic light-induced resonator for terahertz (THz) frequency light created on ultrashort time scales inside a planar waveguide. The resonator is created by patterned femtosecond photoexcitation of a one-dimensional array of photoconductive regions inside a silicon-filled parallel plate waveguide. The metal-dielectric photonic crystal is created on a 2 ps time scale, ten times faster than the 20 ps transit time of the THz light through the array. The resonance reveals itself through narrowband THz transmission enhancement with accompanying phase modulation producing an induced group delay of up to 10.8 ps near resonance.

4.3 Introduction

The development of new methods to confine and control light in the terahertz (THz) region (0.1-10 THz) of the spectrum is a major area of current photonic research [1, 2]. The expansion of the wireless communication spectrum, for example, promises multi-Gbit data transfer rates as the carrier wave is pushed into the THz band [3–6]. Integration of several technologies into a functional system typically requires confinement and isolation of light via guided modes, as opposed to free space optics that are susceptible to environmental conditions and requires a large footprint. For THz light, a parallel plate waveguide (PPWG) operating in the TEM mode provides a low loss platform for the integration of photonic components [7], with several passive [8–11] and active [12–15] devices having recently been demonstrated. Periodicity of dielectric and metallic structures embedded within the waveguide modifies the photonic bandstructure, modulating the amplitude and phase of transmitted light. Another interesting degree of freedom in such structures is the possibility of breaking time-reversal symmetry through dynamic modulation of the local dielectric function via photoinjection of free charges [2, 16]. In the optical regime, interesting effects such as all-optical stopping [17] and storage of light [18], a photonic Aharonov-Bohm effect [19], an effective magnetic field for photons [20], and a photonic Haas-van Alphen effect [21] have been demonstrated using dynamically modulated photonic structures and resonators. Nonlinear optical effects such as the frequency shifting of light are also possible, where the dynamic modulation induces an effective $\chi^{(3)}$ interaction [22, 23].

At THz frequencies, wavelengths are large (1 THz = 300 μm) and so spatial modulations of sub-wavelength dimension can be easily achieved through illumination by an optical pulse, down to the diffraction limit. Using femtosecond pulses to modulate the dielectric function, one can photoexcite on a sub-cycle time scale as well. This new possibility allows one to dynamically modulate the photonic band structure in the extreme non-adiabatic limit by sudden introduction of spatial periodicity on a sub-wavelength scale. Furthermore, the possibility of an optically generated metal-dielectric structure through spatial patterning eliminates the need for fabrication of permanent photonic structures, making the device fully-reconfigurable and reversible in nature. Here we demonstrate the dynamic creation of a THz metal-dielectric photonic crystal inside a PPWG on a time scale much shorter than the pulse transit time. The sudden creation of a resonant structure faster than the THz pulse transit time permits the capture of energy within the resonator volume, delaying the arrival of THz light by an amount determined by the group delay. The more closed a cavity, the longer it can store energy

however the more difficult it is to couple in light. By switching on the entire structure faster than the transit time, we transiently increase the coupling into the structure compared to a static resonator, as verified by experiments and finite-difference time domain (FDTD) simulations. It is important to note here that no pre-existing structure is present inside the waveguide as is often the case in dynamic photonic experiments [2, 23, 24]. We show the onset of enhanced transmission peaks relative to the background absorption as evidence for the dynamically created resonance and selective temporal delay of THz photons up to 10.8 ps.

4.4 Experimental

The time-domain THz spectrometer used in this work is based on optical rectification in a $LiNbO_3$ prism of 800 nm, 40 fs pulses from a Ti:sapphire fs laser amplifier [25–28] using the tilted-pulse front method and electro-optic sampling in an undoped (110) cut GaP crystal of 200 μm thickness optically bonded to a 4 mm inactive GaP (100) cut substrate to avoid reflections that can limit the spectral resolution. The THz pulses are collimated exiting the LN prism and teflon lenses with focal length of 100 mm ensure THz coupling in and out of a tapered aluminium PPWG, schematically drawn in Fig. 4.1(a). Coupling into the transverse electromagnetic (TEM) mode of the waveguide provides minimal waveguide losses and dispersionless propagation in the enclosed 147 μm-thick high-resistivity silicon wafer ($\rho > 20,000$ Ω-cm). The Si-filled region of the PPWG is back-coated with a 200 nm-thick layer of gold and top-coated with several μm-thick indium tin oxide, a transparent conductor. Both coatings provide $< 1\Omega$/sq sheet resistance to confine the THz pulse while the transparency of ITO is sufficient to allow for optical pumping as depicted in Fig. 4.1(b). The THz peak electric field is lowered using a wire-grid polariser pair preventing inter-valley scattering of the photoinjected carriers inside the waveguide. The pump pulses are centered at 1050 nm, produced by an optical parametric amplifier. The wavelength was chosen to be above the silicon indirect bandgap to homogeneously inject charge carriers through the thickness of the waveguide with penetration depth > 100 μm. A 100 nm-thick gold shadow mask lithographically deposited atop the ITO layer allows spatial definition of the $d_1 = 10$ μm wide photoconductive regions with sub-THz-wavelength precision. The travel time of the NIR pulse across the Si waveguide restricts the creation time of the resonator to 1.7 ps, comparable to the travel time of the THz pulse between two adjacent photoexcited regions. Furthermore, the creation time is an order of magnitude smaller than the transit time of the pulse through the entire structure (20.5 ps). Thus, a

resonator structure can be dynamically and all-optically created inside a silicon waveguide at a moment where it entirely encompasses a THz pulse, as depicted in Fig. 4.1b). The turn-off time of the resonator is ultimately limited by the recombination time of the charge carriers; ~ 100 μs in silicon. However, charge diffusion will contribute appreciably to the cavity deterioration once charges have diffused over a distance comparable to the smallest length scale of the photonic crystal. Assuming a critical diffusion distance equal to 10% of the photoexcited wall thickness ($d_1 = 10$ μm) the diffusion time is given by $t_d = (0.1d_1)^2/D \simeq 4.3$ ns. Here, the diffusion coefficient is given by $D = \mu_{eh} k_B T/e = 2.33$ cm^2/s where k_B is the Boltzmann constant, T is the temperature in Kelvins, e is the elementary charge and given the ambipolar mobility of electrons and holes in silicon $\mu_{eh} \simeq 90$ cm^2/Vs [29, 30].

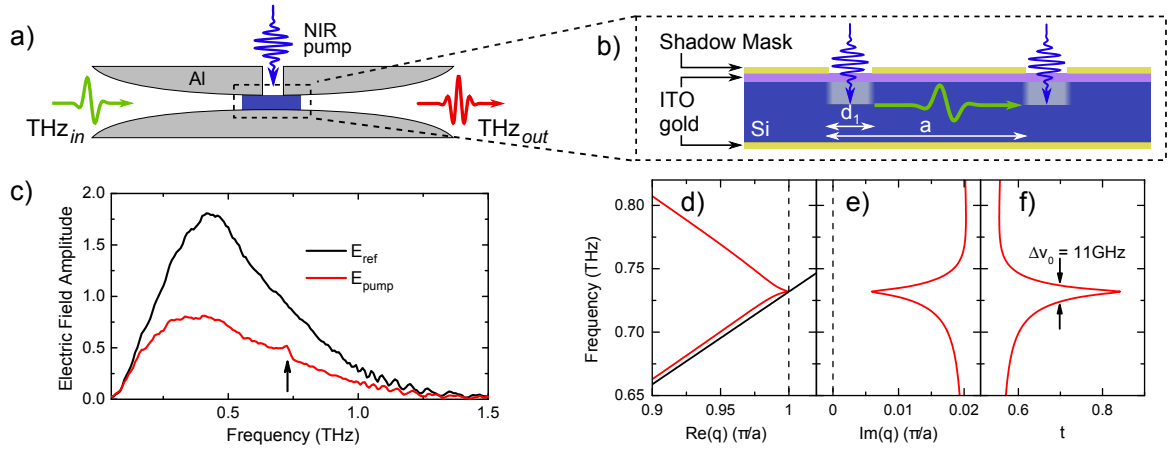

FIGURE 4.1: (a) Schematic of the experimental setup showing the THz pulse coupled into the Si-filled waveguide via a tapered aluminium PPWG. A window allows pumping of the silicon-filled region using a near infrared (NIR) pump pulse. (b) Schematic representation of the periodic metal-dielectric array (gray rectangles) being photoinjected on a sub-transit timescale. (c) Electric field amplitude (arbitrary units) transmitted through the unexcited (E_{ref}) and photoexcited sample (E_{pump}), well after the pump pulse arrives. The a = 60 μm lattice periodicity of the structure introduces a resonance at 0.728 THz, indicated by the arrow. (d) Photonic band structure of the created cavity (red) and of the unpumped waveguide (black) in the vicinity of the first resonance for the Bragg wavevector q. (e) Corresponding imaginary part of the wavevector and (f) electric field transmission t $(\omega) = |E_{pump}(\omega)|/|E_{ref}(\omega)|$.

The signature of a metal-dielectric photonic crystal is a resonant transmission enhancement, relative to the background absorption, when an integer multiple of half-wavelengths inside the media is approximately equal to the periodicity of the stack, with small corrections due to the finite thickness of the metal film [31]. This occurs at a frequency $f_m = mc_0/(2n_{Si}a)$, where $n_{Si} = 3.418$ is the refractive index of Si at THz frequencies, a is the structure periodicity and m is an integer. Figure 4.1(c) shows the THz transmission spectrum through both an unexcited silicon slab, with the THz pulse arriving well before the pump (E_{ref}), and the spectrum when the THz pulse arrives well after the pump, in the quasi-steady state (E_{pump}). The 60 μm periodic

metallo-dielectric structure exhibits a marked transmission enhancement at a frequency of 0.73 THz, in excellent agreement with first order ($m = 1$) Fabry-Pérot resonator physics, as well as a broadband attenuation due to Drude absorption. We also note that the onset of oscillations in both data sets at frequencies greater than 1 THz is due to multi-modal interference due to partial coupling into the TM_2 geometric mode, caused by slight misalignment into the tapered PPWG [15, 32].

The band diagram of the structure created is calculated using the one-dimensional metal-dielectric stack dispersion relation:[33]

$$\cos(qa) = \cos(k_1 d_1)\cos(k_2 d_2) - \frac{1}{2}\left(\frac{k_1}{k_2} + \frac{k_2}{k_1}\right)\sin(k_1 d_1)\sin(k_2 d_2)\,. \tag{4.1}$$

Here, q represents the complex-valued Bloch wavevector, d_1 and d_2 the thickness of the pumped and unpumped regions, respectively and $a = d_1 + d_2$ is the periodicity of the stack. The modulation is introduced in the model via the complex wavevector of the photoexcited region $k_1 = \frac{\omega}{c}\sqrt{n_{\mathrm{Si}}^2 + i\sigma(\omega)/\epsilon_0\omega}$ and using n_{Si} to define the real-valued k-vector of the unpumped region $k_2 = n_{\mathrm{Si}}\omega/c$. A scattering time $\tau_D = 50$ fs and an effective mass $m^* = 0.26m_e$ are used to define the complex conductivity of the photoexcited region through the Drude model $\sigma(\omega) = \frac{ne^2\tau_D/m^*}{1-i\omega\tau_D}$, for the photoexcited carrier density $n \simeq 10^{18}\mathrm{cm}^{-3}$. The calculated band structure in the presence (red) and absence (black) of photoexcitation is presented in Fig. 4.1(d) in the vicinity of the $m = 1$ resonance. Without photoexcitation, propagation occurs on the light line representing the dispersionless propagation of the TEM mode in the waveguide. Upon photoexcitation, Bragg scattering occurs at the lattice wavevector π/a, with a zero-energy gap and a reversal of group velocity above and below resonance. On resonance, the imaginary part of the wavevector, governing loss, shows a marked reduction, shown in Fig. 4.1(e), interpreted as a resonant tunnelling phenomenon. Transmission spectra can be calculated easily by neglecting reflections at the beginning and end of the structure, which is a good approximation due to the soft Gaussian onset of photoconductivity, and assuming Beer's Law for the electric field transmission coefficient $t = e^{-Im(q)L}$. A L=1.8 mm thick effective medium equivalent to the 12-pair, 60 μm periodic, metal-dielectric structure is created here. On resonance a transmission peak appears upon photoexcitation with a linewidth of 11 GHz, shown in Fig. 4.1(f). This represents the fundamental limit to the linewidth, governed by the conductivity of the metallic constituents in the absence of disorder, with an upper Q-factor for the resonator of $\nu_0/\Delta\nu = 66$.

4.5 Results and discussion

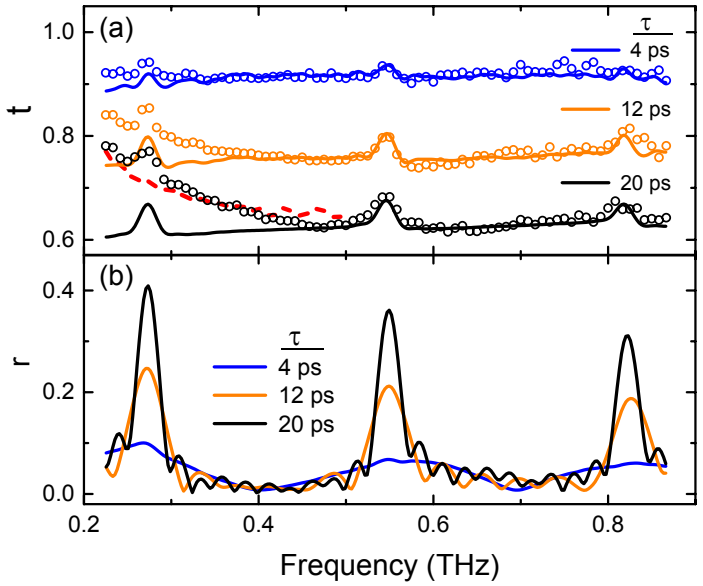

FIGURE 4.2: (a) Experimental data (open circles) and FDTD simulation results (solid lines) of the field transmission amplitude $t(\omega,\tau) = |E_{pump}(\omega,\tau)|/|E_{ref}(\omega)|$ for various pump-probe time delays (τ) for a 12 metal-dielectric pairs. (b) Corresponding simulated reflection amplitude $r(\omega,\tau) = |E_{refl}(\omega,\tau)|/|E_{inc}(\omega)|$. The dashed red curve presented in (a) shows the transmission for a homogeneous photoexcitation, plotted below 0.5 THz for clarity. Lattice periodicity is set to 160 μm and pump energy kept constant at 5.6 μJ over the 1.8 mm structure length.

Several transmission peaks can be arranged within the bandwidth of the THz pulse simply by increasing the periodicity. Transmission spectra for various pump-probe time-delays (τ) are presented in Fig. 4.2(a) (open circles) for 12 photoexcited lines of 20 μm width separated by 140 μm unpumped Si. The $m = 1$, 2 and 3 resonances are evident. The zero time $\tau = 0$ is

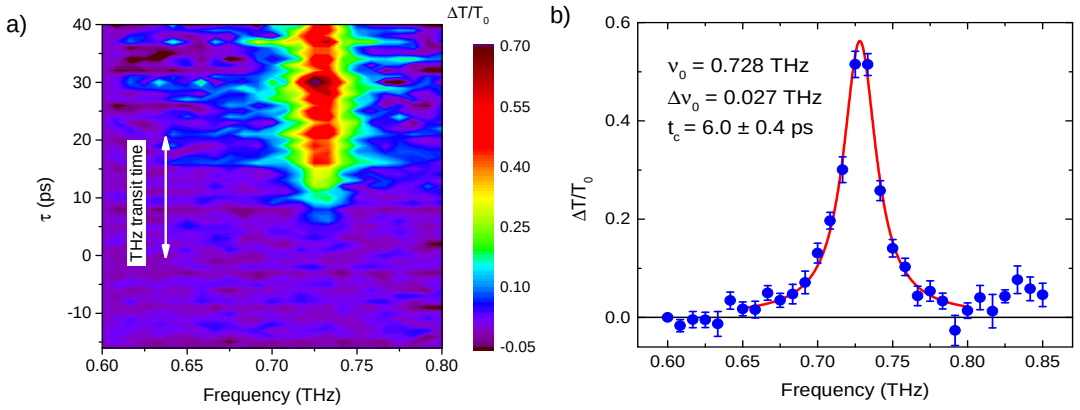

FIGURE 4.3: (a) Intensity modulation ($\Delta T/T_0$) as a function of frequency and pump-probe time delay (τ). (b) Lorentzian fit of the intensity modulation in the static regime ($\tau > 27$ ps). The pump energy is kept constant at 5.6 μJ with a 60 μm periodic structure.

defined as the delay where the THz pulse just exits the photoexcited region when the pump pulse arrives, identified by the earliest change in THz transmission. Negative pump-probe time delays are defined as a late arrival of the NIR pump, and the THz pulse transit time through the total structure is approximately 21 ps. FDTD simulations taking into account the dispersion of the Drude conducting regions are carried out for a simplified one-dimensional system using a freely available code written by Larsen *et al.* [34], with the results showing excellent agreement with the data in Fig. 4.2 (solid lines). The experimentally observed low-frequency roll off is attributed to the portion of the electric field existing outside the waveguide, in the window region, due to finite plate conductivity [35, 36]. Accordingly, the same behaviour is also present for a uniform non-periodic photoexcitation of the waveguide as shown by the dashed red curve in Fig. 4.2(a). Pump energy is used as the sole floating parameter and fixed to the value which best fits the static ($\tau > 27$ ps) photoexcitation transmission. FDTD simulations further reveal sharply peaked features in the reflected electric field amplitude on resonance. This behaviour appears counter-intuitive when considering a lossless dielectric resonator where minima in reflection are usually accompanied by transmission maxima. The observed reflection and transmission maxima occurs here due to the lossy nature of the metallic constituents of the 1D array. Further investigation reveals that when the imaginary part of the complex refractive index (κ) of the photoexcited silicon regions reaches the same order of magnitude as the real part (n), the device will begin to exhibit simultaneously enhanced transmission and reflection on resonance. For a Drude metal, this occurs for frequencies $f \leq 1/(2\pi\tau_D)$ or ≤ 3 THz for silicon, which encompasses the entire THz pulse bandwidth. At late pump-probe time delays the resonator acts as a broadband absorber for off-resonant frequencies. Static regime results are also well-reproduced by analytical transfer-matrix method calculations in both reflection and transmission (not shown here). The broadband absorption and reflection peak is highest for $\tau = 20$ ps, when the THz pulse is traversing the entire photoexcited structure. A noticeable narrowing of the reflection peak is shown in Fig. 4.2(b) as one moves from a situation where the photonic structure is created while the THz pulse is inside, to a pre-existing structure that it transmits through in its entirety. Broadening of the reflected peaks is attributed to the decreasing number of reflective interfaces on which the THz pulse is incident at earlier τ, reducing the number of reflected THz electric field cycles thus broadening the reflection peaks.

Two dimensional pump-probe spectroscopy performed on the $a = 60$ μm sample provides insight on the dynamic effect of sub-transit-time resonator creation. The intensity modulation

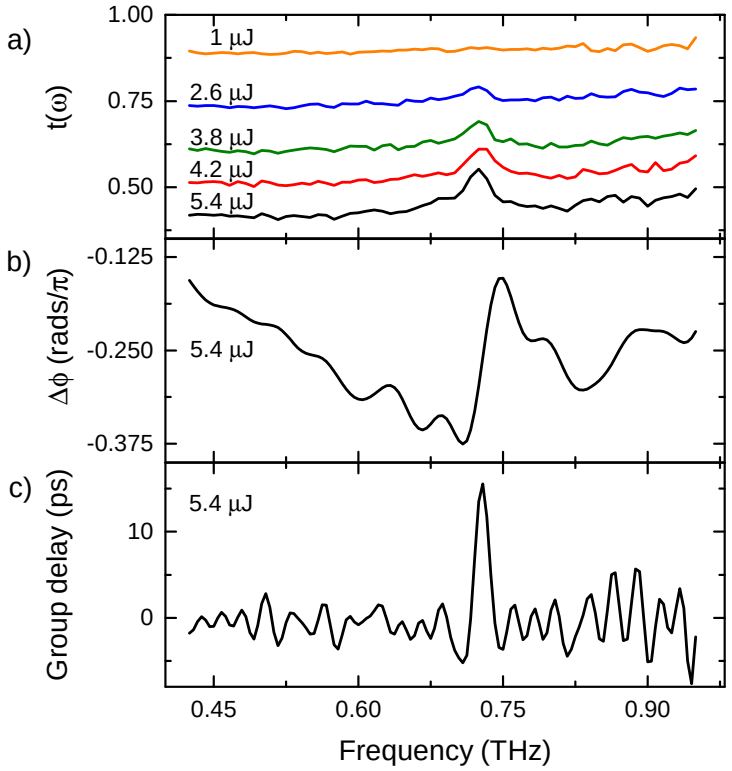

FIGURE 4.4: (a) Measured electric field transmission $\mathrm{t}(\omega)$, (b) measured phase change $\Delta\phi(\omega) = \phi_{pump}(\omega)/\phi_{ref}(\omega)$ and (c) extracted group delay for a 60 μm periodic sample for various pump energies. The data is recorded in the static regime ($\tau > 30$ ps).

($\Delta \mathrm{T}/\mathrm{T}_0 = (t^2 - t_0^2)/t_0^2$) of the 1st order peak taken with respect to the off-resonant THz transmission baseline (T_0) is presented in Fig. 4.3(a). For a constant pump energy of 5.6 μJ, a single crest arises, steadily peaked at 0.73 THz. Shoulder-like features at frequencies adjacent to the resonance are attributed to inhomogeneities in pump intensity distribution as they are present even in the static regime; excluding the possibility of dynamic sideband generation. The absence of additional features in the spectrum further confirms that the 1.7 ps creation time of the resonator is insufficient to induce any observable nonlinearities at these frequencies. Fitting of the time-averaged static excitation portion ($\tau > 27$ ps) to a Lorentzian lineshape, shown in Fig. 4.3(b) indicates a 27 GHz linewidth ($\Delta\nu_0$) frequency-centered at 0.728 THz. The modulation is peaked at 56% and exhibits a lifetime (t_c) of 6.0 $\pm$ 0.4 ps at large τ and a Q-factor of 27. Presented in Fig. 4.4 is the electric field transmission, phase change and group delay induced by the resonator for varying pump energies. Electro-optic sampling provides direct access to both amplitude and phase of the transmitted electric field allowing us to extract the group index $n_g(\omega) = n_\phi(\omega) + \omega\dfrac{\partial n_\phi(\omega)}{\partial\omega}$. The phase change induced by the structure can be observed in Fig. 4.4(b). The phase index is given by $n_\phi(\omega) = n_{Si} + \dfrac{c_0\Delta\phi(\omega)}{\omega L}$ where $\Delta\phi(\omega) = \phi_{pump}(\omega) - \phi_{ref}(\omega)$ and d is the length of the resonator. We can thus calculate an

effective group delay assuming an effective media of length L with a refractive index n_g and knowing that the group velocity is given by $v_g(\omega) = c_0/n_g(\omega)$. An average over all $\tau > 27$ ps of the group delay induced for a 1.8 mm wide structure made of 30 periodically repeating 60 μm index modulations induced using 5.4 μJ pump energy reveals a maximum of 10.8 $\pm$ 0.7 ps group delay on resonance. The results of a single pump-probe delay are shown in Fig. 4.4(c).

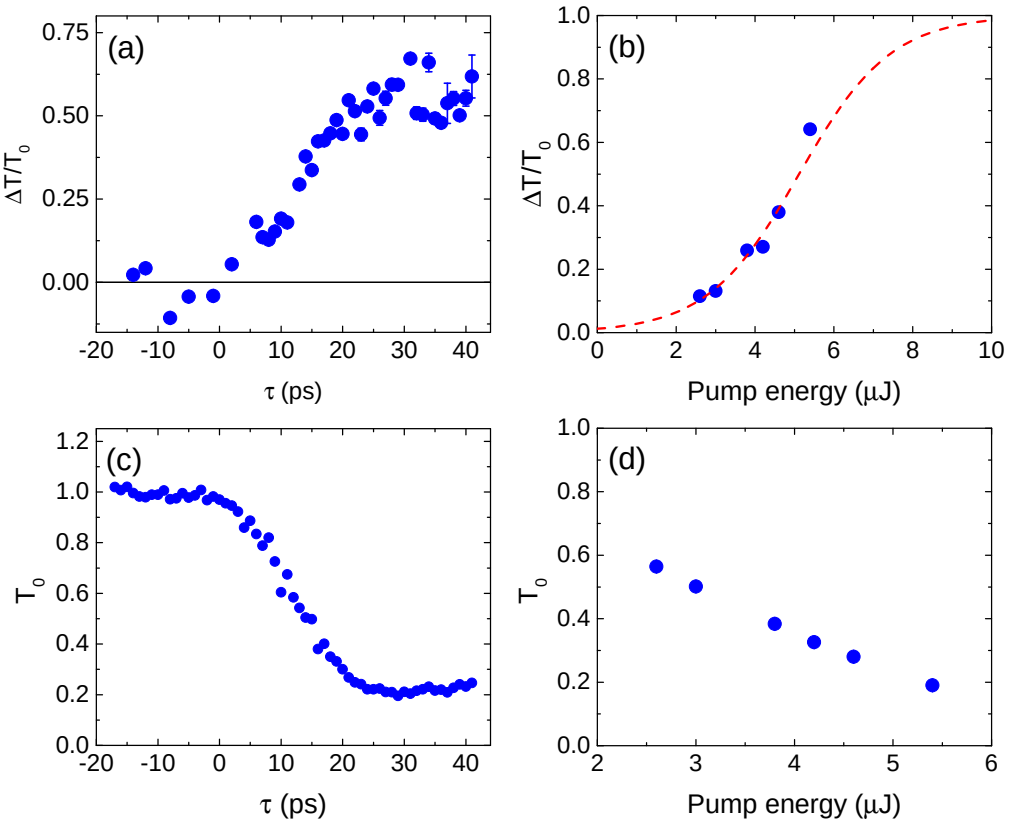

FIGURE 4.5: Intensity modulation as a function of (a) pump-probe time delay (τ) and (b) pump energy with a sigmoidal fit curve shown as a red dashed line. Intensity baseline as a function of (c) pump-probe time delay (τ) and (d) pump energy. The data is presented for the 60 μm periodic sample with a baseline defined at 0.6 THz. (a) and (c) are measured at 5.6 μJ pump energy; (b) and (d) are measured in the static case ($\tau > 30$ ps).

Lorentzian fit parameters extracted from single pump-probe time delay steps indicate no evolution in the transmitted resonance linewidth, or lifetime, within error margins, once the resonance becomes appreciable ($\tau > 5$ ps). Peak intensity modulation amplitude increases with time delay over the 20.5 ps transit time (Fig. 4.5(a)) due to the increased number of photoinjected interfaces in the THz path. Accordingly, the intensity transmission baseline, presented in Fig. 4.5(c), decreases over the same timescale to a minimum of 20 %. The performance of this device is in this case limited by the available pump energy, by the substantial reflection losses undergone by the NIR pump at the shadow mask and by the low transparency of the thick ITO layer.

Adjustment of the pump power provides additional tunability over the intensity modulation and baseline transmission of this optically-induced resonator. Peak modulation intensity data presented in Fig. 4.5(b) demonstrates a superlinear increase of the peak intensity modulation ratio, $\Delta T/T_0$, with pump energy. A sigmoidal fit to the data is shown as a red dashed line, describing the data reasonably well while respecting the upper and lower bounds of 1 and 0, respectively. This fit indicates that the modulation would saturate above 90% at a pump energy of 8 μJ and has a 10% threshold of 2.5 μJ. The associated intensity transmission baseline, shown in Fig. 4.5(d), indicates a linear decrease with increasing pump energy. This result is well described by the linear increase of the conductivity with pump fluence predicted by the Drude model. No appreciable change in center frequency or peak linewidth is observed with varied pump intensities, again differentiating this device, where the metallic regions are thinner than the THz skin depth, from a lossless dielectric photonic crystal for which the lifetime is characterized by the interface reflectance.

4.6 Conclusion

In conclusion, we have demonstrated an all-optically injected and dynamically created resonator inside a PPWG at THz frequencies in a homogeneous semiconductor slab. The turn-on time of the cavity, 1.7 ps in this case, is largely limited by the transit time of the NIR pulse through the thickness of the waveguide which can be reduced by using a thinner wafer. Dynamic creation of resonator structures encompassing a THz pulse on timescales faster than the transit time (20.5 ps) demonstrates potential for introducing frequencies otherwise not allowed inside a structure. The 60 μm periodicity sample exhibits a resonant lifetime of 6.0 $\pm$ 0.4 ps at 0.728 THz corresponding to just above 8 electric field cycles. The measured Q-factor of 27 can ultimately be improved by a factor 2.45 according to analytical predictions by increasing the array size and general homogeneity of the pump excitation and by reducing the waveguide plate losses, dominated here by the ITO. Phase analysis additionally reveals a group delay of 10.8 ps in the static regime. These resonant effects can be tuned to any arbitrary frequency via the structure periodicity, and incorporation of a spatial light modulator should enable video rate switching between structures.

4.7 Funding information

The authors gratefully acknowledge funding from FRQNT and NSERC.

References

[1] Miriam Serena Vitiello et al. “Photonic quasi-crystal terahertz lasers”. In: *Nat. Commun.* 5 (2014), p. 5884.

[2] R. Kakimi, M. Fujita, M. Nagai, M. Ashida, and T. Nagatsuma. “Capture of a terahertz wave in a photonic-crystal slab”. In: *Nat Photonics* 8 (2014), pp. 657–663.

[3] M. Tonouchi. “Cutting-edge terahertz technology”. In: *Nat Photonics* 1 (2007), pp. 97–105.

[4] T. Nagatsuma et al. “Terahertz wireless communications based on photonics technologies”. In: *Opt. Express* 21 (2013), pp. 23736–23747.

[5] T. Nagatsuma. “Breakthroughs in photonics 2013: THz communications based on photonics”. In: *IEEE Photonics J.* 6 (2014), pp. 1–5.

[6] S. Koenig et al. “Wireless sub-THz communication system with high data rate”. In: *Nat Photonics* 7 (2013), pp. 977–981.

[7] R. Mendis, V. Astley, J. B. Liu, and D. M. Mittleman. “Terahertz microfluidic sensor based on a parallel-plate waveguide resonant cavity”. In: *Appl. Phys. Lett.* 95 (2009), p. 171113.

[8] Z. P. Jian, J. Pearce, and D. M. Mittleman. “Two-dimensional photonic crystal slabs in parallel-plate metal waveguides studied with terahertz time-domain spectroscopy”. In: *Semicond. Sci. Tech.* 20 (2005), S300–S306.

[9] Adam Bingham, Yuguang Zhao, and D. Grischkowsky. “THz parallel plate photonic waveguides”. In: *Appl. Phys. Lett.* 87 (2005), p. 051101.

[10] A. L. Bingham and D. Grischkowsky. “High Q, one-dimensional terahertz photonic waveguides”. In: *Appl. Phys. Lett.* 90 (2007), p. 091105.

[11] A. L. Bingham and D. Grischkowsky. “Terahertz two-dimensional high-Q photonic crystal waveguide cavities”. In: *Opt. Lett.* 33 (2008), pp. 348–350.

[12] S. Coleman and D. Grischkowsky. “Parallel plate THz transmitter”. In: *Appl. Phys. Lett.* 84 (2004), pp. 654–656.

[13] D. G. Cooke and P. U. Jepsen. "Optical modulation of terahertz pulses in a parallel plate waveguide". In: *Opt. Express* 16 (2008), pp. 15123–9.

[14] D. G. Cooke and P. U. Jepsen. "Dynamic optically induced planar terahertz quasioptics". In: *Appl. Phys. Lett.* 94 (2009), p. 241118.

[15] L. Gingras, M. Georgin, and D. G. Cooke. "Optically induced mode coupling and interference in a terahertz parallel plate waveguide". In: *Opt. Lett.* 39 (2014), pp. 1807–1810.

[16] L. Fekete, F. Kadlec, H. Němec, and P. Kužel. "Fast one-dimensional photonic crystal modulators for the terahertz range". In: *Opt. Express* 15 (2007), pp. 8898–8912.

[17] Mehmet Fatih Yanik and Shanhui Fan. "Stopping Light All Optically". In: *Phys. Rev. Lett.* 92 (2004), p. 083901.

[18] Q. F. Xu, P. Dong, and M. Lipson. "Breaking the delay-bandwidth limit in a photonic structure". In: *Nat. Phys.* 3 (2007), pp. 406–410.

[19] K. Fang, Z. Yu, and S. Fan. "Photonic Aharonov-Bohm effect based on dynamic modulation". In: *Phys. Rev. Lett.* 108 (2012), p. 153901.

[20] K. J. Fang, Z. F. Yu, and S. H. Fan. "Realizing effective magnetic field for photons by controlling the phase of dynamic modulation". In: *Nat Photonics* 6 (2012), pp. 782–787.

[21] K. Fang, Z. Yu, and S. Fan. "Photonic de Haas-van Alphen effect". In: *Opt. Express* 21 (2013), pp. 18216–24.

[22] Masaya Notomi. "Manipulating light with strongly modulated photonic crystals". In: *Rep. Prog. Phys.* 73 (2010), p. 096501.

[23] T. Kampfrath, D. M. Beggs, T. P. White, A. Melloni, T. F. Krauss, and L. Kuipers. "Ultrafast adiabatic manipulation of slow light in a photonic crystal". In: *Phys. Rev. A* 81 (2010).

[24] L. Fekete, F. Kadlec, P. Kužel, and H. Němec. "Ultrafast opto-terahertz photonic crystal modulator". In: *Opt. Lett.* 32 (2007), pp. 680–682.

[25] K. L. Yeh, M. C. Hoffmann, J. Hebling, and K. A. Nelson. "Generation of 10 μJ ultrashort terahertz pulses by optical rectification". In: *Appl. Phys. Lett.* 90 (2007), p. 171121.

[26] A. G. Stepanov, J. Hebling, and J. Kuhl. "Efficient generation of subpicosecond terahertz radiation by phase-matched optical rectification using ultrashort laser pulses with tilted pulse fronts". In: *Appl. Phys. Lett.* 83 (2003), pp. 3000–3002.

[27] H. Hirori, A. Doi, F. Blanchard, and K. Tanaka. "Single-cycle terahertz pulses with amplitudes exceeding 1 MV/cm generated by optical rectification in $LiNbO_3$". In: *Appl. Phys. Lett.* 103 (2013), p. 091106.

[28] F. Blanchard et al. "Effect of extreme pump pulse reshaping on intense terahertz emission in lithium niobate at multimilliJoule pump energies". In: *Opt. Lett.* 39 (2014), pp. 4333–4336.

[29] C. Jacoboni, C. Canali, G. Ottaviani, and A. Alberigi Quaranta. "A review of some charge transport properties of silicon". In: *Solid State Electronics* 20 (Feb. 1977), pp. 77–89. DOI: 10.1016/0038-1101(77)90054-5.

[30] J. M. Dorkel and P. Leturcq. "Carrier mobilities in silicon semi-empirically related to temperature, doping and injection level". In: *Solid State Electronics* 24 (Sept. 1981), pp. 821–825. DOI: 10.1016/0038-1101(81)90097-6.

[31] M. Scalora, M. J. Bloemer, A. S. Pethel, J. P. Dowling, C. M. Bowden, and A. S. Manka. "Transparent, metallo-dielectric, one-dimensional, photonic band-gap structures". In: *J. Appl. Phys.* 83 (1998), pp. 2377–2383.

[32] M. Theuer, A. J. Shutler, S. S. Harsha, R. Beigang, and D. Grischkowsky. "Terahertz two-cylinder waveguide coupler for transverse-magnetic and transverse-electric mode operation". In: *Appl. Phys. Lett.* 98 (2011).

[33] Laxmi Shiveshwari and Parmanand Mahto. "Photonic band gap effect in one-dimensional plasma dielectric photonic crystals". In: *Solid State Commun.* 138 (2006), pp. 160–164.

[34] C. Larsen, D. G. Cooke, and P. U. Jepsen. "Finite-difference time-domain analysis of time-resolved terahertz spectroscopy experiments". In: *J. Opt. Soc. Am. B* 28 (2011), pp. 1308–1316.

[35] G. Gallot, S. P. Jamison, R. W. McGowan, and D. Grischkowsky. "Terahertz waveguides". In: *J. Opt. Soc. Am. B* 17 (2000), pp. 851–863.

[36] Stephanie M. Teo et al. "Visualization of guided and leaky wave behaviors in an indium tin oxide metallic slab waveguide". In: *Opt. Express* 23 (2015), pp. 14876–14896.

Chapter 5

Direct temporal shaping of terahertz light pulses

5.1 Preface

In a way, this is really where it all began. After observing the waveforms reflected off the photoinjected structures through our FDTD simulations we decided to set aside the idea of dynamic injection of the 1-dimensional photonic structure to focus on the pulse-shaping aspect of the experiment. We believe that, due to the overwhelming number of methods available to generate single-cycle pulses of THz radiation and the relatively small number of solutions to create multi-cycle waveforms beyond passive spectral filters, our device would be truly enabling for control experiments. By this, we mean that, though broadband single-cycle pulses are extremely useful for spectroscopy measurements, the ability to generate elaborate pulse sequences with high field intensities is a remarkable tool if one seeks to control states of matter rather than just probe them. In this work, we showed not only that one could tune the spacing of the photoinjected lines and their number in order to control the linewidth and resonance but we were ambitious enough to demonstrate information encoding on THz waveforms. By digitally addressing a sequence of lines with a defined sequence of pump-on and pump-off states we generated 8-bit sequences of binary ASCII characters spelling the word "McGill". This was the first demonstration of this kind of pulse-shaping ability done directly in the THz spectrum and long pulse sequences demonstrated showed linewidth finesse equal to or better than those of current commercially available filters.

This work was performed and published in 2016 in the optical society of America's (OSA) journal *Optica* with the title "All-optical platform for THz pulse-shaping". The experimental work, from sample design and fabrication to data acquisition and analysis was performed by Lauren Gingras. François Blanchard, a post-doctoral fellow working in Pr. Cooke's lab at the time helped setup the $LiNbO_3$ source used to perform these experiments and provided extremely useful help both in the lab and during the article writing phase. Once more, David G. Cooke is listed as final author for supervising and helping along every step of the process.

This manuscript was submitted with a short supplementary section comprising only one figure and caption which is presented in the last subsection of this chapter.

5.2 Abstract

Active terahertz (THz) waveform synthesis is desirable for a broad range of applications including high speed wireless communications at Tb/s speeds and coherent manipulation of quantum systems driven by engineered light fields. In this work, we demonstrate an all-optical, fully reconfigurable platform for direct and arbitrary temporal shaping of broadband THz light pulses. The technique is based on an array of line photoexcitations of charge carriers within an otherwise homogeneous semiconductor embedded within a parallel plate waveguide (PPWG). The spatially periodic charge distributions locally modulate the THz dielectric function, mapping each photoexcited line in the array directly to a reflected single-cycle THz pulse. Tuning the spatial distribution of the line excitations, arbitrarily-shaped THz pulse sequences can be created from a single THz input pulse with relatively little intrinsic loss. We demonstrate synthesis of multi-cycle THz waveforms, 8-bit digital pulse sequences and THz frequency combs with control over amplitude, central frequency and linewidth.

5.3 Introduction

The temporal shaping and encoding of information on a THz lightwave is key to achieving Tb/s wireless data transfer rates [1–3]. At the same time, THz time-domain spectroscopy has evolved from measuring the broadband linear response of materials to highly nonlinear, coherent manipulations of quantum systems requiring advanced control over the pulse field profile [4–7]. Given

a robust, broadband control scheme over the THz pulse amplitude and phase, multiple phase-locked THz pulse sequences can be generated and used to manipulate quantum states in the same manner as microwave pulses are currently used in multi-pulse nuclear magnetic resonance (NMR) spectroscopy [8]. Passive shaping of THz fields accomplishes this in a static manner using spectral filters, including plasmonic [9, 10], metamaterial [11, 12] or photonic structures [13]. Extensions of these methods to active mode operation provides tunability over the targeted modulated bandwidth, often through pulsed photoexcitation, however commonly only in the vicinity of the engineered resonance [14–23] or photonic band gap [24, 25]. More direct approaches to narrowband THz generation have been heavily developed by low-temperature-operated quantum cascade lasers [26, 27] and by tunable difference frequency mixing of optical pumps in a nonlinear crystal [28] such as in injection-seeded THz-wave parametric generation (IS-TPG) [29]. These methods, however, offer a limited amount of control over the output central frequency and bandwidth.

In order to achieve broadband THz waveform envelope control, spatial or temporal shaping of femtosecond optical pump pulse driving THz generation in an electro-optic crystal or a photoconductive antenna has been applied [30–32]. Though very versatile, the damage threshold of programmable optics used to perform optical pulse shaping, such as spatial light modulators (SLM), often limits the total amount of pump energy available to generate the THz pulse train and therefore limits the output THz power. Schemes that use gated antennas to generate THz waves from temporally-shaped optical pulses, while simple, are inherently limited by current saturation in the semiconductor. Nonlinear optical methods for generating intense single-cycle THz pulses with photon quantum conversion efficiencies at or exceeding 100% now exist, such as tilted pulse front optical rectification in $LiNbO_3$ [33–35]; waveform synthesis techniques that operate directly in the THz domain are desirable to take advantage of these high power sources. In this work, we demonstrate a flexible platform for arbitrary shaping of THz waveforms driven by such intense, single cycle THz pulses.

5.4 Methods

The pulse shaping method is based on spatially-patterned photo-injected charge carrier distributions inside a semiconductor-filled THz parallel-plate waveguide (PPWG), which we have previously demonstrated as a versatile platform to modulate the amplitude [36], propagation direction and pulse delay [37], mode coupling [38], and frequency content of THz pulses [39].

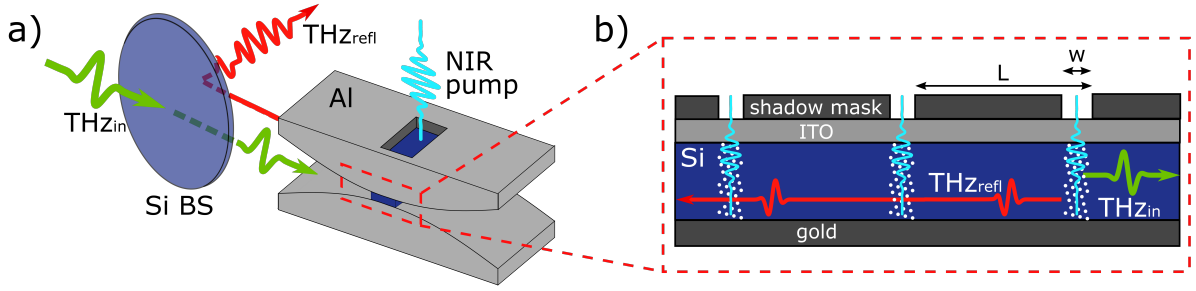

FIGURE 5.1: (a) Schematic representation of the experimental setup. A single-cycle THz pulse (green) is coupled into a dielectric-filled parallel-plate waveguide and detected in reflection geometry. (b) An optically transparent ITO coating allows spatially defined charge carrier injection (dotted regions) using above-bandgap pulses of NIR light (light blue). The periodically repeating photoinjected metallic regions (dotted regions) partially reflect the incident THz pulse to generate a multi-cycle THz signal (red).

Input THz pulses, polarized perpendicular to the plates, are efficiently coupled into the dispersionless TEM mode of the PPWG and interact with the optically-injected photoconductive regions. Importantly, these can be sub-THz wavelength in their spatial extent due to the much smaller diffraction limit of the defining optical pump pulse and small diffusive spread in the picoseconds after injection. In this work, we create a one dimensional metal-dielectric line array within the waveguide that controllably and reversibly creates replicas of an incident single-cycle THz pulse, with a temporal spacing between replicas governed by the periodicity of the lines. We demonstrate multi-cycle envelope-engineered pulses with control over the frequency, linewidth, and phase as well as encoding of a digital 8-bit binary sequence onto a THz waveform.

The experiment uses a THz single-cycle pulse generated by tilted pulse-front optical rectification in a $LiNbO_3$ crystal [33, 40]. This pulse couples into a tapered aluminum PPWG [41], as illustrated in Fig. 5.1(a). A 10 mm-thick float-zone silicon beamsplitter (BS) at 45° is placed before the PPWG and redirects 65% of the reflected signal (red) for detection performed with electro-optic sampling in a ZnTe crystal. A window etched in the top tapered aluminum plate permits the 1070 nm pump pulse from an optical parametric amplifier to photoexcite the embedded sample. Figure 5.1(b) shows a side view of the embedded Si wafer; gold and ITO coatings confine the THz light for dispersionless propagation in the transverse electro-magnetic (TEM) mode. In the low carrier density regime where all frequency components of the THz pulse are below the photoinduced plasma frequency ω_p, the finite conductivity of the optically transparent ITO dominates the waveguide loss through the power absorption coefficient $\alpha_{wg} = n_{Si}R_S/(Z_0 d) = 0.6\ cm^{-1}$ where $n_{Si} = 3.42$ is the refractive index at THz frequencies inside silicon, Z_0 is the vacuum permittivity, $d = 150\ \mu m$ is the waveguide thickness and $R_S \simeq 1\ \Omega$/square is the sheet resistance of the ITO layer [36]. The photon energy of the pump

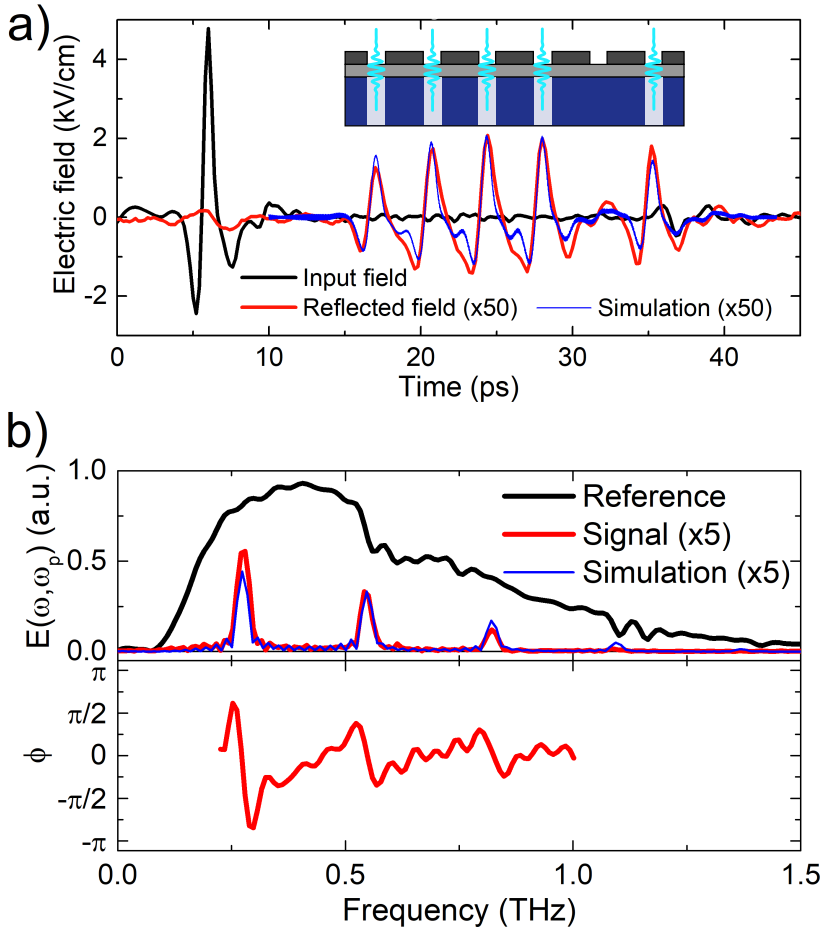

FIGURE 5.2: (a) Typical input pulse (black) and reflected pulse replicas (red) for 20 μm wide pumped lines (w) with a lattice pitch (L) of 160 μm. Accompanying FDTD simulation results (blue) using the reference pulse shape as input. A digital sequence (111101) is created by photoexciting all lines but the 5^{th} (inset). (b, top) Incident electric field amplitude (black), synthesized frequency comb (red) and simulated signal (blue) for 12 photoinjected lines of 20 μm width (w) and 160 μm period (L). (b, bottom) Spectral phase of the experimentally synthesized multi-cycle signal.

(1.16 eV) is tuned just above the band gap energy of silicon (1.12 eV) to take advantage of the > 1 mm penetration depth [42], injecting charge carriers uniformly through the thickness of the silicon to avoid scattering into higher order modes [38]. In our operation regime, the photoinduced charge carrier densities ($\sim 10^{15}$ cm^{-3}) are kept one order of magnitude lower than the threshold for mobility reduction due to electron-hole scattering [43]. Furthermore, the fluence employed (10 μJ/cm^2) is still 3 orders of magnitude below the optical damage threshold for silicon excited at a wavelength of 1060 nm with 100 fs pulses [44]. A shadow mask placed atop the transparent ITO layer ($\sim$10% transmission at 1070 nm) spatially shapes the photoexcitation to induce a periodic photoconductivity modulation along the THz propagation direction, creating a zero-gap, 1-dimensional metal-dielectric photonic crystal structure with a sharp transmission and reflection enhancement (compared to uniform illumination) at a frequency $f_m = mc_0/(2n_{Si}L)$,

where m is an integer, c_0 the vacuum speed of light and L is the periodicity of the array [39, 45]. We note the complex valued index modulation (Re(n) $\simeq$ Im(n)) is intrinsically different from a distributed Bragg reflector, which is based solely on index modulation and exhibits a gap in the photon density of states. Furthermore, the predominant single-cycle character of the transmitted pulse inhibits the pulse-shaping ability in transmission mode, thus all experiments are performed in reflection configuration.

5.5 Results and discussion

An example of the input and reflected THz waveforms are shown in Fig. 5.2(a) where the black line is collected from the air-Si interface reflection inside the tapered PPWG. A digital sequence (red curve) of (111101) is created with 1 denoting a photoexcited line and 0 an unexcited line, as shown in the inset diagram. The amplitude of the THz reflection from each individual lines (1% here) increases with charge carrier density and therefore pump fluence, providing a way to greyscale adjust the relative peak amplitude of each pulse in the waveform. The Gaussian spatial intensity profile of the pump pulse illuminating the entire 1 dimensional array is then imprinted along the time-axis of the synthesized waveform. The shadow mask period (L) and line width (w) used are 160 and 20 μm, respectively. The blue curve shows finite-difference time-domain (FDTD) simulation results using the aforementioned experimental parameters and using the experimental reference electric field profile as an input field. We use a Gaussian spatial pump intensity profile to replicate the experimental conditions and reproduce the experimental results with good agreement.

Generating a waveform composed of 12 pulse replicas with the aforementioned parameters leads to the synthesis of a frequency comb with line separation $\Delta\nu = c_0/(2n_{Si}L) = 274$ GHz. The incident broadband electric field amplitude (black, top) and reflected frequency comb (red, top) presented in Fig. 5.2(b) demonstrate the clear spectral reshaping induced by a 10 μJ NIR pump pulse. The blue curve shows that the FDTD simulations reproduce the spectrum of the synthesized waveform very well with a faster decay of experimental reflection in frequency due to guiding losses. The bandwidth of the incident pulse determines the highest harmonic achievable for a given line separation as well as the frequency range where single-harmonic sythesis can be achieved. The red curve in the lower panel shows the associated spectral phase of the reflected waveform in the vicinity of the first three resonances with high and low frequency ranges omitted due to low signal.

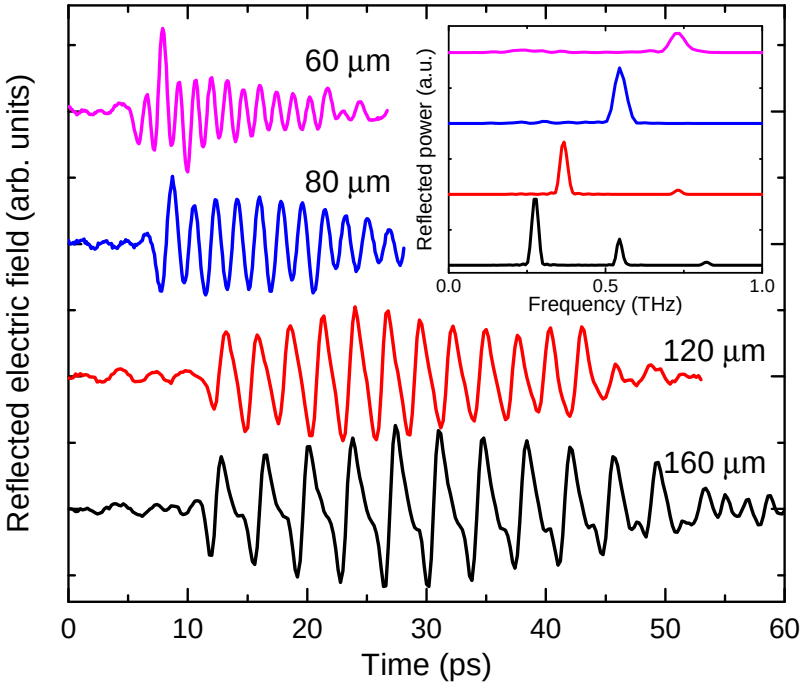

FIGURE 5.3: Electric field time trace of the 12-line frequency combs and associated power spectrum (inset) for various lattice pitches (L) at constant pump energy (15 μJ) and line width (w=20 μm).

The frequency comb can be tuned continuously within the input THz pulse bandwidth by adjusting the lattice pitch (L). Figure 5.3 shows the effect of tuning the lattice pitch from 160 μm (black curve) to 60 μm (pink curve) with a constant line width (w = 20 μm) and line number (12). Consequently, the first order resonance is shifted from 0.27 THz to 0.73 THz, as shown in the inset. The input bandwidth determines how short the input pulse is in time and thus how closely lines can be brought together before replicas start overlapping temporally. When the overlap is significant, envelope reshaping can occur as can be observed in the peaked oscillations at early times of the 60 μm (pink) data set. For the largest pitch of 160 μm, where multiple resonances lie within the input pulse bandwidth, a gradual drift can be seen in the carrier envelope phase of each replica from 14 ps to 47 ps, respectively. This evolution in the carrier envelope phase is due to the dispersion induced within the photoexcited regions in the vicinity of the plasma frequency ($\omega_p/2\pi \simeq 1.3$ THz). When a single resonance is present within the input bandwidth and is located far enough from the plasma frequency (e.g. the L = 80 μm waveform in Fig. 5.3) the resulting waveform is purely monochromatic and has envelope characteristics solely governed by the pump intensity profile.

Bandwidth tuning of the THz waveforms is achieved simply by adjusting the number of photoexcited lines in the array. As the pump intensity profile is narrowed, using an adjustable slit

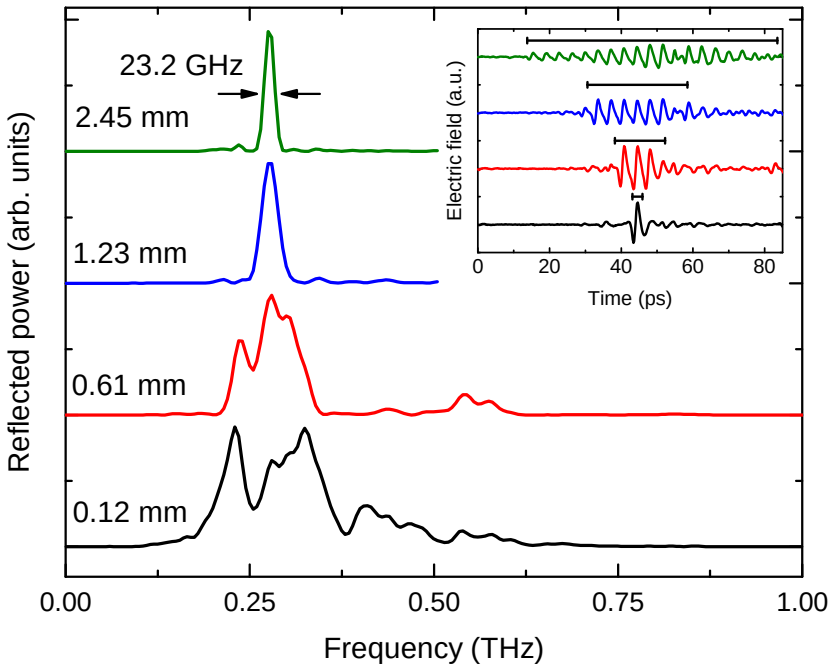

FIGURE 5.4: Power spectrum and corresponding electric field time traces (inset) for varying spatial pump widths. The horizontal lines (inset) show the equivalent spatial pump width used to tune the number of cycles.

just above the shadow mask, fewer lines are injected resulting in fewer pulse replicas and broader bandwidth. Linewidth tuning, shown in Fig. 5.4, becomes evident as the pump spatial extent is broadened from 0.12 mm (black) to 2.45 mm (green) with the inset showing the synthesized electric field time traces. We observe excellent agreement between the waveform envelope extent and the time equivalent of the spatial extent of the slit opening (horizontal black lines, inset). The full extent of the illumination (green) generates a 20-cycle THz waveform with a linewidth of 23.2 $\pm$ 0.4 GHz at a 274 GHz central frequency, or a spectral purity of 8% which rivals commercially available THz bandpass filters. The Gaussian profile of the pump is again responsible for the lower electric field values at early and late times. The minimum linewidth achieved is limited only by the number of lines etched in the sample shadow mask and by the size of the optical port etched in the aluminum tapered PPWG (Fig. 5.1(a)).

Numerical simulations were performed using commercially available FDTD software (Lumerical) to further understand the limitations of the technique. By tuning the plasma frequency, ω_p, of a set of 12 lines of 20 μm width with a 160 μm period up to 19 THz, the reflected waveform is tuned from a multi-cycle to a single-cycle waveform (Fig. 5.5(a)). In the scenario where the plasma frequency is significantly greater than the input THz pulse bandwidth the transmission coefficient of individual lines $t(\omega_p)$ becomes the limiting factor to the total number of pulses

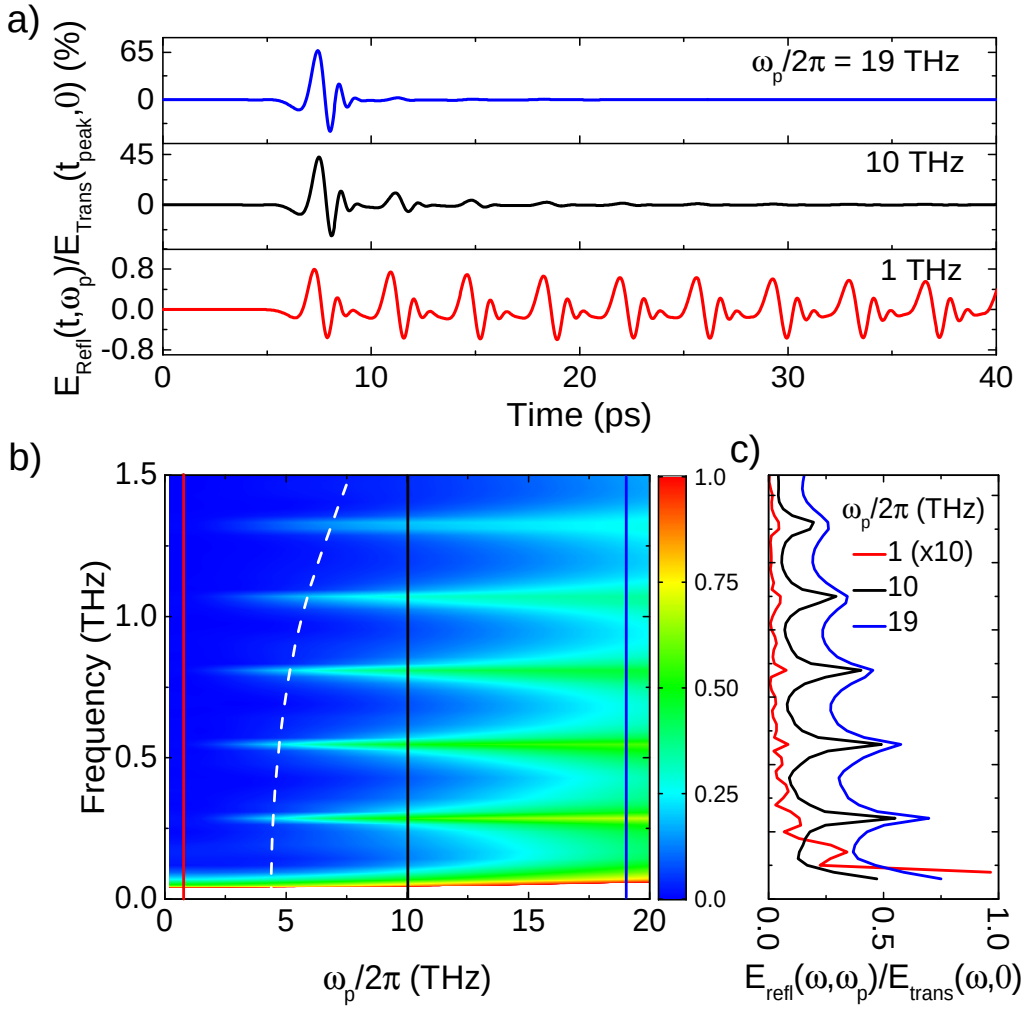

FIGURE 5.5: (a) Simulated (FDTD) reflected THz waveforms for 12 lines of 20 μm thickness with 160 μm period for indicated pump-induced plasma frequencies. (b) Reflected spectrum as a function of pump-induced plasma frequency ($E_{Refl}(\omega,\omega_p)/E_{Trans}(\omega,0)$). The white dashed line denotes the transfer matrix method solution for 25% field reflection from a single 20 μm line. (c) Reflected spectrum for fixed ω_p values (from (b)).

an array can contain. The reflected peak amplitude of the n^{th} line in the array scales as $E_n = E_0 \cdot r \cdot t^{2(n-1)}$ where E_0 is the incident field amplitude and $r(\omega_p)$ is the individual line reflection coefficient. The peak field reflection coefficient can reach up to 65% at $\omega_p/2\pi = 19$ THz. Provided that r is on the order of 1%, as in our experiments, light can traverse the entire array and back without significant loss compared to the first line reflection. The spectral amplitude reflection ($E_{Refl}(\omega,\omega_p)/E_{Trans}(\omega,0)$) plotted in Fig. 5.5(b) shows the continuous transition between 10^{15} and 10^{18} cm^{-3} electron density regimes. Vertical cuts in Fig. 5.5(b) show the corresponding reflection spectra in Fig. 5.5(c) for the datasets presented in (a). We can see that as the plasma frequency reaches 10 THz (black line) a broadband background reflection becomes evident and even more pronounced as ω_p reaches 19 THz (solid blue line).

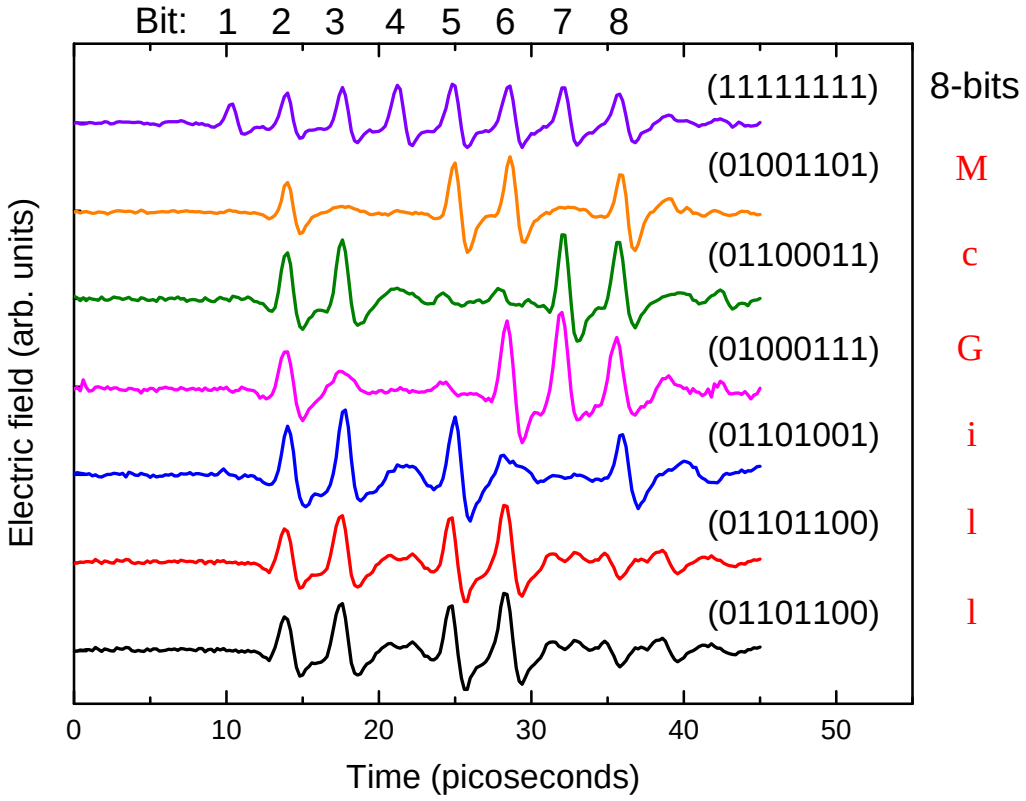

FIGURE 5.6: 8-bit array of binary 1s (pulse present) and 0s (pulse absent) encoded in a THz pulse train. The pulse sequences presented here spell "McGill" in 8-bit binary ASCII characters. The 20 μm wide lines are photoinjected using a 10 μJ pump pulse with a lattice pitch of 160 μm.

Transfer matrix calculations corresponding to a constant 25% field reflection off a single 20 μm thick photoinjected slab are shown in Fig. 5.5(b) by the dashed white curve. When the frequency is increased, higher plasma frequencies are required to achieve the same amount of reflection, as expected. The good agreement between this curve and the resonant peak roll-off from FDTD simulations confirms the Drude response of the media is responsible for the frequency dependence of the peak reflectivity and not disorder in the array.

Finally, each line in the photoexcited array can be independently addressed to individually modulate the replica pulses in the THz waveform. Thus, information can be encoded into the pulse train using binary 1's (pulse present) and 0's (pulse absent), as demonstrated in Fig. 5.6. The top-most waveform (purple) shows all 8 field cycles in the "1" state with subsequent data sets displaying binary sequences that spell "McGill" in 8-bit binary American Standard Code for Information Interchange (ASCII). The shadow mask has a 160 μm pitch with 20 μm wide lines and is pumped with 10 μJ pulse energy. Again, variations in peak field amplitudes, or greyscaling, is caused by the inhomogeneous pump intensity distribution. For demonstration

purposes the array is limited to 8 cycles, or bits, though in the $\omega_p/2\pi \simeq 1$ THz regime FDTD simulations indicate that 32 bits could be encoded with $> 35\%$ peak fields ratio between the 1^{st} and last electric field cycle due to the enhanced THz transmission on resonance [46] (see supplementary materials). It is worth noting that using a pump fluence that increases with the number of lines can help circumvent diminishing signals as the number of photoinjected lines increases. Furthermore, the high transmission ratio of this device enables recycling of the incident single-cycle pulse when operating in the non-depleting $\omega_p/2\pi \simeq 1$ THz regime. Cascading arrays thus makes it possible to generate multiple bit sequences from a single input pulse.

5.6 Conclusion

We have demonstrated temporal shaping of broadband THz light using spatially controlled photoinjected charge carriers inside a PPWG. THz waveforms were synthesized from of a single incident THz pulse using periodic one dimensional arrays, creating frequency combs that are completely tunable in frequency, bandwidth, amplitude and chirp. Moreover, individually addressing each line excitation in the array allows on-off keying of information onto a THz pulse train. Leveraging high peak field THz pulses, this platform can be used to arbitrarily tailor multi-cycle pulse sequences for quantum control schemes of meV scale excitations in matter, or to encode information for THz wireless transmission anywhere within the input bandwidth. The all-optical nature of this device makes it fully-reversible and reconfigurable after charge-carrier recombination. This refresh rate could be pushed to the GHz range using direct band gap semiconductors with shorter carrier lifetimes such as GaAs and two photon excitation.

5.7 Funding information

The authors are grateful to the Fonds de Recherche du Québec - Nature et Technologies (FRQNT) and the Natural Sciences and Engineering Research Council (NSERC) for funding.

5.8 Supplementary materials

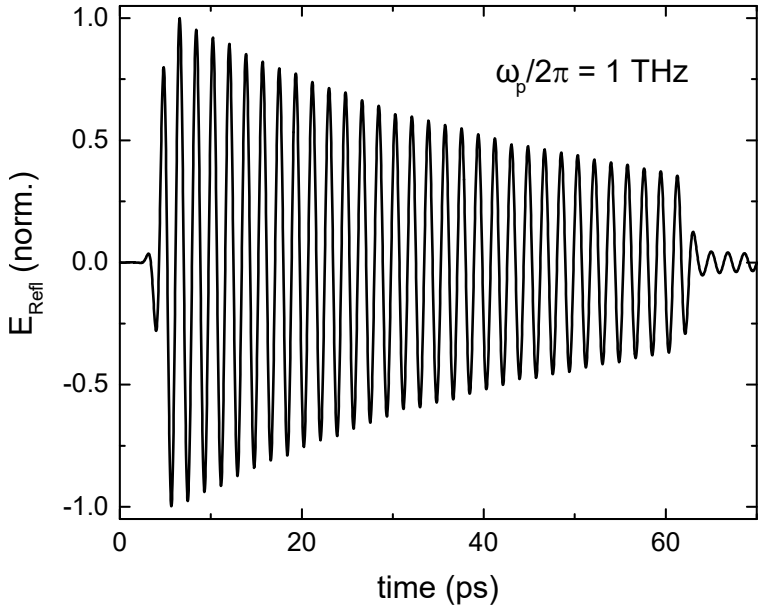

Fig. S1. Simulated reflected electric field for 32 lines of 20 μm width and 80 μm pitch. The plasma frequency is set to 1 THz for all lines showing a 35% peak field ratio between the 1st and 32nd line. The waveguide losses due to finite plate conductivity would add a 14.2% decay for the last field line, leading to a 30% total peak field return.

References

[1] Lothar Möller, John Federici, Alexander Sinyukov, Chongjin Xie, Hee Chuan Lim, and Randy C. Giles. "Data encoding on terahertz signals for communication and sensing". In: *Opt. Lett.* 33 (2008), pp. 393–395.

[2] KoenigS et al. "Wireless sub-THz communication system with high data rate". In: *Nat Photon* 7.12 (2013), pp. 977–981.

[3] T. Nagatsuma et al. "Terahertz wireless communications based on photonics technologies". In: *Opt. Express* 21 (2013), pp. 23736–23747.

[4] B. E. Cole, J. B. Williams, B. T. King, M. S. Sherwin, and C. R. Stanley. "Coherent manipulation of semiconductor quantum bits with terahertz radiation". In: *Nature* 410 (2001), pp. 60–63.

[5] Tobias Kampfrath et al. "Coherent terahertz control of antiferromagnetic spin waves". In: *Nat. Photon.* 5 (2011), pp. 31–34.

[6] S. Fleischer, R. W. Field, and K. A. Nelson. "Commensurate Two-Quantum Coherences Induced by Time-Delayed THz Fields". In: *Phys. Rev. Lett.* 109 (2012).

[7] R. Matsunaga et al. "Light-induced collective pseudospin precession resonating with Higgs mode in a superconductor". In: *Science* 345 (2014), pp. 1145–1149.

[8] N. A. Gershenfeld and I. L. Chuang. "Bulk spin-resonance quantum computation". In: *Science* 275 (1997), pp. 350–356.

[9] L. Ju et al. "Graphene plasmonics for tunable terahertz metamaterials". In: *Nat. Nanotechnol.* 6 (2011), pp. 630–634.

[10] A. Paulsen and A. Nahata. "K-space design of terahertz plasmonic filters". In: *Optica* 2 (2015), pp. 214–220.

[11] D. W. Porterfield, J. L. Hesler, R. Densing, E. R. Mueller, T. W. Crowe, and R. M. Weikle. "Resonant Metal-Mesh Bandpass-Filters for the Far-Infrared". In: *Appl. Optics* 33 (1994), pp. 6046–6052.

[12] A. C. Strikwerda, M. Zalkovskij, D. L. Lorenzen, A. Krabbe, A. V. Lavrinenko, and P. U. Jepsen. "Metamaterial composite bandpass filter with an ultra-broadband rejection bandwidth of up to 240 terahertz". In: *Appl. Phys. Lett.* 104 (2014).

[13] N. Jukam and M. S. Sherwin. "Two-dimensional terahertz photonic crystals fabricated by deep reactive ion etching in Si". In: *Appl. Phys. Lett.* 83 (2003), pp. 21–23.

[14] C. Janke, J. Gómez Rivas, P. H. Bolivar, and H. Kurz. "All-optical switching of the transmission of electromagnetic radiation through subwavelength apertures". In: *Opt. Lett.* 30 (2005), pp. 2357–2359.

[15] H. Němec, P. Kužel, L. Duvillaret, A. Pashkin, M. Dressel, and M. T. Sebastian. "Highly tunable photonic crystal filter for the terahertz range". In: *Opt. Lett.* 30 (2005), pp. 549–551.

[16] H. T. Chen, W. J. Padilla, J. M. O. Zide, A. C. Gossard, A. J. Taylor, and R. D. Averitt. "Active terahertz metamaterial devices". In: *Nature* 444.7119 (2006), pp. 597–600.

[17] L. Fekete, F. Kadlec, P. Kuzel, and H. Nemec. "Ultrafast opto-terahertz photonic crystal modulator". In: *Optics Letters* 32.6 (2007), pp. 680–682.

[18] E. Hendry, M. J. Lockyear, J. Gómez Rivas, L. Kuipers, and M. Bonn. "Ultrafast optical switching of the THz transmission through metallic subwavelength hole arrays". In: *Phys. Rev. B* 75 (2007).

[19] J. Han and A. Lakhtakia. "Semiconductor split-ring resonators for thermally tunable terahertz metamaterials". In: *J. Mod. Optic* 56 (2009), pp. 554–557.

[20] J. Tao, X. G. Huang, X. S. Lin, Q. Zhang, and X. P. Jin. "A narrow-band subwavelength plasmonic waveguide filter with asymmetrical multiple-teeth-shaped structure". In: *Optics Express* 17.16 (2009), pp. 13989–13994.

[21] S. F. Busch, S. Schumann, C. Jansen, M. Scheller, M. Koch, and B. M. Fischer. "Optically gated tunable terahertz filters". In: *Appl. Phys. Lett.* 100 (2012).

[22] N. Born, M. Reuter, M. Koch, and M. Scheller. "High-Q terahertz bandpass filters based on coherently interfering metasurface reflections". In: *Opt. Lett.* 38 (2013), pp. 908–910.

[23] N. Born, M. Scheller, M. Koch, and J. V. Moloney. "Cavity enhanced terahertz modulation". In: *Appl. Phys. Lett.* 104 (2014).

[24] J. Li. "Terahertz modulator using photonic crystals". In: *Opt. Commun.* 269 (2007), pp. 98–101.

[25] T. Kampfrath, D. M. Beggs, T. P. White, A. Melloni, T. F. Krauss, and L. Kuipers. "Ultrafast adiabatic manipulation of slow light in a photonic crystal". In: *Physical Review A* 81.4 (2010).

[26] J. Faist, F. Capasso, D. L. Sivco, C. Sirtori, A. L. Hutchinson, and A. Y. Cho. "Quantum Cascade Laser". In: *Science* 264.5158 (1994), pp. 553–556.

[27] R. Köhler et al. "Terahertz semiconductor-heterostructure laser". In: *Nature* 417 (2002), pp. 156–159.

[28] E. R. Brown, K. A. Mcintosh, K. B. Nichols, and C. L. Dennis. "Photomixing up to 3.8-THz in Low-Temperature-Grown GaAs". In: *Appl. Phys. Lett.* 66 (1995), pp. 285–287.

[29] K. Kawase, J. Shikata, and H. Ito. "Terahertz wave parametric source". In: *J. Phys. D Appl. Phys.* 35 (2002), R1–R14.

[30] J. Liu, J. K. Butler, G. A. Evans, and A. Rosen. "Analysis of millimeter wave phase shifters coupled to a fixed periodic structure". In: *Ieee Transactions on Microwave Theory and Techniques* 44.8 (1996), pp. 1416–1423.

[31] J. Ahn, A. V. Efimov, R. D. Averitt, and A. J. Taylor. "Terahertz waveform synthesis via optical rectification of shaped ultrafast laser pulses". In: *Opt. Express* 11 (2003), pp. 2486–2496.

[32] M. Sato et al. "Terahertz polarization pulse shaping with arbitrary field control". In: *Nat. Photonics* 7 (2013), pp. 724–731.

[33] K. L. Yeh, M. C. Hoffmann, J. Hebling, and K. A. Nelson. "Generation of 10 μJ ultrashort terahertz pulses by optical rectification". In: *Applied Physics Letters* 90.17 (2007).

[34] J. A. Fülöp et al. "Generation of sub-mJ terahertz pulses by optical rectification". In: *Opt. Lett.* 37 (2012), pp. 557–559.

[35] F. Blanchard et al. "Effect of extreme pump pulse reshaping on intense terahertz emission in lithium niobate at multimilliJoule pump energies". In: *Opt. Lett.* 39 (2014), pp. 4333–4336.

[36] D. G. Cooke and P. U. Jepsen. "Optical modulation of terahertz pulses in a parallel plate waveguide". In: *Opt. Express* 16 (2008), pp. 15123–9.

[37] D. G. Cooke and P. U. Jepsen. "Dynamic optically induced planar terahertz quasioptics". In: *Appl. Phys. Lett.* 94 (2009), p. 241118.

[38] L. Gingras, M. Georgin, and D. G. Cooke. "Optically induced mode coupling and interference in a terahertz parallel plate waveguide". In: *Opt. Lett.* 39 (2014), pp. 1807–1810.

[39] L. Gingras, F. Blanchard, M. Georgin, and D. G. Cooke. "Dynamic creation of a light-induced terahertz guided-wave resonator". In: *Opt. Express* 24 (2016), pp. 2496–2504.

[40] A. G. Stepanov, J. Hebling, and J. Kuhl. "Efficient generation of subpicosecond terahertz radiation by phase-matched optical rectification using ultrashort laser pulses with tilted pulse fronts". In: *Applied Physics Letters* 83.15 (2003), pp. 3000–3002.

[41] S. H. Kim, E. S. Lee, Y. Bin Ji, and T. I. Jeon. "Improvement of THz coupling using a tapered parallel-plate waveguide". In: *Optics Express* 18.2 (2010), pp. 1289–1295.

[42] Carsten Schinke et al. "Uncertainty analysis for the coefficient of band-to-band absorption of crystalline silicon". In: *AIP Advances* 5 (2015), p. 067168.

[43] V. Grivitskas, M. Willander, and J. Vaitkus. "The Role of Intercarrier Scattering in Excited Silicon". In: *Solid State Electron.* 27 (1984), pp. 565–572.

[44] P. P. Pronko et al. "Avalanche ionization and dielectric breakdown in silicon with ultrafast laser pulses". In: *Phys. Rev. B* 58 (1998), pp. 2387–2390.

[45] Laxmi Shiveshwari and Parmanand Mahto. "Photonic band gap effect in one-dimensional plasma dielectric photonic crystals". In: *Solid State Communications* 138.3 (2006), pp. 160–164.

[46] M. Scalora, M. J. Bloemer, A. S. Pethel, J. P. Dowling, C. M. Bowden, and A. S. Manka. "Transparent, metallo-dielectric, one-dimensional, photonic band-gap structures". In: *J. Appl. Phys.* 83 (1998), pp. 2377–2383.

Chapter 6

Active phase control of terahertz pulses using a dynamic waveguide

6.1 Preface

At this point, we hope the readers are well acquainted with the method developed for pulse shaping and its advantages. What is important to emphasize though is that one of the major drawbacks of the experiments presented previously was the necessity to use an OPA to convert the wavelength of the pump light. As mentioned, poor pointing stability as well as extremely distorted wavefronts prevented us from using more refined imaging methods to fashion the pump intensity onto the sample. This impediment, we ended up solving through the establishment of a collaboration with Pr. Ménard's group at the University of Ottawa. By using their Yb:KGW laser, which is well suited for tilted pulse-front THz generation in $LiNbO_3$ as well as uniformly pumping our silicon waveguide, we were able to extend the pulse-shaping method one step further. We should mention that the expertise of Pr. Ménard is also extremely conveniently suited to some of the projected experiments, briefly mentioned in the next chapter. The integration of a spatial light modulator (SLM) is perhaps one of the most enabling improvement as it allows for reconfigurability of the pump intensity pattern at a 60 Hz refresh rate. This, in principle eliminates the need for a lithographically-defined permanent shadow mask atop the waveguide. However, most of the experiments performed here still employ a shadow mask which provides unparalleled pump intensity contrast and definition. For this work, we demonstrated not only multi-cycle amplitude modulation but also phase modulation of a broadband single-cycle THz

pulse as well as the generation of arbitrarily-chirped waveforms. Demonstrations of arbitrary phase shifting of broadband pulses have been made in the THz domain though most of them are somewhat limited since they rely on mechanical actuation, which is slow. As for arbitrarily chirped pulses, no demonstration has ever been made in the THz domain, to the best of our knowledge. For this, we believe that this platform has proven not just to be useful but to be truly ground breaking as a source for THz-induced control and field-induced manipulation experiments. We hope to elaborate on some of those and present preliminary results in chapter 7.

This work was a natural extension of that presented in the previously chapter and was thus submitted and published in 2018 to the *Optics Express* journal with the title "Active phase control of terahertz pulses using a dynamic waveguide". The experimental work published in this manuscript was performed in vast majority by Lauren Gingras with some help from Pr. Ménard's students Wei Cui and Aidan W. Schiff-Kearn. Professor Jean-Michel Ménard himself was also extremely useful in helping with the manuscript and with some of the experimental improvements. Once again, David Cooke has showed outstanding feats of supervision throughout the preparation, execution, and publication of this work, most of which was performed sitting at a coffee shop or at a picnic bench near Burnside Hall.

6.2 Abstract

Control over the spectral phase of a light pulse is a fundamental step toward arbitrary signal generation in a spectral band. For the terahertz spectral regime, pulse shaping holds the key for applications ranging from ultra-high speed wireless data transmission to quantum control with shaped fields. In this work, we demonstrate a technique for all-optical and reconfigurable control of the spectral phase of a light pulse in the important terahertz (THz) band. The technique is based on interaction of a guided THz pulse with patterned photoexcited regions within a uniform silicon-filled parallel-plate waveguide. We use this platform to demonstrate broadband and tunable positive and negative chirp of a THz pulse, as well as control of the pulse carrier envelope phase.

6.3 Introduction

Terahertz (THz) light is an important spectroscopic tool for probing low energy excitations in condensed matter [1–3], molecular [4, 5] and biological systems [6, 7]. Recently nonlinear spectroscopy in this spectral region has become possible [8], due to efficient generation of intense THz pulses [9–11]. States-of-matter can now be prepared and manipulated using engineered THz fields in the time domain [12, 13]. A key aspect of any such optical coherent control experiment is a means to tune the pulse spectral phase, ideally in a fast and reconfigurable manner. Such phase control can be used to change the evolution of these states in a prescribed manner, enhancing desired interactions and suppressing background signals [14]. Many highly nonlinear interactions are also crucially sensitive to the absolute, or carrier-envelope phase (CEP), of the pulse. THz-scanning tunnelling microscopy, for example, using the THz pulse field as a temporal gate, is intrinsically sensitive to the CEP of the pulse [15–20]. Field emission of electrons from a metal nanotip [21–23] also depends critically on the pulse polarity.

The phase of a THz pulse generated using short pulsed lasers is intrinsically locked at generation. Control over the chirp of the THz pulse has most commonly been accomplished post-generation, by introducing a dispersive medium with variable thickness in the beam path [24], or by using stacked prism wave plates [25]. There are far fewer methods for controlling the CEP of the pulse, for example by using the Guoy shift at the THz focus or by variable delay between two pulses undergoing difference frequency generation in a nonlinear crystal [26]. Though simple, these methods rely on mechanical actuation of the dispersive element or optical delay stage, which is slow. A handful of demonstrations have also been made for tunable narrowband THz generation [27–31], though again few solutions adjust the waveform chirp in an active fashion.

In this work, we demonstrate a technique for complete phase control of THz light pulses. Our technique shapes the phase of THz pulses by reflection from patterned photoexcited regions inside a silicon-filled parallel-plate waveguide (PPWG). These light-induced reflectors are spatially tailored in the propagating plane of the THz pulse using a two dimensional spatial light modulator (SLM). This makes them fully reconfigurable and capable of introducing both negative and positive chirp and gives control over the CEP. We believe the versatility that this platform offers will make it a useful tool for several THz applications.

6.4 Methods

The technique relies on a silicon-filled PPWG, depicted in Fig. 1(a) and detailed in previous work [32]. The THz pulse is coupled and guided in the dispersionless TM_{00} mode. The silicon is made optically addressable by using a transparent conductive oxide coating as a top plate, thereby allowing photoexcitation of the silicon within and creating localized metallic domains experienced by the THz pulse propagating in the plane. This optically addressable THz waveguide is a versatile platform for a variety of THz pulse control experiments, having already demonstrated amplitude modulation [33], pulse delay and beam steering [34], guided mode coupling [35], frequency selection [36], tunable frequency comb generation and information encoding [32].

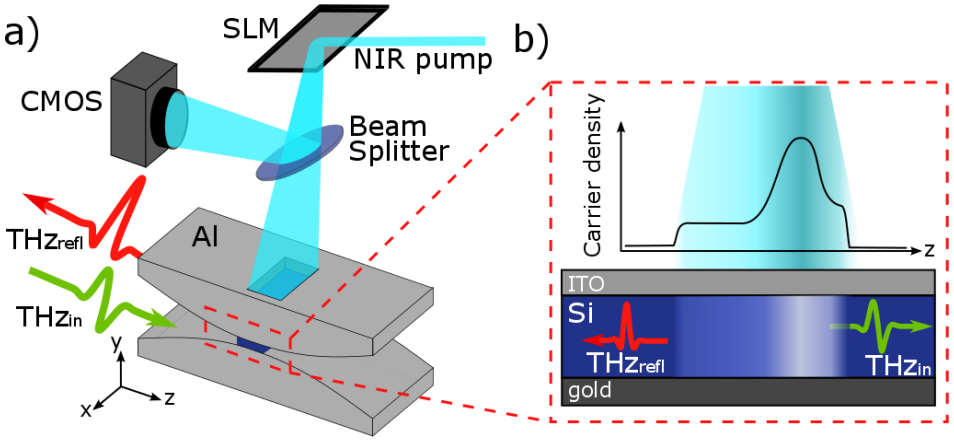

FIGURE 6.1: (a) Schematic representation of the experiment where a broadband single-cycle THz pulse is coupled in a PPWG. The dielectric-filled waveguide is pumped with a NIR pulsed source which is spatially patterned using a SLM. A CMOS camera records the intensity profile reflected by a beamsplitter. (b) Cross-section of the PPWG where a spatially shaped pump photoinduces a phase-shifting reflector for the THz pulse.

For these experiments, a solid-state Yb:KGW femtosecond laser amplifier providing 180 fs duration, 1 mJ pulses with a center wavelength of 1028 nm was used to generate, detect and modulate the THz pulse. THz pulses were efficiently generated by tilted pulse-front optical rectification in a $LiNbO_3$ prism. The platform's core consists of a tapered aluminium PPWG that provides coupling between free-space and a silicon-filled guided section [32]. A 150 nm gold layer is deposited on the bottom side of a double-side polished, 150 μm thick high resistivity float zone silicon slab (resistivity $>$ 10,000 Ω-cm). A thick (sheet resistance of 1 Ω/sq) indium tin oxide (ITO) coating was deposited on the top surface of the silicon to form the second conducting plate in the waveguide while allowing optical access for the pump light. The NIR pump beam is spatially patterned using a two dimensional SLM, and the intensity profile of

the pump beam on the sample is measured in-situ by splitting a fraction of the beam before illumination and casting the image onto a CMOS array. The SLM used is a commercial product from Holoeye with a 1920×1080 pixel array (8 μm pixel pitch) each providing 256 phase levels and a 2π maximum phase shift. The SLM and imaging optics define structures with a spatial resolution of approximately 40 μm, much smaller than THz wavelengths inside silicon (100 μm). The 1028 nm pump pulse wavelength is chosen close to the indirect band gap of silicon such that the optical penetration depth (≈ 200 μm) is larger than the waveguide thickness, creating a uniform excitation through the thickness of the silicon slab. The resultant charge carrier density profile created by the patterned pump distribution locally modulates the complex-valued refractive index inside the waveguide (see Fig. 6.1(b)). The subsequent space-to-time mapping that occurs upon THz pulse reflection is the key to the functionality of the device. A silicon beamsplitter introduced before the waveguide at 45° (not shown here) redirects the reflected THz pulse for electro-optic sampling detection inside a GaP crystal.

6.5 Results and discussions

The broadband phase ϕ of the THz pulse can be shifted easily by multiples of π by reflection off an even or odd number of conducting interfaces within the waveguide. We can demonstrate this phase flipping capability by retro-reflecting the THz pulse off a single or a pair of photoexcited

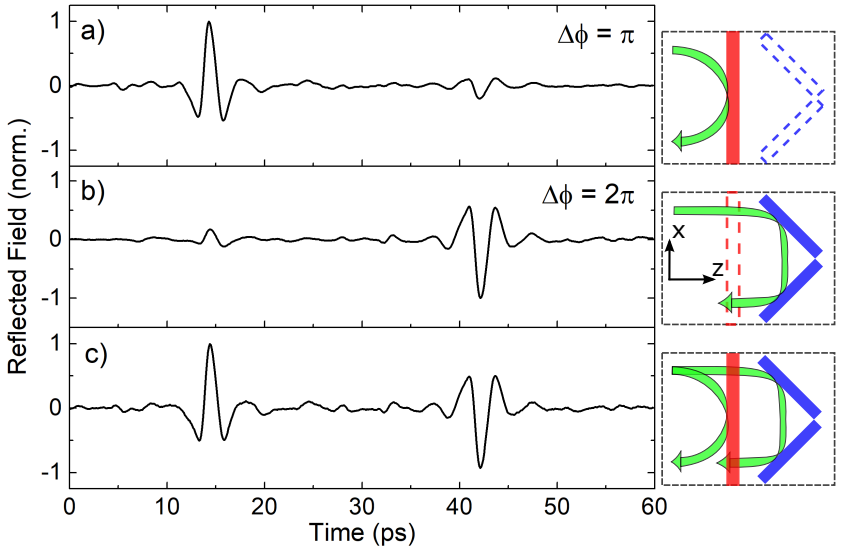

FIGURE 6.2: Reflections of an incident single-cycle THz pulse off dielectric-metal interfaces with associated diagrams. (a) π phase shift and (b) 2π shift generated by reflections off one and two dielectric-metal interfaces, respectively. (c) π and 2π phase shifts induced by the simultaneous presence of all pump-induced metallic reflectors.

lines in the silicon. Figure 6.2 shows the THz reflection from a structure which holds the possibility of either odd (Region I, red) or even (Region II, blue) reflective surfaces, combining a single line excitation and two interfaces at 45° and −45°. The interfaces of these pump-induced reflectors are patterned by a lithographically-defined gold shadow mask deposited atop the ITO layer, shaping the transmitted pump pulses and ensuring a sharp conductive interface and optimal reflection. The SLM is then used to direct light to the two reflectors, and can tune the individual line reflectance. The Drude optical conductivity of injected photocarriers in silicon is purely real and flat to a good approximation over the entire 0.2 - 1 THz bandwidth of the pulse and so the dispersion of the carriers can be neglected. The excited regions are 20 μm in width, and their conductivity is adjustable via pump power tuning over each section. Figure 6.2(a) shows the reflected pulse when 40% of the 120 μJ NIR pulse is used to create Region I, a normal incident reflection off a single surface. With a single interface, we achieve a peak electric-field reflection coefficient of 43% and 19% is reached when both regions are photoexcited. Note, some light leakage in the dark areas defined by the SLM results in the small amount of reflection observed at 42 ps and 14 ps in the $\Delta\phi = \pi$ and $\Delta\phi = 2\pi$ data sets, respectively. When the pump is switched to illuminate only Region II, in Fig. 6.2(b), the pulse is time-shifted due to the extra path length travelled within the waveguide but now the phase is flipped by 2π. If, however, both regions are illuminated with Region I acting as a partial reflector, a phase flipped pair of pulses is received at the detector as shown in Fig. 6.2(c).

Reflection from a distributed interface allows the possibility of broadband phase manipulation and can be used to control the CEP of a pulse [16]. Figures 6.3(a)-6.3(c) show THz pulses reflected off three different charge carrier distributions, each with a carrier-envelope phase shift $\Delta\phi = -\pi/2$, 0 and $+\pi/2$, respectively. The pump intensity profiles giving rise to these charge carrier distributions are defined by the SLM and the measured profiles are shown in the adjacent graphs. Taking the intensity profile of Fig. 6.3(a) as an example, one can think of this carrier distribution as two separate regions. The first, spanning from 0.1 to 0.3 mm, acts as a phase delay for the THz pulse as it passes through the region twice with minimal losses; the second, a peak at 0.37 mm, redirects the pulse as a mirror. An analytical estimate can capture the main contributions to the phase change in the dc limit of the Drude conductivity, where the angular frequency and the scattering time product $\omega\tau \gg 1$, assuming a constant real conductivity σ_1 of length d. This is appropriate for silicon in the range of frequencies investigated as $\tau \sim 50$ fs at room temperature for carrier density on the order of 10^{16} cm^{-3} [37]. In the first, low photoconductivity region, the change in CEP phase is approximately $\Delta\phi_{CEP} = \frac{d}{2c_0}\sqrt{\frac{\sigma_1\omega}{\epsilon_0}}$,

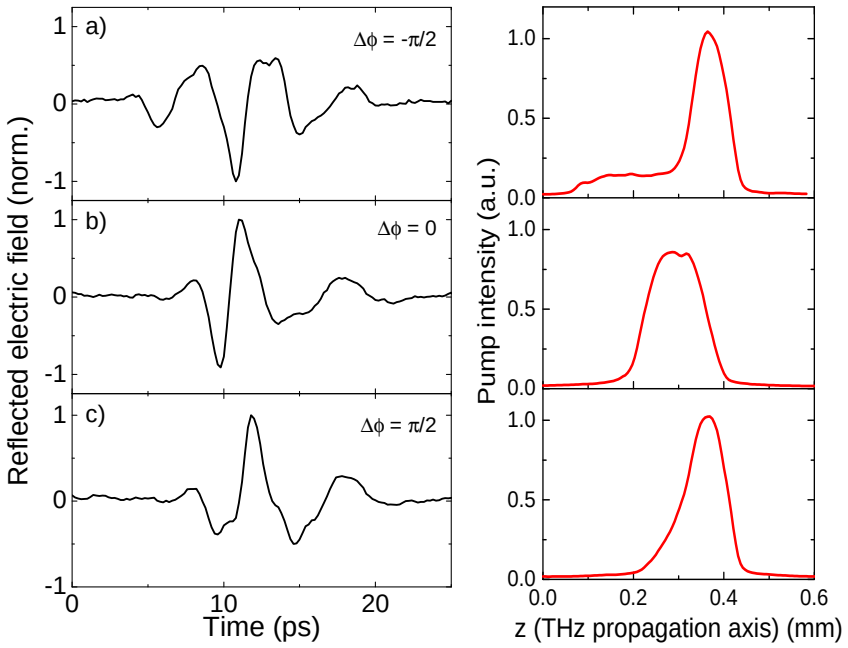

FIGURE 6.3: Imparting broadband $\pm\pi/2$ phase changes to an incident THz pulse using engineered photoconductive reflective interfaces within the waveguide. The data sets show the reflected THz signal as well as the pump intensity profile of the single line generated by the SLM and recorded by the CMOS camera. (a) $-\pi/2$ phase flip, (b) 0 phase flip, and (c) $+\pi/2$ phase flip along side the intensity profile employed.

where σ_1 is the real part of the conductivity, ϵ_0 is the vacuum permittivity and c_0 is the speed of light in vacuum, respectively. The slowly-varying square root dependence on THz frequency serves to introduce a relatively flat phase shift across the pulse; continuously tunable through the thickness of the medium traversed. Finite-difference time-domain (FDTD) simulations performed using a software developed by Larsen et al. [38] provided the intensity profiles required to achieve the desired phase modulation, however minor fine-tuning is performed in situ to achieve the desired pulse shape. We note that given the reconfigurable nature of this phase shaping method it could easily be implemented with a genetic algorithm for pulse shape optimization.

The ability to arbitrarily control the chirp of a pulse is also valuable for control experiments such as vibrational ladder climbing in a molecular system [39]. For a first demonstration, we designed a shadow mask with 20 μm wide lines with a pitch of $\Delta z = 90 \times 0.98^n$ μm, where n is an integer indexing lines in the array. By using a mask, we sacrifice the reconfigurability of the device for better contrast and smaller details in the photoinjected structure, thus reaching higher resonant frequencies. By illuminating the shadow mask with a Gaussian intensity profile, the reflected THz pulse becomes positively chirped as seen in Fig. 6.4(a). Due to the distributed nature of the reflector, the peak electric field reflectivity demonstrated here is kept at 2.3% per

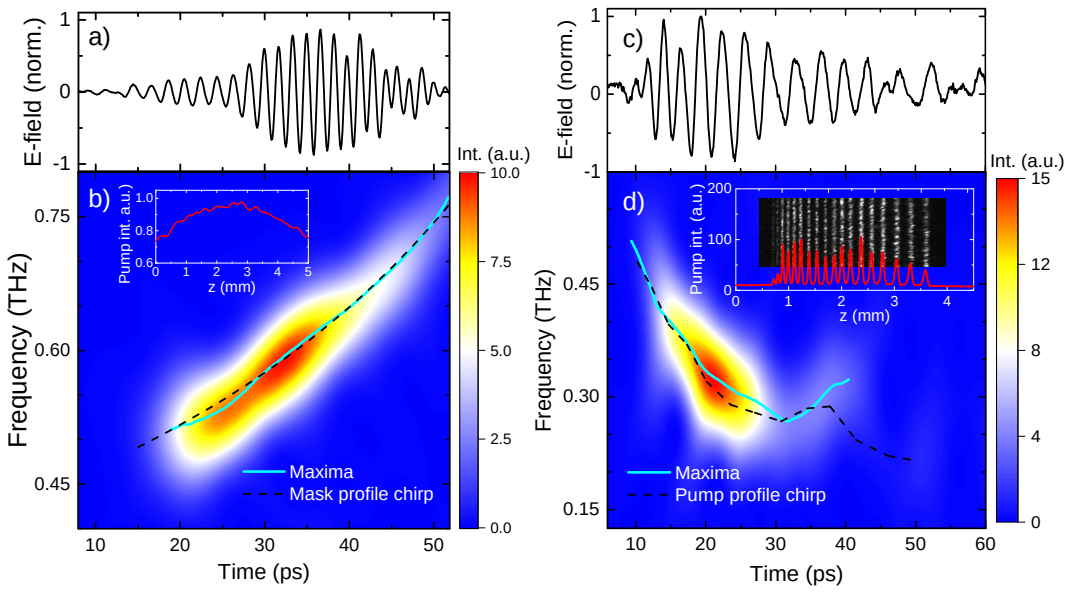

FIGURE 6.4: Positively chirped THz electric field (a) and associated STFT intensity (b) for a shadow-masked sample pumped with 100 μJ pump energy. Negatively chirped THz electric field (c) and associated STFT intensity (d). The pump-intensity profile generated using the SLM and captured by the CMOS array is shown in the insets (b and d). The cyan solid lines (b and d) shows the position of the intensity maxima and the black dashed curve the maxima position predicted from the mask design (b) or pump intensity profile (d).

cycle. A short-time Fourier transform (STFT) of the waveform, presented in Fig. 6.4(b), shows the instantaneous frequency as a function of time increasing from 0.47 THz to 0.75 THz with an average chirp of 8 GHz/ps. The inset shows the pump intensity profile parallel to the THz propagation axis as recorded by the camera. The cyan line follows the position of the intensity maxima of the STFT data and shows excellent agreement with the predicted instantaneous frequency $\nu(t)$ (black dashed curve). From the mask design (Δz), we calculate $\nu(t) = c/2n_{Si}\Delta z$ where $n_{Si} = 3.42$ is the refractive index of silicon.

Negative chirped THz pulses are as easily generated as positive. In this case, we present a maskless implementation using only the SLM to shape the carrier distribution within the waveguide. Operation in this manner is currently limited to chirped frequencies below 0.45 THz due to the pixel size of the SLM and imaging optics used, however the waveforms are completely reconfigurable. Presented in Fig. 6.4(c), the chirped waveform shows a clear increase in cycle period as a function of time. The STFT performed on this data is shown in Fig. 6.4(d), explicitly showing a negative chirp of -11 GHz/ps on average between 10 and 30 ps over a 220 GHz bandwidth. The inset shows the pump intensity profile achieved using the SLM overlaid with the image recorded by the camera. The STFT maxima (solid cyan curve) shows excellent agreement with the expected instantaneous frequency (dashed black curve), calculated directly

from the recorded the pump intensity profile. From the pump intensity profile design, the chirp can be reversed from negative to positive within the same pulse as it does here at 30 ps. This feature is intentionally created by a region near 2 mm (see inset of Fig. 6.4(d)) where the pump induced features are slightly closer together, and this reversal is very well reproduced by the experimentally observed waveform.

6.6 Conclusion

We have demonstrated CEP control over broadband THz pulses using spatially engineered photoinjected reflectors inside a silicon-filled PPWG. Odd or even integer multiples of π phase flips are demonstrated using a single or a pair of pump-induced reflective interfaces, respectively. Broadband tuning of THz pulse phase over $\pm\pi/2$ increments was also demonstrated by photoinjection of low-conductivity phase delay volumes adjacent to the photoinduced reflectors. In addition, arbitrarily chirped THz waveforms were demonstrated in the same platform, both positive and negative, showing 8 and -11 GHz/ps chirp between 0.25 and 0.75 THz. We believe this device will be a great asset for THz dispersion control, wireless communication, and spectroscopy of molecular and solid state systems.

6.7 Funding

The authors gratefully acknowledge funding from the Natural Sciences and Engineering Research Council of Canada (NSERC) and Fonds de Recherche du Québec-Nature et Technologies (FRQNT).

6.8 Disclosures

The authors declare that there are no conflicts of interest related to this article.

References

[1] M. C. Nuss, D. H. Auston, and F. Capasso. "Direct subpicosecond measurement of carrier mobility of photoexcited electrons in gallium-arsenide". In: *Physical Review Letters* 58.22 (1987), pp. 2355–2358.

[2] M. Vanexter and D. R. Grischkowsky. "Characterization of an optoelectronic terahertz beam system". In: *Ieee Transactions on Microwave Theory and Techniques* 38.11 (1990), pp. 1684–1691.

[3] M. C. Hoffmann, J. Hebling, H. Y. Hwang, K. L. Yeh, and K. A. Nelson. "Impact Ionization in InSb studied by THz-Pump-THz-probe spectroscopy". In: *Ultrafast Phenomena Xvi* 92 (2009), pp. 666–668.

[4] K. Kawase, Y. Ogawa, Y. Watanabe, and H. Inoue. "Non-destructive terahertz imaging of illicit drugs using spectral fingerprints". In: *Optics Express* 11.20 (2003), pp. 2549–2554.

[5] S. J. Oh et al. "Molecular imaging with terahertz waves". In: *Optics Express* 19.5 (2011), pp. 4009–4016.

[6] A. G. Markelz, A. Roitberg, and E. J. Heilweil. "Pulsed terahertz spectroscopy of DNA, bovine serum albumin and collagen between 0.1 and 2.0 THz". In: *Chemical Physics Letters* 320.1-2 (2000), pp. 42–48.

[7] L. V. Titova et al. "Intense THz pulses down-regulate genes associated with skin cancer and psoriasis: a new therapeutic avenue?" In: *Scientific Reports* 3 (2013).

[8] W. Kuehn, K. Reimann, M. Woerner, and T. Elsaesser. "Phase-resolved two-dimensional spectroscopy based on collinear n-wave mixing in the ultrafast time domain". In: *Journal of Chemical Physics* 130.16 (2009).

[9] K. L. Yeh, M. C. Hoffmann, J. Hebling, and K. A. Nelson. "Generation of 10 μJ ultrashort terahertz pulses by optical rectification". In: *Applied Physics Letters* 90.17 (2007).

[10] H. Hirori, A. Doi, F. Blanchard, and K. Tanaka. "Single-cycle terahertz pulses with amplitudes exceeding 1 MV/cm generated by optical rectification in $LiNbO_3$". In: *Applied Physics Letters* 98.9 (2011).

[11] F. Blanchard et al. "Effect of extreme pump pulse reshaping on intense terahertz emission in lithium niobate at multimilliJoule pump energies". In: *Optics Letters* 39.15 (2014), pp. 4333–4336.

[12] A. Pashkin, A. Sell, T. Kampfrath, and R. Huber. "Electric and magnetic terahertz nonlinearities resolved on the sub-cycle scale". In: *New Journal of Physics* 15 (2013).

[13] T. Kampfrath, K. Tanaka, and K. A. Nelson. "Resonant and nonresonant control over matter and light by intense terahertz transients". In: *Nature Photonics* 7.9 (2013), pp. 680–690.

[14] P. F. Tian, D. Keusters, Y. Suzaki, and W. S. Warren. "Femtosecond phase-coherent two-dimensional spectroscopy". In: *Science* 300.5625 (2003), pp. 1553–1555.

[15] J. Ahn, A. V. Efimov, R. D. Averitt, and A. J. Taylor. "Terahertz waveform synthesis via optical rectification of shaped ultrafast laser pulses". In: *Opt. Express* 11 (2003), pp. 2486–2496.

[16] M. V. Arkhipov et al. "Generation of unipolar half-cycle pulses via unusual reflection of a single-cycle pulse from an optically thin metallic or dielectric layer". In: *Optics Letters* 42.11 (2017), pp. 2189–2192.

[17] T. L. Cocker et al. "An ultrafast terahertz scanning tunnelling microscope". In: *Nature Photonics* 7.8 (2013), pp. 620–625.

[18] K. Yoshioka et al. "Real-space coherent manipulation of electrons in a single tunnel junction by single-cycle terahertz electric fields". In: *Nature Photonics* 10.12 (2016), pp. 762–765.

[19] T. L. Cocker, D. Peller, P. Yu, J. Repp, and R. Huber. "Tracking the ultrafast motion of a single molecule by femtosecond orbital imaging". In: *Nature* 539.7628 (2016), pp. 263–267.

[20] V. Jelic et al. "Ultrafast terahertz control of extreme tunnel currents through single atoms on a silicon surface". In: *Nature Physics* 13.6 (2017), pp. 591–598.

[21] G. Herink, L. Wimmer, and C. Ropers. "Field emission at terahertz frequencies: AC-tunneling and ultrafast carrier dynamics". In: *New Journal of Physics* 16 (2014).

[22] J. D. Zhang et al. "Terahertz radiation-induced sub-cycle field electron emission across a split-gap dipole antenna". In: *Applied Physics Letters* 107.23 (2015).

[23] S. Li and R. R. Jones. "High-energy electron emission from metallic nano-tips driven by intense single-cycle terahertz pulses". In: *Nature Communications* 7 (2016).

[24] R. Mendis, A. Nag, F. Chen, and D. M. Mittleman. "A Tunable Universal THz Filter using Artificial Dielectrics". In: *35th International Conference on Infrared, Millimeter, and Terahertz Waves (Irmmw-Thz 2010)* (2010).

[25] Y. Kawada, T. Yasuda, and H. Takahashi. "Carrier envelope phase shifter for broadband terahertz pulses". In: *Optics Letters* 41.5 (2016), pp. 986–989.

[26] A. Sell, R. Scheu, A. Leitenstorfer, and R. Huber. "Field-resolved detection of phase-locked infrared transients from a compact Er:fiber system tunable between 55 and 107 THz". In: *Applied Physics Letters* 93.25 (2008).

[27] K. Kawase, J. Shikata, and H. Ito. "Terahertz wave parametric source". In: *J. Phys. D Appl. Phys.* 35 (2002), R1–R14.

[28] Z. Chen, X. B. Zhou, C. A. Werley, and K. A. Nelson. "Generation of high power tunable multicycle teraherz pulses". In: *Applied Physics Letters* 99.7 (2011).

[29] Sen-Cheng Zhong et al. "Dual-mode tunable terahertz generation in lithium niobate driven by spatially shaped femtosecond laser". In: *Optics Express* 25.15 (2017), pp. 17066–17075.

[30] L. Mahler et al. "High-performance operation of single-mode terahertz quantum cascade lasers with metallic gratings - art. no. 1181101". In: *Applied Physics Letters* 87.18 (2005).

[31] Q. F. Xu, P. Dong, and M. Lipson. "Breaking the delay-bandwidth limit in a photonic structure". In: *Nature Physics* 3.6 (2007), pp. 406–410.

[32] Lauren Gingras and David G. Cooke. "Direct temporal shaping of terahertz light pulses". In: *Optica* 4.11 (2017), pp. 1416–1420.

[33] D. G. Cooke and P. U. Jepsen. "Optical modulation of terahertz pulses in a parallel plate waveguide". In: *Optics Express* 16.19 (2008), pp. 15123–15129.

[34] D. G. Cooke and P. U. Jepsen. "Time-resolved THz spectroscopy in a parallel plate waveguide". In: *Physica Status Solidi a-Applications and Materials Science* 206.5 (2009), pp. 997–1000.

[35] L. Gingras, M. Georgin, and D. G. Cooke. "Optically induced mode coupling and interference in a terahertz parallel plate waveguide". In: *Optics Letters* 39.7 (2014), pp. 1807–1810.

[36] Lauren Gingras, François Blanchard, Marcel Georgin, and David G. Cooke. "Dynamic creation of a light-induced terahertz guided-wave resonator". In: *Optics Express* 24.3 (2016), pp. 2496–2504.

[37] F. A. Hegmann and K. P. H. Lui. "Optical pump - terahertz probe investigation of carrier relaxation in radiation-damaged silicon-on-sapphire". In: *Ultrafast Phenomena in Semiconductors Vi* 4643 (2002), pp. 31–41.

[38] C. Larsen, D. G. Cooke, and P. U. Jepsen. "Finite-difference time-domain analysis of time-resolved terahertz spectroscopy experiments". In: *J. Opt. Soc. Am. B* 28 (2011), pp. 1308–1316.

[39] N. A. Gershenfeld and I. L. Chuang. "Bulk spin-resonance quantum computation". In: *Science* 275 (1997), pp. 350–356.

Chapter 7

Further experiments

In the sections that follow we will discuss a few applications suited for the platform we have built in the course of this project. This list is by no means exhaustive and focuses on underlying the applications that we wish to pursue and also for which we already have collected preliminary data. As this is all ongoing research we present the relevant theory only in a brief fashion; the recorded experimental data sets presented are by no means comprehensive and we wish to expand on the experimental parameters that might be relevant or interesting to investigate in future studies. We would like to note that most of these measurements were performed during the course of other experiments mainly as exploratory proof-of-concept projects in the laboratory spaces of the University of Ottawa. We therefore have performed the necessary calibrations and verifications to ensure the validity of the experimental data.

7.1 Time-to-space mapping

One of the first concepts that is interesting to point out is that, as was pointed out earlier, these experiments rely on the concept of space-to-time mapping where photoinjected lines form a pattern in space that is directly imprinted on the time-domain data recorded through the electric field waveform. What is also interesting to note is that this concept can also be extended to perform time-to-space mapping, in which by looking at the time-resolved information collected one can infer information about the spatial distribution of the electric field amplitude, for example.

7.1.1 Echelons and THz wavefront imaging

In this experiment, we define a set of 4 small mirrors that are overlaid in a step-like arrangement. A pictorial depiction can be seen in the insets of Fig. 7.1 where an incident Gaussian intensity wavefront is partially reflected by 4 small mirrors. By separating the mirrors along the x-axis, each individually provides information about the intensity of the pulse at its position.

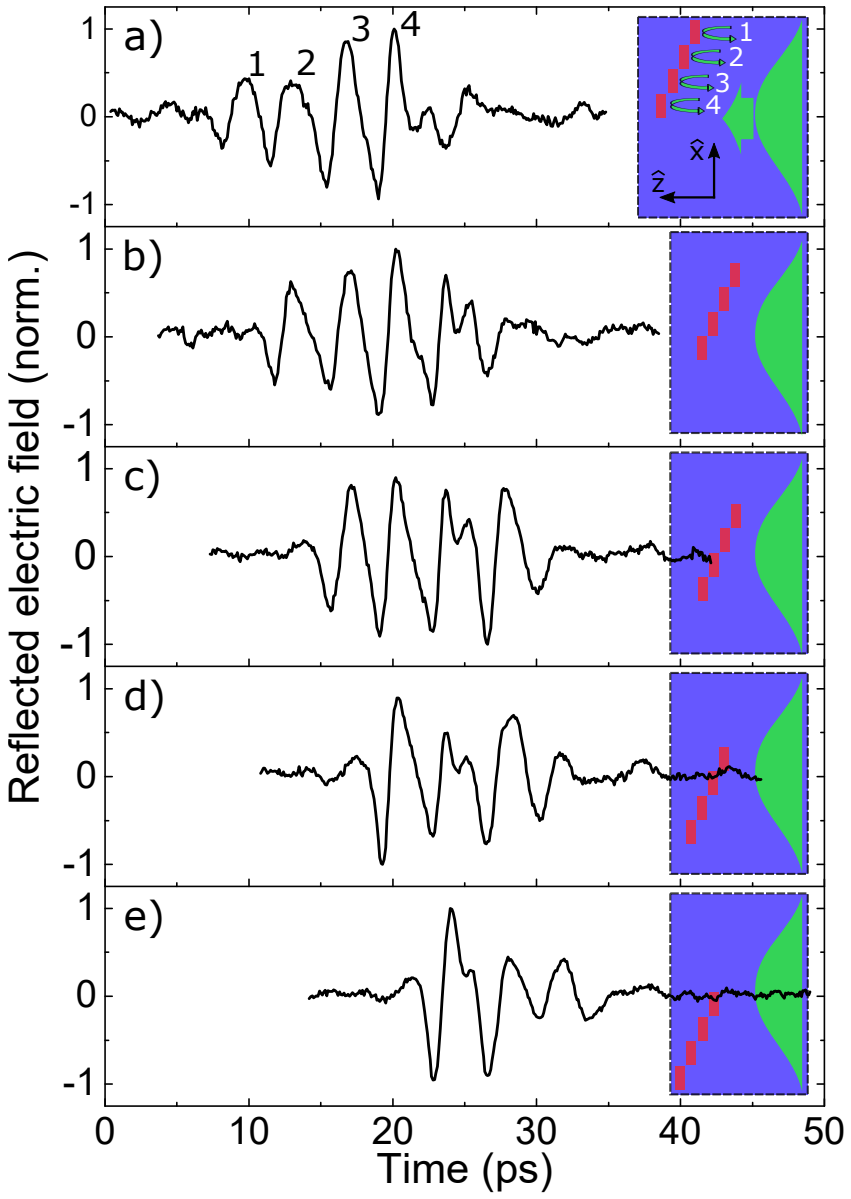

FIGURE 7.1: Time-to-space mapping of the THz field amplitude spatial distribution. a) Shows 4 peaks separated in time labelled 1-4 alongside a schematic representation of 4 small spatially separated mirrors causing the reflection. The red lines in the inset depict the photoinjected mirrors whilst the green shape shows the Gaussian spatial distribution of the THz field amplitude inside the waveguide. Subfigures b)-e) show the mapping of the field amplitude as the mirrors are moved by 1 vertical pitch between each plot. We note that there are redundant peaks between each subsequent measurement.

The separation along the z-axis is directly correlated to the time-difference in the arrival of the pulses at the detector, as illustrated by the labels (1-4) on the reflectors and associated peaks. By shifting the reflectors both in the x and z directions, it is possible to reconstruct the spatial distribution of the wavefront inside the waveguide. By looking at the subfigures a) and e) we can immediately recognize the wings of the Gaussian distribution whilst subfigure c) mirrors the flatter distribution near the Gaussian maximum. The x-axis range scanned here is roughly 8 mm with reflectors of about 1 mm in length defined using the SLM. This ensures minimal scattering of the field upon reflection due to the absence of wavelength-sized features and spans the entirety of the sample in the x-axis. This confirms our former assumption that the experiments were performed with a "soft" focus inside the waveguide (ie. the focus is far from diffraction-limited).

7.2 Two-dimensional photonic crystals

One more interesting aspect of this platform is the possibility to create two-dimensional (2D) photonic crystals out of light-induced pillars inside silicon. As illustrated in previously published work, the 1D structures did not exhibit a photonic gap, or a band where no frequencies are allowed to propagate freely. As we demonstrate here, this is however not the case for two-dimensional structures where periodic boundary conditions can be engineered to prevent certain frequency bands from being allowed within the array of pillars. The structure is created using a shadow mask in order to ensure maximal contrast and smoothness of the pillar edges. The lattice is comprised of a 10×10 array of cylinders (30 μm radius) with a 100 μm center to center distance. The sample is illuminated uniformly and both transmitted and reflected electric field time traces are collected for analysis. The frequency domain data is presented in Fig. 7.2 for both transmission and reflection with pump energies of 15, 72 and 133 μJ. As we know, square array lattices have a few rejection bands, or gaps, in the $\Gamma-$X region for TM modes [193]. Accordingly, if we draw our attention to the reflected spectra which is more evident, we can observe reflection peaks at 0.2, 0.45 and 0.9 THz. Though those peaks are more pronounced for higher intensities we also see the appearance of a broadband reflection due to the increasing metallic nature of the structure. This results in smaller penetration of the THz light into the lattice which results in broadband reflection but also lessens the interference effect. If we look at the transmitted spectrum, we can observe a clear reduction at 0.2 and 0.45 THz though the effect is not as clear as in reflection. It is important to note that the data presented is the differential

transmission. Due to the small dimension of the array, much of the incident THz light collected by the detector was able to pass outside of the photoinjected region. Thus, the differential and reference data sets could not be correlated properly because of a high unmodulated background signal. This could obviously be improved in future experiments simply by defining an array spanning the entire sample in the photolithographic stage of the sample fabrication.

7.2.1 Bandgap structure

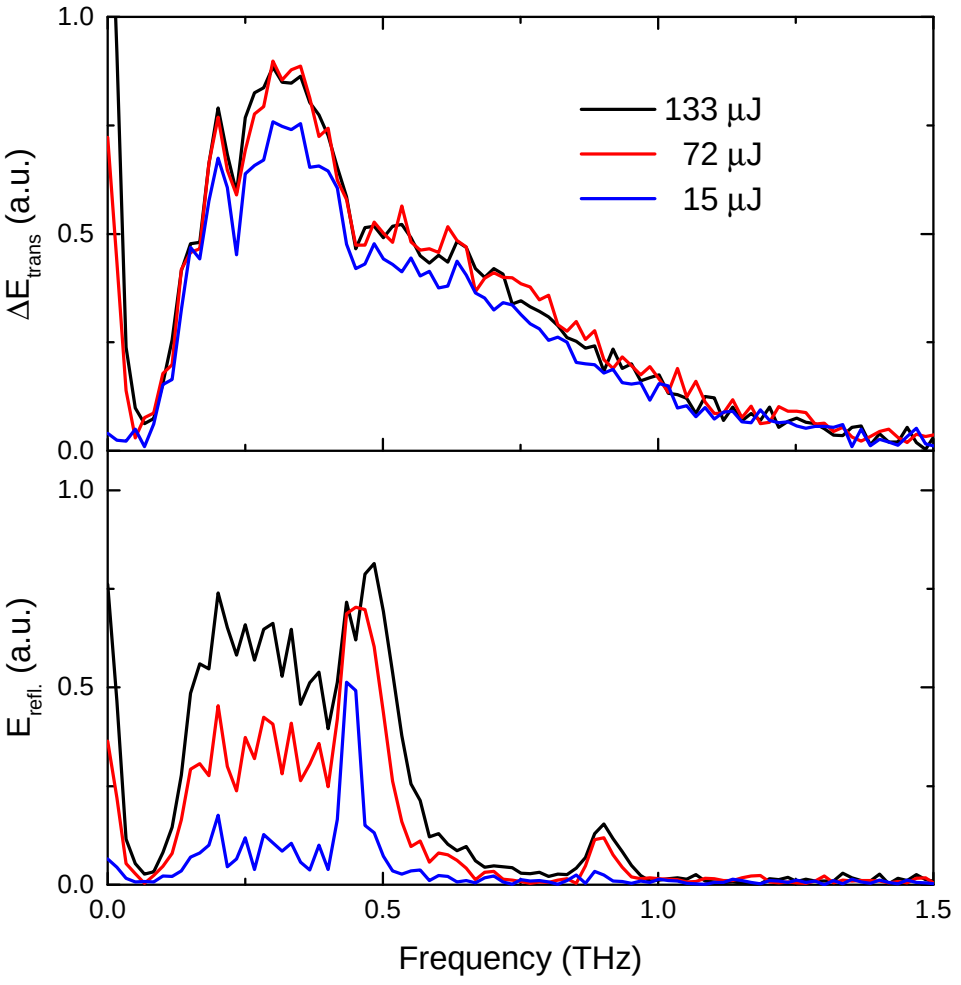

FIGURE 7.2: (top) Transmission of a THz pulse through a 10×10 square array of photoinjected cylinders. The structure has a 100 μm pitch and the columns have a 30 μm radius. The total pump intensity is varied between 90 mW and 800 mW. (bottom) Reflected electric field amplitude for the same structure and parameters.

7.2.2 Future experiments

One of the details that might strike the reader about the previous experiment is that it was performed in the static regime, where no time resolution is provided between the arrival of the pump light and THz light. This is simply because no mechanical translation stage had been implemented in the pump line when these experiments were performed. It might seem like an obvious extension of this work to investigate the dynamics of photonic band creation, and it would be. In future experiments we wish to investigate not only more structures (rectangular, hexagonal, etc.) but also the effects of dynamic creation of photonic gaps in order to probe the adiabatic and hopefully non-adiabatic transitions that occur when the environment of a broadband pulse is modified on ultrafast timescales. Again, it is important to remember that the all-optical nature of the structure and lack of pre-existing folded photonic band structure results in infinite input bandwidth, within the constrained experimentally available bandwidth of course. What this allows if for the possibility of creating gapped structures entirely encompassing a THz pulse on timescales faster than the transit time. Using these methods we hope to investigate the possibility for trapping of broadband signals but also perhaps of subsequent pump-induced releasing. This is of course still in a speculative phase and we have begun investigating these effects using FDTD simulations though major issues have arose leading to non-converging solutions due to dynamic refractive index modulations within the model. Needless to say, this is a very interesting prospect from a fundamental science standpoint and also a work in progress.

7.3 Pulse shaping for molecular control experiments

Perhaps one of the most interesting prospects enabled by arbitrary pulse shaping is the ability to control molecular vibrations instead of just probing their resonances. For example, by tailoring a field on or near resonance, it is conceivable to prepare groups of molecules in a preferred alignment, orientation or to populate their rotational vibrational states in a given order. This is of course an extension of the principle at work behind nuclear magnetic resonance (NMR) spectroscopy, where a series of pulses is applied to probe and prepare samples, typically small molecules, by targeting resonances of the atomic nuclei's local magnetic field. In the THz regime, transitions targeted would be in the few-meV energy range such as the rotational vibration of water molecules.

7.3.1 Resonance and free induction decay

For a proof of concept and quick experiment, we turned to perhaps the most easily available molecule in a laboratory space: H_2O. As every THz spectroscopist knows too well water molecules have a wide array of resonances at THz frequencies. The folded molecule indeed has a very high polarity and is exceedingly abundant in the Earth's atmosphere. This is of course extremely convenient to any living organism but extremely aggravating to lab-dwelling THz spectroscopist as gaseous H_2O is responsible for considerable dispersion and the myriad of dips observed throughout the far infrared spectrum [30]. This of course has been known for a long time now and spectroscopists have figured out clever ways to avoid suffering from these, such as building elaborate enclosures made of plexiglass and garbage bags surrounding the portions of the spectrometer where THz light freely propagates. These enclosures are then purged with dry air or nitrogen in order to remove the excess water molecules.

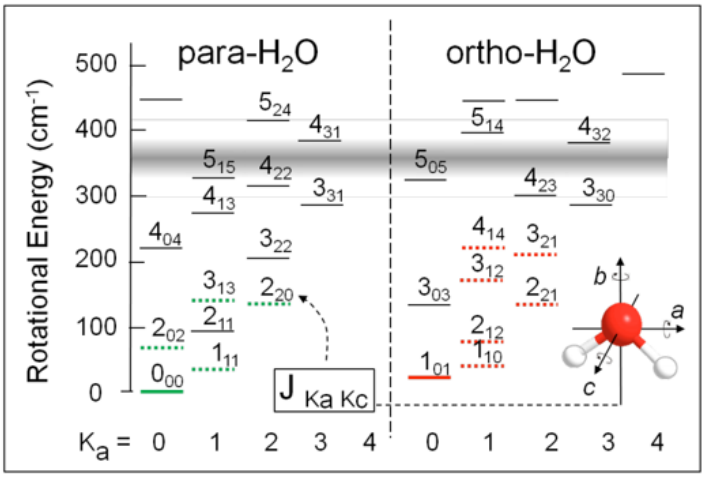

FIGURE 7.3: Rotational energy levels of ortho- and para-water. The ball-stick model indicates the rotation axis a & c for the k-state quantum numbers (K_a & K_c, respectively). This figure was reproduced from Yang et al. [183].

What this experiment focuses on is the resonant excitation of the transition between the 1_{01} and 1_{10} molecular rotations which corresponds to a transition frequency of 556 GHz. These numbers refer to the J, K_a and K_c quantum numbers of the molecular vibrational states, which are shown in Fig. 7.3, which is reproduced from Yang et al. [183]. The 556 GHz transition might be familiar to the reader as it is the lowest order vibrational transition of ortho-water, the expression of H_2O with oppositely aligned hydrogen spins. We note that this is not a transition from the ground state (0_{00}) as the vibrational ground state only exists in the para-water molecule where both hydrogen spins are aligned and k-state sums must be even. By

tailoring a slowly increasing field resonant with the 556 GHz transition and by increasing the number of field cycles we can observe the free induction decay of water molecules in air at 30% relative humidity, as shown in Fig. 7.4. Here, we observe the exponential decay expected from the resonant creation of an excited population of molecular with preferential alignment due to the polarization of the THz electric field.

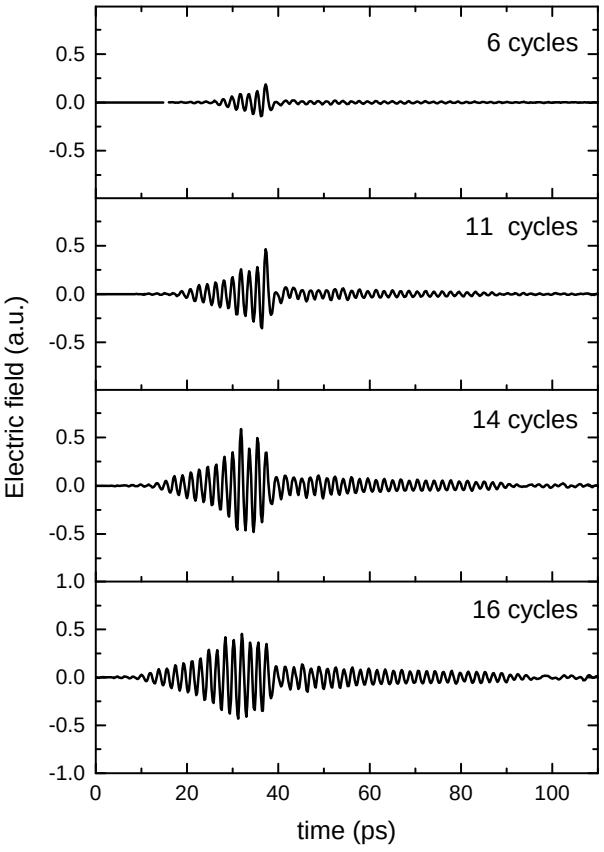

FIGURE 7.4: Electric field time trace of a multi-cycle driving field exhibiting radiative decay of the 556 GHz water rotational molecular transition. The data is presented for increasing number of field cycles, all at 30% relative humidity.

7.3.2 Echo of the 556 GHz H_2O transition

What is remarkable though is that if we simply purge the volume inside the box using nitrogen from a gas cylinder down to 5% relative humidity homogeneous linewidth broadening diminishes due to lessening in intermolecular collision frequency and given a large enough number of cycles and field amplitude we are able to observe an echo of the rotational state. The left side of Fig. 7.4 shows the time traces of the pump used and the echos observed whilst the figures to the right show a blowup of the echo. In this case, the experiment was performed with water vapour in both the collimated and focused section of the sample. For this, it is difficult to evaluate the

number of molecules being probed as there is no defined volume being probed at a precise field value. We believe that the greater contribution originates from the gas volume encompassed by the focus of the sample where field intensities, and thus alignment, are greater.

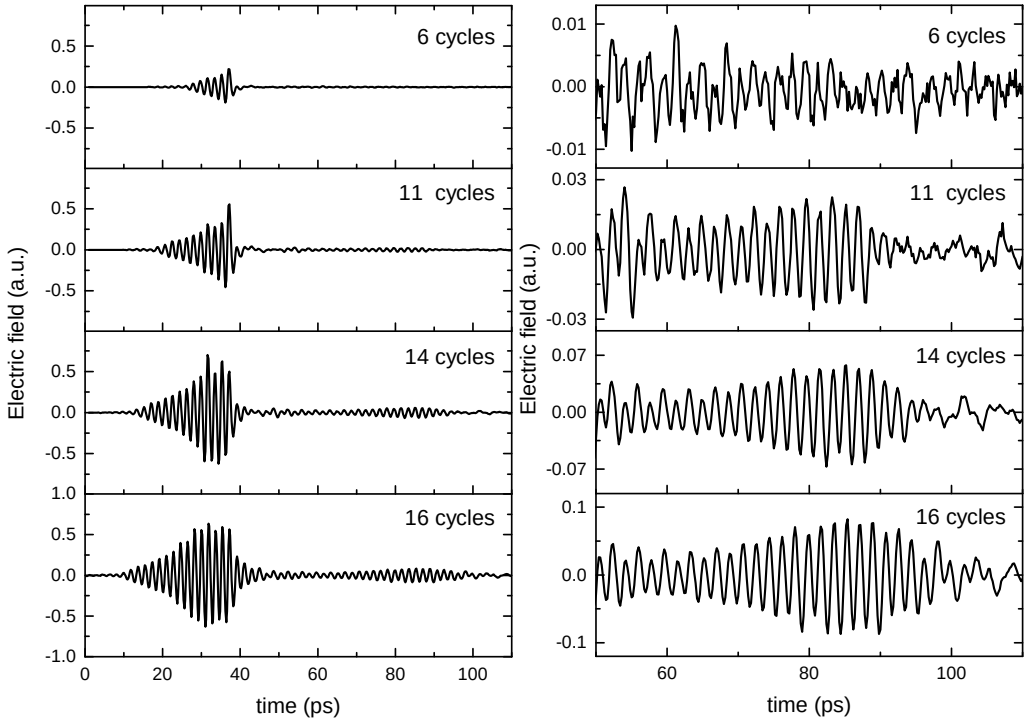

FIGURE 7.5: Electric field time trace of a multi-cycle driving field exhibiting an echo of the 556 GHz water rotational molecular transition. The data is presented for increasing number of field cycles, all at 5% relative humidity. The plots on the right side show enlargements of the full time traces presented on the left in the vicinity of the echo.

By looking at the resonant peak intensity ($E^2(t)$), it is possible to gather information about the nature resonance. Whilst this is still an ongoing investigation and since there are still many experimental unknowns, we show Gaussian fits of the resonances in Fig. 7.6. The main parameters shown here are the linewidth of the echo (FHWM) and the time delay (Δt) between the last driving cycle and the echo peak. We believe these two parameters are linked to how narrowly-defined the two interfering states are and their energy separation, though the nature of those is still uncertain. The presence of a triplet state in ortho-water raises the question of Stark splitting of the resonant levels though this is still speculative and more careful experimental investigation needs to be made before any conclusions can be drawn. What seems to be certain is that no clear change is observed in the echo apart from its amplitude when more cycles are added to the driving field. Since the 556 GHz resonance has a van-Vlek-Weisskopf line

shape which is characterized by a dispersive response that spans much of out incident THz bandwidth further investigations should consider the effects of dispersion on the pump beam. As such, future experiments should investigate the dependence on the humid air volume and propagation distance of the THz pulse in this volume.

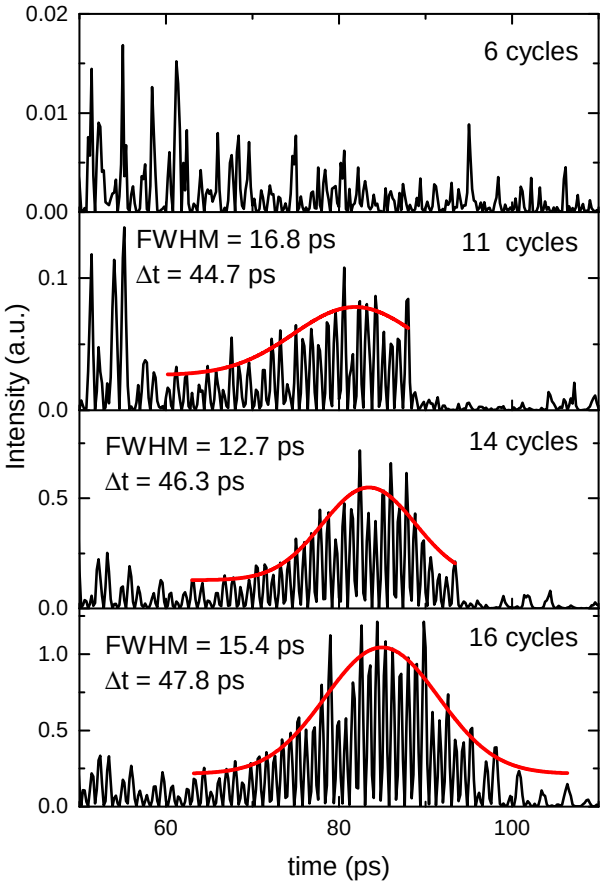

FIGURE 7.6: Intensity ($E^2(t)$) peaks of the rotational echo of the 556 GHz transition in water molecules at 5% relative humidity. The red curves show Gaussian fits to the peak maxima with their FWHM and central time delay (Δt) with respect to the last driving cycle maxima.

7.4 Eyecandy

We would like to conclude by presenting some images that illustrate well the power of the pulse-shaping method discussed in this manuscript. The waveforms fashioned for the following figures have perhaps no scientific value but serve to exemplify just how arbitrarily the envelope of THz fields can be sculpted using this method. Figure 7.7 shows 22 consecutive field cycles with an envelope fashioned to match the structure of the Jacques-Cartier bridge linking Montreal and the south shore of the St-Laurent river. As shown in the backdrop image, the structure has

been recently been fitted with several thousands of LED light structures which are used to bring light shows to the metropolis area. Figure 7.8 shows an even more impressive structure, the Canadian parliament located in Ottawa. The envelope of the 23 field cycles overlap with the building's roof and towers to create what we believe to be the most elaborate THz waveform generated to his day.

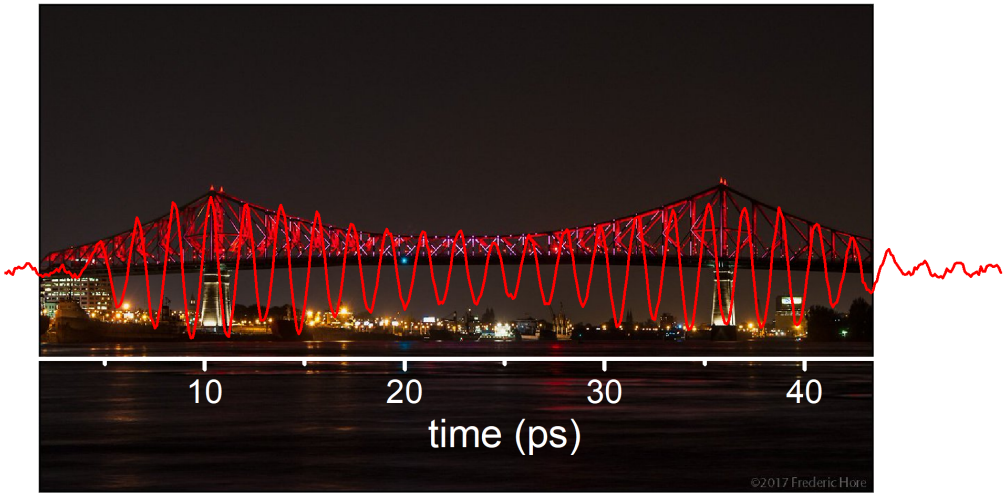

FIGURE 7.7: Time trace of a THz multi-cycle pulse fashioned to overlay with a picture of the Jacques-Cartier bridge joining the island of Montreal and the south shore of the St-Laurent river.

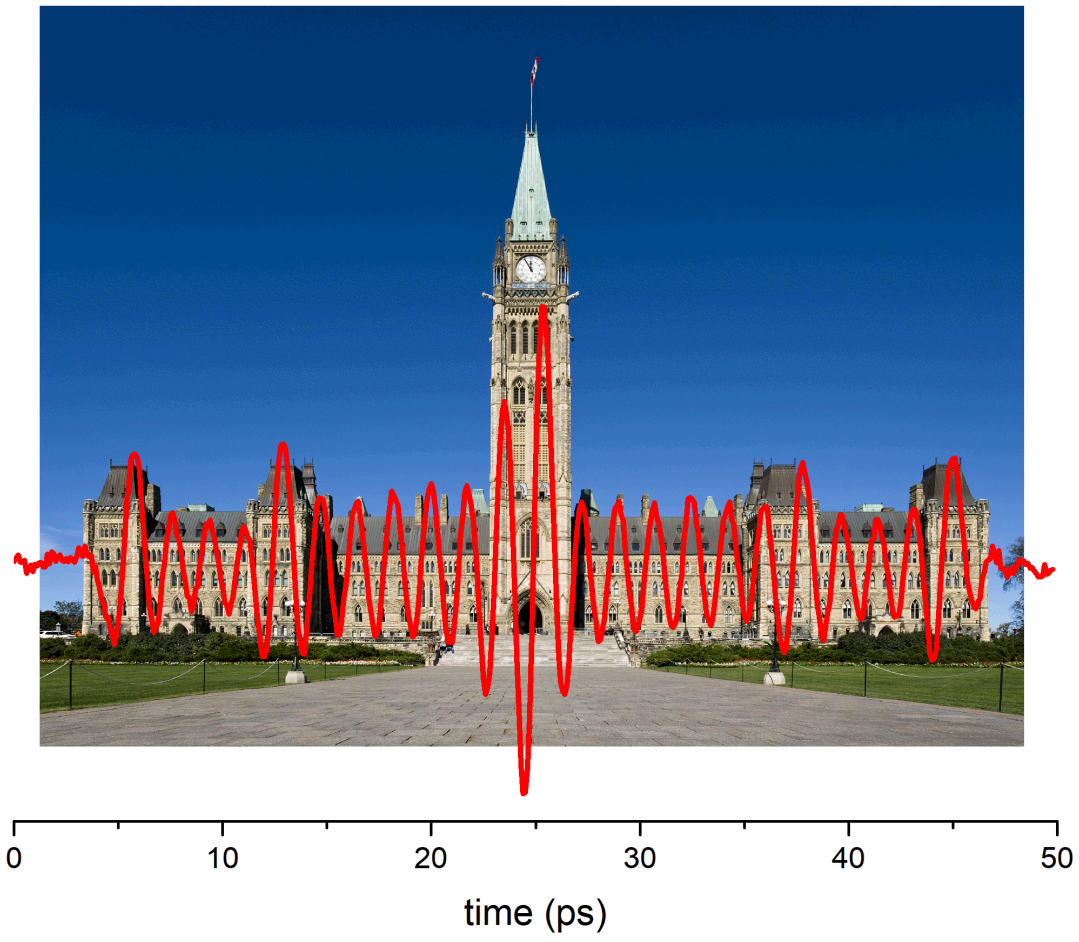

FIGURE 7.8: THz waveform with an envelope engineered to overlap with the Canadian parliament building.

Bibliography - Articles

[1] L. Gingras, M. Georgin, and D. G. Cooke. "Optically induced mode coupling and interference in a terahertz parallel plate waveguide". In: *Optics Letters* 39.7 (2014), pp. 1807–1810.

[2] Lauren Gingras, François Blanchard, Marcel Georgin, and David G. Cooke. "Dynamic creation of a light-induced terahertz guided-wave resonator". In: *Optics Express* 24.3 (2016), pp. 2496–2504.

[3] Lauren Gingras and David G. Cooke. "Direct temporal shaping of terahertz light pulses". In: *Optica* 4.11 (2017), pp. 1416–1420.

[4] Lauren Gingras, Wei Cui, Aidan W. Schiff-Kearn, Jean-Michel Ménard, and David G. Cooke. "Active phase control of terahertz pulses using a dynamic waveguide". In: *Optics Express* 26.11 (2018), pp. 13876–13882.

[5] D. H. Auston. "Picosecond optoelectronic switching and gating in silicon". In: *Applied Physics Letters* 26.3 (1975), pp. 101–103.

[6] G. M. Turner, M. C. Beard, and C. A. Schmuttenmaer. "Carrier localization and cooling in dye-sensitized nanocrystalline titanium dioxide". In: *Journal of Physical Chemistry B* 106.45 (2002), pp. 11716–11719.

[7] Prashanth C. Upadhya et al. "Excitation-density-dependent generation of broadband terahertz radiation in an asymmetrically excited photoconductive antenna". In: *Optics Letters* 32.16 (2007), pp. 2297–2299.

[8] H. J. Bakker, G. C. Cho, H. Kurz, Q. Wu, and X. C. Zhang. "Distortion of terahertz pulses in electro-optic sampling". In: *Journal of the Optical Society of America B-Optical Physics* 15.6 (1998), pp. 1795–1801.

[9] C. Baker et al. "Highly resistive annealed low-temperature-grown InGaAs with sub-500 fs carrier lifetimes". In: *Applied Physics Letters* 85.21 (2004), pp. 4965–4967.

[10] Abul K. Azad et al. "Carrier dynamics in InGaAs with embedded ErAs nanoislands". In: *Applied Physics Letters* 93.12 (2008).

[11] M. Herrmann, M. Tani, M. Watanabe, and K. Sakai. "An electronic read-out circuit for time-domain terahertz imaging with photoconductive antennas". In: *Physics in Medicine and Biology* 47.21 (2002), pp. 3711–3718.

[12] Masaya Nagai, Hiroyuki Yada, Takashi Arikawa, and Koichiro Tanaka. "Terahertz time-domain attenuated total reflection spectroscopy in water and biological solution". In: *International Journal of Infrared and Millimeter Waves* 27.4 (2006), pp. 505–515.

[13] T. Mueller et al. "Ultrafast resonant terahertz response of excitons in semiconductor quantum dots". In: *Physical Review B* 77.3 (2008).

[14] L. Razzari et al. "Nonlinear ultrafast modulation of the optical absorption of intense few-cycle terahertz pulses in n-doped semiconductors". In: *Physical Review B* 79.19 (2009).

[15] K. Kawase, Y. Ogawa, Y. Watanabe, and H. Inoue. "Non-destructive terahertz imaging of illicit drugs using spectral fingerprints". In: *Optics Express* 11.20 (2003), pp. 2549–2554.

[16] J. Y. Lu et al. "Terahertz microchip for illicit drug detection". In: *Ieee Photonics Technology Letters* 18.21-24 (2006), pp. 2254–2256.

[17] M. Kato, S. R. Tripathi, K. Murate, K. Imayama, and K. Kawase. "Non-destructive drug inspection in covering materials using a terahertz spectral imaging system with injection-seeded terahertz parametric generation and detection". In: *Optics Express* 24.6 (2016), pp. 6425–6432.

[18] M. C. Kemp, P. F. Taday, B. E. Cole, J. A. Cluff, A. J. Fitzgerald, and W. R. Tribe. "Security applications of terahertz technology". In: *Terahertz for Military and Security Applications* 5070 (2003), pp. 44–52.

[19] M. C. Kemp. "Explosives Detection by Terahertz Spectroscopy-A Bridge Too Far?" In: *Ieee Transactions on Terahertz Science and Technology* 1.1 (2011), pp. 282–292.

[20] A. C. Warren et al. "Arsenic precipitates and the semi-insulating properties of GaAs buffer layers grown by low-temperature molecular-beam epitaxy". In: *Applied Physics Letters* 57.13 (1990), pp. 1331–1333.

[21] M. C. Wanke, O. Lehmann, K. Muller, Q. Z. Wen, and M. Stuke. "Laser rapid prototyping of photonic band-gap microstructures". In: *Science* 275.5304 (1997), pp. 1284–1286.

[22] S. E. Whitmire, D. Wolpert, A. G. Markelz, J. R. Hillebrecht, J. Galan, and R. R. Birge. "Protein flexibility and conformational state: A comparison of collective vibrational modes of wild-type and D96N bacteriorhodopsin". In: *Biophysical Journal* 85.2 (2003), pp. 1269–1277.

[23] S. Wietzke, C. Joerdens, N. Krumbholz, B. Baudrit, M. Bastian, and M. Koch. "Terahertz imaging: a new non-destructive technique for the quality control of plastic weld joints". In: *Journal of the European Optical Society-Rapid Publications* 2 (2007).

[24] R. Knipper et al. "THz absorption in fabric and its impact on body fcanning for security application". In: *Ieee Transactions on Terahertz Science and Technology* 5.6 (2015), pp. 999–1004.

[25] M. C. Beard and C. A. Schmuttenmaer. "Using the finite-difference time-domain pulse propagation method to simulate time-resolved THz experiments". In: *Journal of Chemical Physics* 114.7 (2001), pp. 2903–2909.

[26] M. C. Beard, G. M. Turner, and C. A. Schmuttenmaer. "Subpicosecond carrier dynamics in low-temperature grown GaAs as measured by time-resolved terahertz spectroscopy". In: *Journal of Applied Physics* 90.12 (2001), pp. 5915–5923.

[27] M. C. Beard, G. M. Turner, and C. A. Schmuttenmaer. "Measuring intramolecular charge transfer via coherent generation of THz radiation". In: *Journal of Physical Chemistry A* 106.6 (2002), pp. 878–883.

[28] L. Thrane, R. H. Jacobsen, P. U. Jepsen, and S. R. Keiding. "THz reflection spectroscopy of liquid water". In: *Chemical Physics Letters* 240.4 (1995), pp. 330–333.

[29] D. Turchinovich, A. Kammoun, P. Knobloch, T. Dobbertin, and M. Koch. "Flexible all-plastic mirrors for the THz range". In: *Applied Physics a-Materials Science & Processing* 74.2 (2002), pp. 291–293.

[30] M. Vanexter, C. Fattinger, and D. Grischkowsky. "Terahertz time-domain spectroscopy of water-vapor". In: *Optics Letters* 14.20 (1989), pp. 1128–1130.

[31] R. A. Cheville and D. Grischkowsky. "Far-infrared terahertz time-domain spectroscopy of flames". In: *Optics Letters* 20.15 (1995), pp. 1646–1648.

[32] B. E. Cole, J. B. Williams, B. T. King, M. S. Sherwin, and C. R. Stanley. "Coherent manipulation of semiconductor quantum bits with terahertz radiation". In: *Nature* 410.6824 (2001), pp. 60–63.

[33] M. Schall, M. Walther, and P. U. Jepsen. "Fundamental and second-order phonon processes in CdTe and ZnTe". In: *Physical Review B* 64.9 (2001).

[34] R. Huber, F. Tauser, A. Brodschelm, M. Bichler, G. Abstreiter, and A. Leitenstorfer. "How many-particle interactions develop after ultrafast excitation of an electron-hole plasma". In: *Nature* 414.6861 (2001), pp. 286–289.

[35] I. H. Libon et al. "An optically controllable terahertz filter". In: *Applied Physics Letters* 76.20 (2000), pp. 2821–2823.

[36] S. Chatterjee et al. "THz measurements of the optical response in a two-dimensional electron gas". In: *Physica Status Solidi C: Current Topics in Solid State Physics, Vol 6, No 2* 6.2 (2009), pp. 453–456.

[37] J. Hebling, G. Almasi, I. Z. Kozma, and J. Kuhl. "Velocity matching by pulse front tilting for large-area THz-pulse generation". In: *Optics Express* 10.21 (2002), pp. 1161–1166.

[38] K. L. Yeh, M. C. Hoffmann, J. Hebling, and K. A. Nelson. "Generation of 10 μJ ultrashort terahertz pulses by optical rectification". In: *Applied Physics Letters* 90.17 (2007).

[39] A. Sell, R. Scheu, A. Leitenstorfer, and R. Huber. "Field-resolved detection of phase-locked infrared transients from a compact Er:fiber system tunable between 55 and 107 THz". In: *Applied Physics Letters* 93.25 (2008).

[40] N. Karpowicz et al. "Coherent heterodyne time-domain spectrometry covering the entire 'terahertz gap' (vol 92, art no. 011131, 2008)". In: *Applied Physics Letters* 92.15 (2008).

[41] C. P. Hauri, C. Ruchert, C. Vicario, and F. Ardana. "Strong-field single-cycle THz pulses generated in an organic crystal". In: *Applied Physics Letters* 99.16 (2011).

[42] T. Seifert et al. "Efficient metallic spintronic emitters of ultrabroadband terahertz radiation". In: *Nature Photonics* 10.7 (2016), pp. 483–488.

[43] P. Rodin, U. Ebert, W. Hundsdorfer, and I. Grekhov. "Tunneling-assisted impact ionization fronts in semiconductors". In: *Journal of Applied Physics* 92.2 (2002), pp. 958–964.

[44] P. Gaal, K. Reimann, M. Woerner, T. Elsaesser, R. Hey, and K. H. Ploog. "Nonlinear terahertz response of n-type GaAs". In: *Physical Review Letters* 96.18 (2006).

[45] W. Kuehn, P. Gaal, K. Reimann, M. Woerner, T. Elsaesser, and R. Hey. "Terahertz-induced interband tunneling of electrons in GaAs". In: *Physical Review B* 82.7 (2010).

[46] M. M. Glazov and S. D. Ganichev. "High frequency electric field induced nonlinear effects in graphene". In: *Physics Reports-Review Section of Physics Letters* 535.3 (2014), pp. 101–138.

[47] H. T. Chen, R. Kersting, and G. C. Cho. "Terahertz imaging with nanometer resolution". In: *Applied Physics Letters* 83.15 (2003), pp. 3009–3011.

[48] T. L. Cocker et al. "An ultrafast terahertz scanning tunnelling microscope". In: *Nature Photonics* 7.8 (2013), pp. 620–625.

[49] T. L. Cocker, D. Peller, P. Yu, J. Repp, and R. Huber. "Tracking the ultrafast motion of a single molecule by femtosecond orbital imaging". In: *Nature* 539.7628 (2016), pp. 263–267.

[50] K. Yoshioka et al. "Real-space coherent manipulation of electrons in a single tunnel junction by single-cycle terahertz electric fields". In: *Nature Photonics* 10.12 (2016), pp. 762–765.

[51] V. Jelic et al. "Ultrafast terahertz control of extreme tunnel currents through single atoms on a silicon surface". In: *Nature Physics* 13.6 (2017), pp. 591–598.

[52] G. Herink, L. Wimmer, and C. Ropers. "Field emission at terahertz frequencies: AC-tunneling and ultrafast carrier dynamics". In: *New Journal of Physics* 16 (2014).

[53] J. D. Zhang et al. "Terahertz radiation-induced sub-cycle field electron emission across a split-gap dipole antenna". In: *Applied Physics Letters* 107.23 (2015).

[54] S. Li and R. R. Jones. "High-energy electron emission from metallic nano-tips driven by intense single-cycle terahertz pulses". In: *Nature Communications* 7 (2016).

[55] M. Fakhari, A. Fallahi, and F. X. Kartner. "THz cavities and injectors for compact electron acceleration using laser-driven THz sources". In: *Physical Review Accelerators and Beams* 20.4 (2017).

[56] D. F. Zhang et al. "Segmented terahertz electron accelerator and manipulator (STEAM)". In: *Nature Photonics* 12.6 (2018), pp. 336–342.

[57] N. H. Matlis et al. "Acceleration of electrons in THz driven structures for AXSIS". In: *Nuclear Instruments and Methods in Physics Research Section A: Accelerators, Spectrometers, Detectors and Associated Equipment* (2018).

[58] A. Hirata et al. “120-GHz-band wireless link technologies for outdoor 10-Gbit/s data transmission”. In: *IEEE Transactions on Microwave Theory and Techniques* 60.3 (2012), pp. 881–895.

[59] KoenigS et al. “Wireless sub-THz communication system with high data rate”. In: *Nat Photon* 7.12 (2013), pp. 977–981.

[60] X. Y. Li, J. J. Yu, J. W. Zhang, Z. Dong, F. Li, and N. Chi. “A 400G optical wireless integration delivery system”. In: *Optics Express* 21.16 (2013), pp. 18812–18819.

[61] H. Shams, M. J. Fice, K. Balakier, C. C. Renaud, F. van Dijk, and A. J. Seeds. “Photonic generation for multichannel THz wireless communication”. In: *Optics Express* 22.19 (2014), pp. 23465–23472.

[62] Shi Jia et al. “THz photonic wireless links with 16-QAM modulation in the 375-450 GHz band”. In: *Optics Express* 24.21 (2016), pp. 23777–23783.

[63] I. Kallfass et al. “Towards MMIC-Based 300 GHz indoor wireless communication systems”. In: *Ieice Transactions on Electronics* E98c.12 (2015), pp. 1081–1090.

[64] A. Hirata et al. “120-GHz-band millimeter-wave photonic wireless link for 10-Gb/s data transmission”. In: *Ieee Transactions on Microwave Theory and Techniques* 54.5 (2006), pp. 1937–1944.

[65] I. Kallfass et al. “64 Gbit/s transmission over 850 m fixed wireless link at 240 GHz carrier frequency”. In: *Journal of Infrared Millimeter and Terahertz Waves* 36.2 (2015), pp. 221–233.

[66] Lin Chun-Yu et al. “A 400 Gbps/100 m free-space optical link”. In: *Laser Physics Letters* 14.2 (2017), p. 025206.

[67] T. Nagatsuma, G. Ducournau, and C. C. Renaud. “Advances in terahertz communications accelerated by photonics”. In: *Nature Photonics* 10 (2016), p. 371.

[68] M. Urteaga, Z. Griffith, M. Seo, J. Hacker, and M. J. W. Rodwell. “InP HBT technologies for THz integrated circuits”. In: *Proceedings of the IEEE* 105.6 (2017), pp. 1051–1067.

[69] M. M. Assefzadeh and A. Babakhani. “Broadband oscillator-free THz pulse generation and radiation based on direct digital-to-impulse architecture”. In: *IEEE Journal of Solid-State Circuits* 52.11 (2017), pp. 2905–2919.

[70] X. Wu and K. Sengupta. “Dynamic waveform shaping with picosecond time widths”. In: *IEEE Journal of Solid-State Circuits* 52.2 (2017), pp. 389–405.

[71] K. Sengupta and A. Hajimiri. "A 0.28 THz power-generation and beam-steering array in CMOS based on distributed active radiators". In: *IEEE Journal of Solid-State Circuits* 47.12 (2012), pp. 3013–3031.

[72] S. Pandey, G. Kumar, and A. Nahata. "Slot waveguide-based splitters for broadband terahertz radiation". In: *Optics Express* 18.22 (2010), pp. 23466–23471.

[73] K. S. Reichel, R. Mendis, and D. M. Mittleman. "A broadband terahertz waveguide T-junction variable power splitter". In: *Scientific Reports* 6 (2016), p. 28925.

[74] N. J. Karl, R. W. McKinney, Y. Monnai, R. Mendis, and D. M. Mittleman. "Frequency-division multiplexing in the terahertz range using a leaky-wave antenna". In: *Nature Photonics* 9 (2015), p. 717.

[75] J. Ma, N. J. Karl, S. Bretin, G. Ducournau, and D. M. Mittleman. "Frequency-division multiplexer and demultiplexer for terahertz wireless links". In: *Nature Communications* 8.1 (2017), p. 729.

[76] W. L. Chan, H.-T. Chen, A. J. Taylor, I. Brener, M. J. Cich, and D. M. Mittleman. "A spatial light modulator for terahertz beams". In: *Applied Physics Letters* 94.21 (2009), p. 213511.

[77] C. M. Watts et al. "Terahertz compressive imaging with metamaterial spatial light modulators". In: *Nature Photonics* 8 (2014), p. 605.

[78] K. J. Fang, Z. F. Yu, and S. H. Fan. "Realizing effective magnetic field for photons by controlling the phase of dynamic modulation". In: *Nature Photonics* 6.11 (2012), pp. 782–787.

[79] K. J. Fang, Z. F. Yu, and S. H. Fan. "Photonic Aharonov-Bohm effect based on dynamic modulation". In: *Physical Review Letters* 108.15 (2012).

[80] Q. F. Xu, P. Dong, and M. Lipson. "Breaking the delay-bandwidth limit in a photonic structure". In: *Nature Physics* 3.6 (2007), pp. 406–410.

[81] S. Sandhu, M. L. Povinelli, and S. H. Fan. "Stopping and time reversing a light pulse using dynamic loss tuning of coupled-resonator delay lines". In: *Optics Letters* 32.22 (2007), pp. 3333–3335.

[82] G. Günter et al. "Sub-cycle switch-on of ultrastrong light–matter interaction". In: *Nature* 458 (2009), p. 178.

[83] B. Mayer et al. "Sub-Cycle Slicing of High-Field Multi-THz Transients". In: *2014 39th International Conference on Infrared, Millimeter, and Terahertz Waves (IRMMW-THz)* (2014).

[84] T. Rybka, M. Ludwig, M. F. Schmalz, V. Knittel, D. Brida, and A. Leitenstorfer. "Sub-cycle optical phase control of nanotunnelling in the single-electron regime". In: *Nature Photonics* 10 (2016), p. 667.

[85] C. Riek et al. "Subcycle quantum electrodynamics". In: *Nature* 541 (2017), p. 376.

[86] N. Kamaraju et al. "Subcycle control of terahertz waveform polarization using all-optically induced transient metamaterials". In: *Light: Science &Amp; Applications* 3 (2014), e155.

[87] O. Schubert et al. "Sub-cycle control of terahertz high-harmonic generation by dynamical Bloch oscillations". In: *Nature Photonics* 8 (2014), p. 119.

[88] N. Yoshikawa, T. Tamaya, and K. Tanaka. "High-harmonic generation in graphene enhanced by elliptically polarized light excitation". In: *Science* 356.6339 (2017), p. 736.

[89] H. A. Hafez et al. "Extremely efficient terahertz high-harmonic generation in graphene by hot Dirac fermions". In: *Nature* 561.7724 (2018), pp. 507–511.

[90] J. Reimann et al. "Subcycle observation of lightwave-driven Dirac currents in a topological surface band". In: *Nature* (2018).

[91] F. J. Garcia-Vidal, L. Martin-Moreno, and J. B. Pendry. "Surfaces with holes in them: new plasmonic metamaterials". In: *Journal of Optics a-Pure and Applied Optics* 7.2 (2005), S97–S101.

[92] D. M. Wu et al. "Terahertz plasmonic high pass filter". In: *Applied Physics Letters* 83.1 (2003), pp. 201–203.

[93] H. Tao et al. "Highly flexible wide angle of incidence terahertz metamaterial absorber: Design, fabrication, and characterization". In: *Physical Review B* 78.24 (2008).

[94] O. Paul, R. Beigang, and M. Rahm. "Highly selective terahertz bandpass filters based on trapped mode excitation". In: *Optics Express* 17.21 (2009), pp. 18590–18595.

[95] Y. J. Chiang, C. S. Yang, Y. H. Yang, C. L. Pan, and T. J. Yen. "An ultrabroad terahertz bandpass filter based on multiple-resonance excitation of a composite metamaterial". In: *Applied Physics Letters* 99.19 (2011).

[96] X. Q. Zhang, J. Q. Gu, W. Cao, J. G. Han, A. Lakhtakia, and W. L. Zhang. "Bilayer-fish-scale ultrabroad terahertz bandpass filter". In: *Optics Letters* 37.5 (2012), pp. 906–908.

[97] N. R. Han, Z. C. Chen, C. S. Lim, B. Ng, and M. H. Hong. "Broadband multi-layer terahertz metamaterials fabrication and characterization on flexible substrates". In: *Optics Express* 19.8 (2011), pp. 6990–6998.

[98] H. T. Chen, W. J. Padilla, J. M. O. Zide, A. C. Gossard, A. J. Taylor, and R. D. Averitt. "Active terahertz metamaterial devices". In: *Nature* 444.7119 (2006), pp. 597–600.

[99] H. T. Chen et al. "Experimental demonstration of frequency-agile terahertz metamaterials". In: *Nature Photonics* 2.5 (2008), pp. 295–298.

[100] D. Shrekenhamer et al. "High speed terahertz modulation from metamaterials with embedded high electron mobility transistors". In: *Optics Express* 19.10 (2011), pp. 9968–9975.

[101] G. Wysocki, R. F. Curl, F. K. Tittel, R. Maulini, J. M. Bulliard, and J. Faist. "Widely tunable mode-hop free external cavity quantum cascade laser for high resolution spectroscopic applications". In: *Applied Physics B-Lasers and Optics* 81.6 (2005), pp. 769–777.

[102] R. Maulini, A. Mohan, M. Giovannini, J. Faist, and E. Gini. "External cavity quantum-cascade laser tunable from 8.2 to 10.4 μm using a gain element with a heterogeneous cascade". In: *Applied Physics Letters* 88.20 (2006).

[103] B. G. Lee et al. "Widely tunable single-mode quantum cascade laser source for mid-infrared spectroscopy". In: *Applied Physics Letters* 91.23 (2007).

[104] A. Hugi et al. "External cavity quantum cascade laser tunable from 7.6 to 11.4 mu m". In: *Applied Physics Letters* 95.6 (2009).

[105] L. Consolino et al. "Spectral purity and tunability of terahertz quantum cascade laser sources based on intracavity difference-frequency generation". In: *Science Advances* 3.9 (2017).

[106] M. Wienold et al. "High-temperature, continuous-wave operation of terahertz quantum-cascade lasers with metal-metal waveguides and third-order distributed feedback". In: *Optics Express* 22.3 (2014), pp. 3334–3348.

[107] Y. Sasaki, A. Yuri, K. Kawase, and H. Ito. "Terahertz-wave surface-emitted difference frequency generation in slant-stripe-type periodically poled LiNbO3 crystal". In: *Applied Physics Letters* 81.18 (2002), pp. 3323–3325.

[108] F. Ahr et al. "Narrowband terahertz generation with chirped-and-delayed laser pulses in periodically poled lithium niobate". In: *Optics Letters* 42.11 (2017), pp. 2118–2121.

[109] C. H. Zhang, Y. Avetisyan, A. Glosser, I. Kawayama, H. Murakami, and M. Tonouchi. "Bandwidth tunable THz wave generation in large-area periodically poled lithium niobate". In: *Optics Express* 20.8 (2012), pp. 8784–8790.

[110] Y. Avestisyan et al. "Terahertz generation by optical rectification in lithium niobate crystal using a shadow mask". In: *Optics Express* 20.23 (2012), pp. 25752–25757.

[111] C. H. Zhang, Y. Avetisyan, G. Abgaryan, I. Kawayama, H. Murakami, and M. Tonouchi. "Tunable narrowband terahertz generation in lithium niobate crystals using a binary phase mask". In: *Optics Letters* 38.6 (2013), pp. 953–955.

[112] S. Hayashi, K. Nawata, T. Taira, J. Shikata, K. Kawase, and H. Minamide. "Ultrabright continuously tunable terahertz-wave generation at room temperature". In: *Scientific Reports* 4 (2014).

[113] J. Faist, F. Capasso, D. L. Sivco, C. Sirtori, A. L. Hutchinson, and A. Y. Cho. "Quantum Cascade Laser". In: *Science* 264.5158 (1994), pp. 553–556.

[114] Y. Kawada, T. Yasuda, and H. Takahashi. "Carrier envelope phase shifter for broadband terahertz pulses". In: *Optics Letters* 41.5 (2016), pp. 986–989.

[115] Y. Kawada, T. Yasuda, A. Nakanishi, K. Akiyama, K. Hakamata, and H. Takahashi. "Achromatic prism-type wave plate for broadband terahertz pulses". In: *Optics Letters* 39.9 (2014), pp. 2794–2797.

[116] G. R. Keiser et al. "Nonlinear terahertz metamaterials with active electrical control". In: *Applied Physics Letters* 111.12 (2017).

[117] R. Shimano, H. Nishimura, and T. Sato. "Frequency tunable circular polarization control of terahertz radiation". In: *Japanese Journal of Applied Physics Part 2-Letters & Express Letters* 44.20-23 (2005), pp. L676–L678.

[118] Y. Hirota, R. Hattori, M. Tani, and M. Hangyo. "Polarization modulation of terahertz electromagnetic radiation by four-contact photoconductive antenna". In: *Optics Express* 14.10 (2006), pp. 4486–4493.

[119] R. Imai, N. Kanda, T. Higuchi, K. Konishi, and M. Kuwata-Gonokami. "Generation of broadband terahertz vortex beams". In: *Optics Letters* 39.13 (2014), pp. 3714–3717.

[120] S. Morimoto, T. Arikawa, F. Blanchard, K. Sakai, K. Sasaki, and K. Tanaka. "Control of Spoof Localized Surface Plasmons by Vortex of Light in Terahertz Region". In: *2016 41st International Conference on Infrared, Millimeter, and Terahertz Waves (IRMMW-THz)* (2016).

[121] T. Arikawa, S. Morimoto, and K. Tanaka. "Focusing light with orbital angular momentum by circular array antenna". In: *Optics Express* 25.12 (2017), pp. 13728–13735.

[122] Z. P. Jian, J. Pearce, and D. M. Mittleman. "Two-dimensional photonic crystal slabs in parallel-plate metal waveguides studied with terahertz time-domain spectroscopy". In: *Semiconductor Science and Technology* 20.7 (2005), S300–S306.

[123] P. Peier, H. Merbold, V. Pahinin, K. A. Nelson, and T. Feurer. "Imaging of THz waves in 2D photonic crystal structures embedded in a slab waveguide". In: *New Journal of Physics* 12 (2010).

[124] P. A. George, C. Manolatou, F. Rana, A. L. Bingham, and D. R. Grischkowsky. "Integrated waveguide-coupled terahertz microcavity resonators". In: *Applied Physics Letters* 91.19 (2007).

[125] R. Mendis and D. M. Mittleman. "Comparison of the lowest-order transverse-electric (TE1) and transverse-magnetic (TEM) modes of the parallel-plate waveguide for terahertz pulse applications". In: *Optics Express* 17.17 (2009), pp. 14839–14850.

[126] Eui Su Lee and Tae-In Jeon. "Tunable THz notch filter with a single groove inside parallel-plate waveguides". In: *Opt. Express* 20.28 (2012), pp. 29605–29612.

[127] S. S. Harsha, N. Laman, and D. Grischkowsky. "High-Q terahertz Bragg resonances within a metal parallel plate waveguide". In: *Applied Physics Letters* 94.9 (2009).

[128] M. Mbonye, R. Mendis, and D. M. Mittleman. "Inhibiting the TE1-mode diffraction losses in terahertz parallel-plate waveguides using concave plates". In: *Optics Express* 20.25 (2012), pp. 27800–27809.

[129] A. Alphones and M. Tsutsumi. "Leaky-wave radiation from a periodically photoexcited semiconductor slab wave-guide". In: *Ieee Transactions on Microwave Theory and Techniques* 43.9 (1995), pp. 2435–2441.

[130] A. Alphones and M. Tsutsumi. "Optically controlled Bragg reflection characteristic of millimeter waves in a corrugated dielectric waveguide". In: *Microwave and Optical Technology Letters* 17.6 (1998), pp. 352–357.

[131] A. Alphones. "Bragg reflection filter by periodic photoexcitation of a semiconductor waveguide". In: *Microwave and Optical Technology Letters* 23.2 (1999), pp. 117–120.

[132] L. Fekete, F. Kadlec, H. Nemec, and P. Kuzel. "Fast one-dimensional photonic crystal modulators for the terahertz range". In: *Optics Express* 15.14 (2007), pp. 8898–8912.

[133] A. L. Bingham and D. Grischkowsky. "High Q, one-dimensional terahertz photonic waveguides". In: *Applied Physics Letters* 90.9 (2007), p. 091105.

[134] A. L. Bingham and D. R. Grischkowsky. "Terahertz 2-D photonic crystal waveguides". In: *Ieee Microwave and Wireless Components Letters* 18.7 (2008), pp. 428–430.

[135] C. M. Yee and M. S. Sherwin. "High-Q terahertz microcavities in silicon photonic crystal slabs". In: *Applied Physics Letters* 94.15 (2009).

[136] E. S. Lee, S. G. Lee, C. S. Kee, and T. I. Jeon. "Terahertz notch and low-pass filters based on band gaps properties by using metal slits in tapered parallel-plate waveguides". In: *Optics Express* 19.16 (2011), pp. 14852–14859.

[137] E. S. Lee, J. K. So, G. S. Park, D. Kim, C. S. Kee, and T. I. Jeon. "Terahertz band gaps induced by metal grooves inside parallel-plate waveguides". In: *Opt Express* 20.6 (2012), pp. 6116–23.

[138] D. G. Cooke and P. U. Jepsen. "Time-resolved THz spectroscopy in a parallel plate waveguide". In: *Physica Status Solidi a-Applications and Materials Science* 206.5 (2009), pp. 997–1000.

[139] D. G. Cooke and P. U. Jepsen. "Dynamic optically induced planar terahertz quasioptics". In: *Applied Physics Letters* 94.24 (2009).

[140] D. G. Cooke and P. U. Jepsen. "Optical modulation of terahertz pulses in a parallel plate waveguide". In: *Opt. Express* 16 (2008), pp. 15123–9.

[141] D. G. Cooke and P. U. Jepsen. "Dynamic optically induced planar terahertz quasioptics". In: *Appl. Phys. Lett.* 94 (2009), p. 241118.

[142] J. Liu, J. K. Butler, G. A. Evans, and A. Rosen. "Analysis of millimeter wave phase shifters coupled to a fixed periodic structure". In: *Ieee Transactions on Microwave Theory and Techniques* 44.8 (1996), pp. 1416–1423.

[143] J. Ahn, A. V. Efimov, R. D. Averitt, and A. J. Taylor. "Terahertz waveform synthesis via optical rectification of shaped ultrafast laser pulses". In: *Opt. Express* 11 (2003), pp. 2486–2496.

[144] M. Sato et al. "Terahertz polarization pulse shaping with arbitrary field control". In: *Nat. Photonics* 7 (2013), pp. 724–731.

[145] P. U. Jepsen, D. G. Cooke, and M. Koch. "Terahertz spectroscopy and imaging - Modern techniques and applications". In: *Laser & Photonics Reviews* 5.1 (2011), pp. 124–166.

[146] M. Tonouchi. "Cutting-edge terahertz technology". In: *Nature Photonics* 1.2 (2007), pp. 97–105.

[147] S. S. Dhillon et al. "The 2017 terahertz science and technology roadmap". In: *Journal of Physics D-Applied Physics* 50.4 (2017).

[148] M. Rahm, J. S. Li, and W. J. Padilla. "THz wave modulators: a brief review on different odulation techniques". In: *Journal of Infrared Millimeter and Terahertz Waves* 34.1 (2013), pp. 1–27.

[149] P. R. Smith, D. H. Auston, and M. C. Nuss. "Subpicosecond photoconducting dipole antennas". In: *Ieee Journal of Quantum Electronics* 24.2 (1988), pp. 255–260.

[150] D. H. Auston and M. C. Nuss. "Electrooptic generation and detection of femtosecond electrical transients". In: *Ieee Journal of Quantum Electronics* 24.2 (1988), pp. 184–197.

[151] C. Fattinger and D. Grischkowsky. "Point-Source Terahertz Optics". In: *Applied Physics Letters* 53.16 (1988), pp. 1480–1482.

[152] F. Blanchard et al. "Generation of 1.5 μJ single-cycle terahertz pulses by optical rectification from a large aperture ZnTe crystal". In: *Optics Express* 15.20 (2007), pp. 13212–13220.

[153] F. Blanchard et al. "Effect of extreme pump pulse reshaping on intense terahertz emission in lithium niobate at multimilliJoule pump energies". In: *Optics Letters* 39.15 (2014), pp. 4333–4336.

[154] K. H. Yang, P. L. Richards, and Y. R. Shen. "Generation of far-infrared radiation by picosecond light pulses in $LiNbO_3$". In: *Applied Physics Letters* 19.9 (1971), pp. 320–323.

[155] A. Rice et al. "Terahertz optical rectification from (110) zincblende crystals". In: *Applied Physics Letters* 64.11 (1994), pp. 1324–1326.

[156] R. A. Kaindl, F. Eickemeyer, M. Woerner, and T. Elsaesser. "Broadband phase-matched difference frequency mixing of femtosecond pulses in GaSe: Experiment and theory". In: *Applied Physics Letters* 75.8 (1999), pp. 1060–1062.

[157] A. Nahata, A. S. Weling, and T. F. Heinz. "A wideband coherent terahertz spectroscopy system using optical rectification and electro-optic sampling". In: *Applied Physics Letters* 69.16 (1996), pp. 2321–2323.

[158] J. Hebling, K.-L. Yeh, M. C. Hoffmann, B. Bartal, and K. A. Nelson. "Generation of high-power terahertz pulses by tilted-pulse-front excitation and their application possibilities". In: *Journal of the Optical Society of America B* 25.7 (2008), B6–B19.

[159] A. G. Stepanov, J. Hebling, and J. Kuhl. "Efficient generation of subpicosecond terahertz radiation by phase-matched optical rectification using ultrashort laser pulses with tilted pulse fronts". In: *Applied Physics Letters* 83.15 (2003), pp. 3000–3002.

[160] J. Hebling, A. G. Stepanov, G. Almaasi, B. Bartal, and J. Kuhl. "Tunable THz pulse generation by optical rectification of ultrashort laser pulses with tilted pulse fronts". In: *Applied Physics B-Lasers and Optics* 78.5 (2004), pp. 593–599.

[161] Q. Wu and X. -C Zhang. "Ultrafast electro-optic field sensors". In: *Applied Physics Letters* 68.12 (1996), pp. 1604–1606.

[162] H. Hirori, A. Doi, F. Blanchard, and K. Tanaka. "Single-cycle terahertz pulses with amplitudes exceeding 1 MV/cm generated by optical rectification in $LiNbO_3$". In: *Applied Physics Letters* 98.9 (2011).

[163] S. B. Bodrov, A. A. Murzanev, Y. A. Sergeev, Y. A. Malkov, and A. N. Stepanov. "Terahertz generation by tilted-front laser pulses in weakly and strongly nonlinear regimes". In: *Applied Physics Letters* 103.25 (2013).

[164] S. Vidal, J. Degert, M. Tondusson, E. Freysz, and J. Oberle. "Optimized terahertz generation via optical rectification in ZnTe crystals". In: *Journal of the Optical Society of America B-Optical Physics* 31.1 (2014), pp. 149–153.

[165] N. Masaru, H. Shinji, T. Shunji, T. Kazuya, F. Yasunori, and K. Kenji. "Optical damage resistance and refractive indices in near-stoichiometric MgO-doped $LiNbO_3$". In: *Japanese Journal of Applied Physics* 41.1A (2002), p. L49.

[166] L. Pálfalvi, J. Hebling, J. Kuhl, Á Péter, and K. Polgár. "Temperature dependence of the absorption and refraction of Mg-doped congruent and stoichiometric $LiNbO_3$ in the THz range". In: *Journal of Applied Physics* 97.12 (2005), p. 123505.

[167] C. A. Werley, Q. A. Wu, K. H. Lin, C. R. Tait, A. Dorn, and K. A. Nelson. "Comparison of phase-sensitive imaging techniques for studying terahertz waves in structured $LiNbO_3$". In: *Journal of the Optical Society of America B-Optical Physics* 27.11 (2010), pp. 2350–2359.

[168] Z. Y. Wang, F. H. Su, and F. A. Hegmann. "Ultrafast imaging of terahertz Cherenkov waves and transition-like radiation in $LiNbO_3$". In: *Optics Express* 23.6 (2015), pp. 8073–8086.

[169] P. U. Jepsen, M. Schall, V. Schyja, C. Winnewisser, H. Helm, and S. R. Keiding. "Detection of high power THz pulses by phase retardation in an electro-optic crystal". In: *Ultrafast Processes in Spectroscopy* (1996), pp. 645–648.

[170] Q. Wu, T. D. Hewitt, and X. C. Zhang. "Two-dimensional electro-optic imaging of THz beams". In: *Applied Physics Letters* 69.8 (1996), pp. 1026–1028.

[171] A. Nahata, D. H. Auston, T. F. Heinz, and C. J. Wu. "Coherent detection of freely propagating terahertz radiation by electro-optic sampling". In: *Applied Physics Letters* 68.2 (1996), pp. 150–152.

[172] A. Leitenstorfer, S. Hunsche, J. Shah, M. C. Nuss, and W. H. Knox. "Detectors and sources for ultrabroadband electro-optic sampling: Experiment and theory". In: *Applied Physics Letters* 74.11 (1999), pp. 1516–1518.

[173] Q. Wu and X. C. Zhang. "7 terahertz broadband GaP electro-optic sensor". In: *Applied Physics Letters* 70.14 (1997), pp. 1784–1786.

[174] P. C. M. Planken, H. K. Nienhuys, H. J. Bakker, and T. Wenckebach. "Measurement and calculation of the orientation dependence of terahertz pulse detection in ZnTe". In: *Journal of the Optical Society of America B-Optical Physics* 18.3 (2001), pp. 313–317.

[175] T. I. Jeon and D. Grischkowsky. "Nature of conduction in doped silicon". In: *Physical Review Letters* 78.6 (1997), pp. 1106–1109.

[176] L. Gingras, M. Georgin, and D. G. Cooke. "Dynamic light-induced THz resonators in a waveguide". In: *2015 Conference on Lasers and Electro-Optics (CLEO)* (2015).

[177] Laxmi Shiveshwari and Parmanand Mahto. "Photonic band gap effect in one-dimensional plasma dielectric photonic crystals". In: *Solid State Communications* 138.3 (2006), pp. 160–164.

[178] J. M. Bendickson, J. P. Dowling, and M. Scalora. "Analytic expressions for the electromagnetic mode density in finite, one-dimensional, photonic band-gap structures". In: *Physical Review E* 53.4 (1996), pp. 4107–4121.

[179] S. H. Kim, E. S. Lee, Y. Bin Ji, and T. I. Jeon. "Improvement of THz coupling using a tapered parallel-plate waveguide". In: *Optics Express* 18.2 (2010), pp. 1289–1295.

[180] R. Mendis. "Nature of subpicosecond terahertz pulse propagation in practical dielectric-filled parallel-plate waveguides". In: *Optics Letters* 31.17 (2006), pp. 2643–2645.

[181] M. Walther, D. G. Cooke, C. Sherstan, M. Hajar, M. R. Freeman, and F. A. Hegmann. "Terahertz conductivity of thin gold films at the metal-insulator percolation transition". In: *Physical Review B* 76.12 (2007).

[182] T. Kampfrath, D. M. Beggs, T. P. White, A. Melloni, T. F. Krauss, and L. Kuipers. "Ultrafast adiabatic manipulation of slow light in a photonic crystal". In: *Physical Review A* 81.4 (2010).

[183] C. H. Yang, G. Sarma, D. H. Parker, J. J. ter Meulen, and L. Wiesenfeld. "State-to-state differential and relative integral cross sections for rotationally inelastic scattering of H_2O by hydrogen". In: *The Journal of Chemical Physics* 134.20 (2011), p. 204308.

Bibliography - Theses

[184] David G. Cooke. “Time-resolved terahertz spectroscopy of bulk and nanoscale semiconductors”. Thesis. 2007.

Bibliography - Books

[185] Y.-S. Lee. *Principles of Terahertz Science and Technology*. Springer, 2009. ISBN: 978-0-387-09539-4.

[186] G. Gruner M. Dressel. *Electrodynamics of Solids: Optical Properties of Electrons in Matter*. Cambridge University Press, 2002. ISBN: 0 521 59726 9.

[187] D. Mittleman. *Sensing with Terahertz Radiation*. 2003. ISBN: 978-3-642-07717-3. DOI: 10.1007/978-3-540-45601-8.

[188] S. L. Dexheimer. *Terahertz Spectroscopy: Principles and Applications*. CRC Press, 2008. ISBN: 978-0-8493-7525-5.

[189] Y. R. Shen. *Nonlinear Optics*. 2012. ISBN: 0471430803.

[190] Robert P. Boyd. *Nonlinear Optics*. Third. Elsevier Inc., 2008. ISBN: 978-0-12-369470-6.

[191] W. J. Tropf and M. E. Thomas. *Handbook of Optical Constants of Solids*. Vol. 2. Elsevier Inc., 1997, p. 1096. ISBN: 978-0-12-544415-6.

[192] R. A. Serway. *Principles of Physics*. Saunders Golden Sunburst Ser. Saunders College Publishing, 1997. ISBN: 0030204577.

[193] John Joannopoulos, Steven Johnson, Joshua Winn, and Robert Meade. *Photonic Crystals: Molding the Flow of Light. second edition*. 2008. DOI: citeulike-article-id:8898374.